# Seismic Anisotropy of the Deep Earth from a Mineral and Rock Physics Perspective

**D. Mainprice**
Université Montpellier II, Montpellier, France

## 1 Introduction

Seismic anisotropy is commonly defined as the direction-dependent nature of the propagation velocities of seismic waves. However, this definition does not cover all the seismic manifestations of seismic anisotropy. In addition to direction-dependent velocity, there is direction-dependent polarization of P- and S-waves, and anisotropy can contribute to the splitting of normal modes. Seismic anisotropy is a characteristic feature of the Earth, with anisotropy being present near the surface due to aligned cracks (e.g., Crampin, 1984), in the lower crust, upper and lower mantle due to mineral-preferred orientation (e.g., Karato, 1998; Mainprice *et al.*, 2000). At the bottom of the lower mantle (D″layer, e.g., Kendall and Silver (1998)) and in the solid inner core (e.g., Ishii *et al.*, 2002a) the causes of anisotropy are still controversial (**Figure 1**). In some cases multiple physical factors could be contributing to the measured anisotropy, for example, mineral-preferred orientation and alignment of melt inclusions at mid-ocean ridge systems (e.g., Mainprice, 1997). In the upper mantle, the pioneering work of Hess (1964) and Raitt *et al.* (1969) from Pn velocity measurements in the shallow mantle of the ocean basins showed azimuthal anisotropy. Long-period surface waves studies (e.g., Nataf *et al.*, 1984; Montagner and Tanimoto, 1990) have since confirmed that azimuthal and SH/SV polarization anisotropy are global phenomena in the Earth's upper mantle, particularly in the top 200 km of the upper mantle. Anisotropic global tomography, based on surface and body wave data, has shown that anisotropy is very strong in the subcontinental mantle and present generally in the upper mantle, but significantly weaker at greater depths (e.g., Beghein *et al.*, 2006; Panning and Romanowicz, 2006). The long wavelengths used in long-period surface wave studies means that such methods are insensitive to heterogeneity less than the wavelength of about 1000 km. In an effort to address the problem of regional variations of anisotropy, the splitting of SKS teleseismic shear waves that propagate vertically have been extensively used. At continental stations SKS studies show that the azimuth of the fast polarization direction is parallel to the trend of mountain belts (Kind *et al.*, 1985; Silver and Chan 1988,

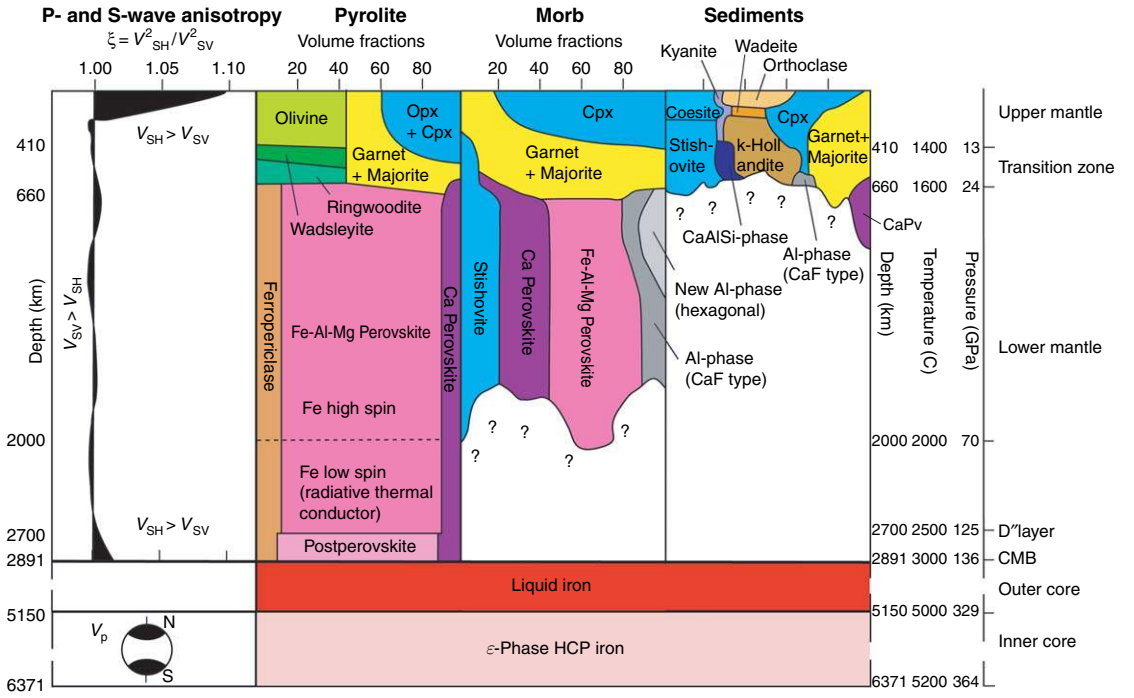


**Figure 1** The simplified petrology and seismic anisotropy of the Earth's mantle and core. The radially (transverse isotropic) anisotropic model of S-wave anisotropy of the mantle is taken from Panning and Romanowicz (2006). The icon at the inner core represents the fast P-wave velocities parallel to the rotation axis of the Earth. The petrology of mantle is taken from Ono and Oganov (2005) for pyrolite, Perrillat *et al*. (2006) for the transformed MORB and based on Irifune *et al*. (1994) as modified by Poli and Schmidt (2002) for the transformed argillaceous sediments.

1991; Vinnik *et al*., 1989; Silver, 1996; Fouch and Rondenay, 2006). From the earliest observations it was clear that the anisotropy in the upper mantle was caused by the preferred orientation of olivine crystals induced by plastic deformation related to mantle flow processes at the geodynamic or plate tectonic scale.

The major cause of seismic anisotropy in the upper mantle is the crystal-preferred orientation (CPO) caused by plastic deformation. Knowledge of the CPO and its evolution requires well-characterized naturally deformed samples, experimentally deformed samples and numerical simulation for more complex deformation histories of geodynamic interest. The CPO not only causes seismic anisotropy, but also records some aspects of the deformation history. Samples of the Earth's mantle are readily found on the surface in the form of ultramafic massifs, xenoliths in basaltic or kimberlitic volcanics and as inclusions in diamonds. However, samples from depths greater than 220 km are extremely rare. Upper-mantle samples large enough for the measurement of CPO have been recovered from kimberlitic volcanics in South Africa to a depth of about 220 km established by geobarometry (e.g., Boyd, 1973). Kimberlite mantle xenoliths of deeper origin (>300 km) with evidence for equilibrated majorite garnet which is now preserved as pyrope garnet with exsolved pyroxene have been reported (Haggerty and Sautter, 1990; Sautter *et al*., 1991). The Alpe Arami peridotite garnet lherzolite is proposed to have been exhumed from a minimum depth of 250 km based on clinoenstatite exsolution lamellae present in diopside grains (Bozhilov *et al*., 1999). Samples of even deeper origin are preserved as inclusions in diamonds. Although most diamonds crystallize at depths of 150–200 km, some diamonds contain inclusions of majorite (Moore and Gurney, 1985), enstatite and ferripericlase (Scott-Smith *et al*., 1984), and $CaSiO_3 + (Fe, Mg)SiO_3 + SiO_2$ (Harte and Harris, 1993). The mineral associations imply transition zone (410–660 km) and lower-mantle origins for these diamond inclusions (Kesson and Fitz, 1991). Although these samples help to constrain mantle petrology, they are too small to provide information about CPO. Hence, knowledge of CPO in the transition zone, lower mantle, and inner core will be derived from deformation experiments at high pressure and temperatue (e.g., olivine – Couvy

*et al.*, 2004; ringwoodite – Karato *et al.*, 1998; perovskite – Cordier *et al.*, 2004b; $MgGeO_3$ postperovskite – Merkel *et al.*, 2006a; $\varepsilon$-phase iron – Merkel *et al.*, 2005).

It has been accepted since the PREM seismic model (Dziewoński and Anderson, 1981) that the top 200 km of the Earth's mantle is anisotropic on a global scale (**Figure 1**). However, there are exceptions, for example, under the Baltic shield the anisotropy increases below 200 km (Pedersen *et al.*, 2006). The seismic discontinuity at about 200 km was first reported by the Danish seismologist Inge Lehmann (1959, 1961), that now bears her name. However, the discontinuity is not always present at the same depth. Anderson (1979) interpreted the discontinuity as the petrological change of garnet lherzolite to eclogite. More recently, interpretations have favored an anisotropy discontinuity, although even this is controversial (see Vinnik *et al.* (2005)), proposed interpretations include: a local anisotropic decoupling shear zone marking the base of the lithosphere (Leven *et al.*, 1981), a transition from an anisotropic mantle deforming by dislocation creep to isotropic mantle undergoing diffusion creep (Karato, 1992), simply the base of an anisotropic layer beneath continents (e.g., Gaherty and Jordan, 1995), or the transition from [100] to [001] direction slip in olivine (Mainprice *et al.*, 2005). Global tomography studies show that the base of the anisotropic subcontinental mantle may vary in depth from 100 to 450 km (e.g., Polet and Anderson, 1995), but most global studies favor an anisotropy discontinuity for S-waves at around 200–250 km, which is stronger and deeper (300 km) beneath continents (e.g., Deuss and Woodhouse, 2002; Ritsema *et al.*, 2004; Panning and Romanowicz, 2006) and weaker and shallower (200 km) beneath the oceans. There is also evidence for weak seismic discontinuities at 260 and 310 km which has been reported in subduction zones by Deuss and Woodhouse (2002).

A major seismic discontinuity at 410 km is due to the transformation of olivine to wadsleyite (e.g., Helffrich and Wood, 1996) with a shear wave impedance contrast of 6.7% (e.g., Shearer, 1996). The 410 km discontinuity has topography within 5 km of the global average. The olivine to wadsleyite transformation will result in the lowering of anisotropy with depth. Global tomography models (e.g., Montagner, 1994a, 1994b; Montagner and Kennett, 1996; Beghein *et al.*, 2006; Panning and Romanowicz, 2006) indicate that the strength of anisotropy is less in the transition zone (410–660 km) than in the upper mantle (**Figure 1**). A global study of the anisotropy of transion zone by Trampert and van Heijst (2002) has detected a weak anisotropy shear wave of about 1–2%. The surface wave overtone technique used by Trampert and van Heijst (2002) cannot localize the anisotropy within the 410–660 km depth range; however the only mineral with a strong anisotropy and significant volume fraction in the transition zone is wadsleyite occurring between 410 and 520 km. Between 520 and 660 km there is an increase the very weakly anisotropic phases, such as garnet, majorite, and ringwoodite in the transition zone (**Figure 1**). Tommasi *et al.* (2004) have shown that the CPO predicted by a plastic flow model using the experimentally observed slip systems of wadsleyite can reproduce the weak anisotropy observed by Trampert and van Heijst (2002). A weaker discontinuity at 520 km, with a shear wave impedance contrast of 2.9%, has been reported by Shearer and co-workers (e.g., Shearer, 1996; Flanagan and Shearer, 1998). The discontinuity at 520 km depth has been attributed to the wadsleyite to ringwoodite transformation by Shearer (1996). Deuss and Woodhouse (2001) have reported the 'splitting' of the 520 km discontinuity into two discontinuities at 500 and 560 km, they interpret the variations of depth of 520 km, and presence of two discontinuities at 500 and 560 km in certain regions can only be explained by variations in temperature and composition (e.g $Mg/Mg + Fe$ ratio), which effect the phase transition Clapeyron. Regional seismic studies by Vinnik and Montagner (1996) and Vinnik *et al.* (1997) show evidence for a weakly anisotropic (1.5%) layer for S-waves at the bottom 40 km of the transition zone (620–660 km). The some global tomography models (e.g., Montagner and Kennett, 1996; Montagner, 1998) also show significant transverse isotropic anisotropy in the transition zone with $V_{SH} > V_{SV}$ and $V_{PH} > V_{PV}$. Given the low intrinsic anisotropy of most of the minerals in the lower part of the transition zone, Karato (1998) suggested that this anisotropy is due to petrological layering caused by garnet and ringwoodite rich layers of transformed subducted oceanic crustal material. Such transversely isotropic medium with a vertical symmetry axis would not cause any splitting for vertically propagating S-waves and would not produce the azimuthal anisotropy observed by Trampert and van Heijst (2002), but

would produce the difference between horizontal and vertical velocities seen by global tomography. A global study supports this suggestion, as high-velocity slabs of former oceanic lithosphere are conspicuous structures just above the 660 km discontinuity in the circum-Pacific subuction zones (Ritsema *et al.*, 2004). A regional study by Wookey *et al.* (2002) also finds significant shear wave splitting associated with horizontally travelling S-waves, which is compatiable with a layered structure in the vicinity of the 660 km discontinuity. However, recent anisotropic global tomography models do not show significant anisotropy in this depth range (Beghein *et al.*, 2006; Panning and Romanowicz, 2006).

The strongest seismic discontinuity at 660 km is due to the dissociation of ringwoodite to perovskite and ferropericlase (**Figure 1**) with a shear wave impedance contrast of 9.9% (e.g., Shearer, 1996). The 660 km discontinuity has an important topography with local depressions of up to 60 km from the global average in subduction zones (e.g., Flanagan and Shearer, 1998). From 660 to 1000 km a weak anisotropy is observed in the top of the lower mantle with $V_{SH} < V_{SV}$ and $V_{PH} < V_{PV}$ (e.g., Montagner and Kennett, 1996; Montagner, 1998). Karato (1998) attributed the anisotropy to the CPO of perovskite and possibly ferropericlase caused by plastic deformation in the convective boundary layer at the top of the lower mantle. In this depth range, Kawakatsu and Niu (1994) have identified a flat seismic discontinuity at 920 km with S to P converted waves with an S-wave velocity change of 2.4% in Tonga, Japan Sea, and Flores Sea subuction zones. They suggested that this feature is thermodynamically controlled by some sort of phase transformation or alternatively we may suggest it marks the bottom of the anisotropic boundary layer proposed by Montagner (1998) and Karato (1998). Reflectors in lower mantle have been reported by Deuss and Woodhouse (2001) at 800 km depth under North America and at 1050 and 1150 km beneath Indonesia; they only considered the 800 km reflector to be a robust result. Karki *et al.* (1997b) have suggested that the transformation of the highly anisotropic $SiO_2$ polymorphs stishovite to $CaCl_2$ structure at $50 \pm 3$ GPa at room temperature may be the possible explanation of reflectivity in the top of the lower mantle. However, according to Kingma *et al.* (1995) the transformation would take place at 60 GPa at lower mantle temperatures in the range 2000–2500 K, corresponding to depth of 1200–1500 km, that is, several hundred kilometers below the 920 km discontinuity. It is highly speculative to suggest that free silica is responsible for the 920 km discontinuity as a global feature as proposed by Kawakatsu and Niu (1994). Ringwood (1991) suggested that 10% stishovite would be present from 350 to 660 km in subducted oceanic crust and this would increase to about 16% at 730 km. Hence, in the subduction zones studied by Kawakatsu and Niu (1994), it is quite possible that significant stishovite could be present to 1200 km and may be a contributing factor to the seismic anisotropy of the top of the lower mantle. From 1000 to 2700 km the lower mantle is isotropic for body waves or free oscillations (e.g., Montagner and Kennett, 1996; Beghein *et al.*, 2006; Panning and Romanowicz, 2006). Karato *et al.* (1995) have suggested by comparison with deformation experiments of fine-grained analogue oxide perovskite that the seismically isotropic lower mantle is undergoing deformation by superplasticity or diffusive creep which does not produce a crystal-preferred orientation. In the bottom of the lower mantle the D″ layer (100–300 km thick) appears to be transversely isotropic with a vertical symmetry axis characterized by $V_{SH} > V_{SV}$ (**Figure 1**) (e.g., Kendall and Silver, 1996, 1998), which may be caused by CPO of the constituent minerals, shape-preferred orientation of horizontally aligned inclusions, possibly melt (e.g., Williams and Garnero, 1996; Berryman, 2000) or core material. It has been suggested that the melt fraction of D″ may be as high as 30% (Lay *et al.*, 2004). Seismology has shown that D″ is extremely heterogeneous as shown by globally high fluctuations of shear (2–3%) and compressional (1%) wave velocities (e.g., Mégnin and Romanowcz, 2000; Ritsema and van Heijst, 2001; Lay *et al.*, 2004), a variation of the thickness of D″ layer between 60 and 300 km (e.g., Sidorin *et al.*, 1999a), P- and S-wave velocities variations are some times correlated and sometimes anticorrelated (thermal, chemical, and melting effects?) (e.g., Lay *et al.*, 2004), ultralow velocity zones (ULVZs) at the base of D″ with $V_p$ 10% slower and $V_s$ 30% slower than surrounding material (e.g., Garnero *et al.*, 1998), regions with horizonal (e.g., Kendall and Silver, 1998; Kendall, 2000) or inclined anisotropy (e.g., McNamara *et al.*, 2003; Garnero *et al.*, 2004; Maupin *et al.*, 2005; Wookey *et al.*, 2005a) in the range 0.5–1.5% and isotropic regions, localized patches of shear velocity discontinuity, even predicted the possibility of a globally extensive phase transformation (Nataf and Houard, 1993) and its Claperon slope (Sidorin *et al.*, 1999b). Until recently, the candidate phase for this transition was $SiO_2$. However, the mineralogical picture of the

D″ layer has been completely changed with the discovery of postperovskite by Murakami *et al.* (2004), which is produced by the transformation of Mg-perovskite in the laboratory at pressures greater than 125 GPa at high temperature. Seismic modeling of the D″ layer using the new phase diagram and elastic properties of perovskite and postperovskite can explain many features mentioned above near the core–mantle boundary (Wookey *et al.*, 2005b).

The inner solid core was the last elastic shell of the Earth to be identified by the Danish seismologist Inge Lehmann in a paper published in 1936 with the short title P′. She identified P-waves that traveled through the core region (PKP, where K stands for core) at epicentral distances of 105–142° in contradiction to the expected travel times for a single core model. She proposed a two-shell model for the core with a uniform velocity of about 10 km $s^{-1}$ with a small velocity discontinuity between each shell and a inner shell radius of 1400 km, close to the actually accepted value of 1221.5 km from PREM (Dziewoński and Anderson, 1981). The liquid nature of the outer core was first proposed by Jeffreys (1926) based on shear wave arrival times and the solid nature of inner core was first proposed by Birch (1940) based on the compressibility of iron at high pressure. Given the great depth (5149.5 km) and the number of layers a seismic wave has to traverse to reach the inner core and return to the surface it is not surprising the first report of anisotropy of the inner core was inferred fifty years after the discovery of the inner core. Poupinet *et al.* (1983) were the first to observe that PKIKP (where K now stands for the outer core and I is for inner core) P-waves travel about 2 s faster parallel to the Earth's rotation axis than waves traveling the equatorial plane. They interpreted their observations in terms of a possible heterogeneity of the inner core. Shortly afterwards, a PKIKP travel time study by Morelli *et al.* (1986) and normal modes (free oscillations) by Woodhouse *et al.* (1986) reported new observations and interpreted the results in terms of anisotropy. However, the interpretation of PKIKP body wave travel times in terms of anisotropy remained controversial, with an alternative interpretation being that the inner core had a nonspherical structure (e.g., Widmer *et al.*, 1992). Finally, the observation of large differential travel times for PKIKP for paths from the South Sandwich Islands to Alaska by Creager (1992), Song and Helmberger (1993), and the interpretation of higher-quality free oscillation data by Tromp (1993, 1994) and Durek and Romanowicz (1999) gave further strong support for the homogenous transverse anisotropy interpretation. The general consensus became that the inner core is strongly anisotropic, with a P-wave anisotropy of about 3–4% with the fast velocity direction parallel to the Earth's rotation axis (see reviews by Creager (2000), Song (1997), and Tromp (2001). However, many studies have suggested variations to this simple anisotropy model of the inner core. It has been suggested that the symmetry axis of the anisotropy is tilted from the Earth's rotation axis (Shearer and Toy, 1991; Creager, 1992; Su and Dziewoński, 1995) by 5–10°. A significant difference in the anisotropy between Eastern and Western Hemispheres of the inner core has been reported by Tanaka and Hamaguchi (1997) and Creager (1999) with the Western Hemisphere having significantly stronger anisotropy than the Eastern Hemisphere that is nearly isotropic. Several recent studies concur that the outer part (100–200 km) of the inner core is isotropic and inner part is anisotropic (e.g., Song and Helmberger, 1998; Garcia and Souriau, 2000, 2001; Song and Xu, 2002; Garcia, 2002). It has also been suggested that there is a small innermost inner core with radius of about 300 km with distinct transverse isotropy relative to the outermost inner core by Ishii and Dziewoński (2002) **Figure 2**(**a**). The innermost core has the slowest P-wave velocity at 45° to the east–west direction and the outer part has a weaker anisotropy with slowest P-wave velocity parallel to the east–west direction. Using split normal mode constraints, Beghein and Trampert (2003) also showed that there is a change in velocity structure with radius in the inner core; however, their model (**Figure 2**(**b**)) shows that the symmetry of the P- and S-wave changes at about 400 km radius, suggesting a radical change, such as a phase transition of iron. Much of the complexity of the observations seems to be station and method dependent (see Ishii *et al.* (2002a, 2002b). In a detailed study Ishii *et al.* (2002a, 2002b) derive a model that simultaneously satisfies normal mode, absolute travel time, and differential travel time data. It has allowed them to separate a mantle signature and regional structure from global anisotropy of the inner core. Their preferred model of homogeneous transverse isotropy with a symmetry axis aligned with the rotation axis contradicts many of models proposed above, but is similar to

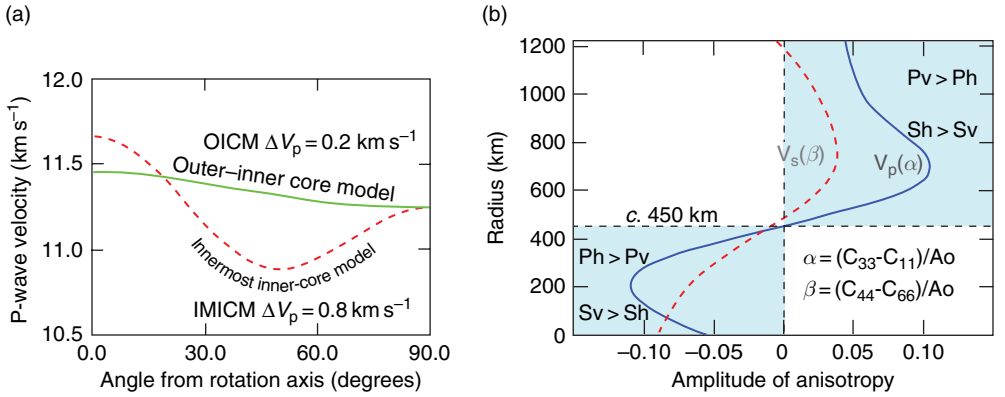


**Figure 2** (a) The outer–inner core and innermost inner-core P-wave anisotropy models of Ishii and Dziewoński (2002). Note that variation of $V_p$ is only 0.2 km s$^{-1}$ for outer–inner core model (300–1221 km radius) and 0.8 km s$^{-1}$ for innermost inner core model (0–300 km radius). (b) P- and S-wave inner-core models of Beghein and Trampert (2003). Note the veriation of $V_p$ in the outermost and innermost core is between about 5 and 10 km s$^{-1}$, but the symmetry is different. The amplitude of S-wave anisotropy is weaker than P-wave, but there is symmetry change for both at *c.* 450 km radius.

previous suggestions. In a study of inner-core P-wave anisotropy using both finite-frequency and ray theories, Calvet *et al.* (2006) found that the data can be explained by three families of models which all exhibit anisotropy changes at a radius between 550 and 400 km (compared to 300 km for Ishii and Dziewoński (2002, 2003) and about 400 km for Beghein and Trampert (2003)). The first model has a weak anisotropy with a slow P-wave velocity symmetry axis parallel to Earth's rotation axis. The second model has a nearly isotropic innermost inner core. Lastly, the third model has a strongly anisotropic innermost inner core with a fast symmetry axis parallel to Earth's rotation axis. These models have very different implications for the origin of the anisotropy and the history of Earth's core. These divergences partly reflect the uneven sampling of the inner core by PKP(DF) paths resulting from the spatial distribution of earthquakes and seismographic stations. More data are required to improve the determination of the anisotropic structure of the innermost inner core, as for example, nearly antipodal waves that may provide crucial constraints on the structures at the centre of the Earth.

Theoretical studies of the process of generating the Earth's magnetic field through fluid motion of the outer core have predicted that the electromagnetic torque would force the inner core to rotate relative to the mantle (Steenbeck and Helmis, 1975; Gubbins, 1981; Szeto and Smylie, 1984; Glatzmaier and Roberts, 1995, 1996). Song and Richards (1996) first reported seismic differential travel time observations based of three decades of data supporting the eastward relative rotation of inner core by about 1° per year faster than the daily rotation of the mantle and crust. Around the equator of the inner core, this rotation rate corresponds to a speed of a few tens of kilometers per year. The interpretation of the observed travel times required using the seismic anisotropy model inner core established by Su and Dziewoński (1995). Clearly to establish such small relative rotation rate a detailed knowledge of anisotropy, heterogeneity, and shape of the inner core is required, as travel times will change with direction and time (Song, 2000). The result was supported by some studies (e.g., Creager, 1997) and challenged by other studies (e.g., Souriau *et al.*, 1997), but all indicated a smaller rotation rate than 1° per year. The most recent study to date by Zhang *et al.* (2005) confirms a rotation rate of 0.3–0.5° using techniques that avoids artifacts of poor event locations and contamination by small-scale heterogeneities. Shear waves are very useful for determining the magnitude and orientation of anisotropy along individual ray paths. Despite several claims to have observed shear waves (e.g., Julian *et al.*, 1972; Okal and Cansi 1998), the analysis of the attenuation (Doornbos, 1974) and frequency range (Deuss *et al.*, 2000) reveals that these claims are unjustified. The analysis and validation of observations by Deuss *et al.* (2000) provide the first reliable observation of long period (20–30 s) shear waves providing new possibilities for exploring the anisotropy of inner core.

The transverse isotropy observed for P-waves traveling through the inner core could be explained by the CPO of hexagonal close packed (h.c.p.) from of iron ($\varepsilon$-phase) crystals or a layered structure. Analysis of the coda of short period inner core boundary reflected P-waves (PKiKP) require only a few percent heterogeneity at length scales of 2 km (Vidale and Earle, 2000) which suggests a relatively homogenous nonstructured inner core; however, this interpretation of coda has recently been questioned by Poupinet and Kennett (2004). The mechanism responsible for the CPO has been the subject of considerable speculation in recent years. The suggested mechanisms include: alignment of crystals in the magnetic field as they solidify from the liquid outer core (Karato, 1993), the alignment of crystals by plastic flow under the action of Maxwell normal stresses caused the magnetic field (Karato, 1999), faster crystal growth in the equatorial region of the inner core (Yoshida *et al.*, 1996), anisotropic growth driven by strain energy, dendric crystal growth aligned with the direction of dominant heat flow (Bergman, 1997), plastic flow in a thermally convective regime ( Jeanloz and Wenk, 1988; Wenk *et al.*, 1988; Wenk *et al.*, 2000), and plastic flow under the action of magnetically induced Maxwell shear stresses (Buffett and Wenk, 2001). An alternative explication was proposed by Singh *et al.* (2000) to explain the P-wave anisotropy and the low shear wave velocity of about 3.6 km s$^{-1}$ (Deuss *et al.* 2000) is the presence of a volume fraction of 3–10% liquid iron (or FeS) in the form of oblate spherical inclusions aligned in the equatorial plane in a matrix of iron crystals with their *c*-axes aligned parallel to the rotation axis as originally proposed by Stixrude and Cohen (1995). The S-wave velocity and attenuation data are mainly from the outer part of the inner core and hence it was suggested that the liquid inclusions are present in this region. Note this is in contradiction with other studies, which suggest that the outer core has a low anisotropy. Several problems posed by all models to different degrees include: whether the inner core is thermally convective (see Weber and Machetel, 1992; Yukutake, 1998); the viscosity of the inner core; the strength of magnetic field and magnitude of the Maxwell stresses necessary to cause crystal alignment; and the presence of liquids or even the ability of the models to correctly predict the magnitude and orientation of the seismic P-wave anisotropy. Given the range of seismic models and the variety of physical phenomena proposed to explain these models, better constraints on the seismic data, probably using better-quality data and a wider geographical distribution of seismic stations in polar regions are urgently required.

In this chapter, our current knowledge of the seismic anisotropy of the constituent minerals of the Earth's interior and our ability to extrapolate these properties to mantle conditions of temperature and pressure (**Figure 1**) are reviewed. The chapter begins by reviewing the fundamentals of elasticity, plane wave propagation in anisotropic crystals, the measurements of elastic constants, and the effective elastic constants of crystalline aggregates.

## 2 Mineral Physics

### 2.1 Elasticity and Hooke's Law

Robert Hooke's experiments demonstrated that extension of a spring is proportional to the weight hanging from it which was published in *De Potentia Restitutiva* (or of Spring Explaining the Power of Springing Bodies 1678), establishing that in elastic solids there is a simple linear relationship between stress and strain. The relationship is now commonly known as Hooke's law (**Ut tensio, sic vis** – which translated from Latin is 'as is the extension, so is the force' – was the solution to an anagram announced two years early in 'A Description of Helioscopes and some other Instruments 1676', to prevent Hooke's rivals from claiming to have made the discovery themselves!). In the case of small (infinitesimal) deformations a Maclaurin expansion of stress as a function of strain developed to first order correctly describes the elastic behavior of most linear elastic solids:

$$\sigma_{ij}(\varepsilon_{kl}) = \sigma_{ij}(0) + \left(\frac{\partial \sigma_{ij}}{\partial \varepsilon_{kl}}\right)_{\partial \varepsilon_{kl}=0} \times \varepsilon_{kl} + \frac{1}{2}\left(\frac{\partial \sigma_{ij}}{\partial \varepsilon_{kl}\partial \varepsilon_{mn}}\right)_{\substack{\partial \varepsilon_{kl}=0 \\ \partial \varepsilon_{mn}=0}} \varepsilon_{kl}\varepsilon_{mn} + \cdots$$

as the elastic deformation is zero at a stress of zero then $\sigma_{ij}(0) = 0$ and restricting our analysis to first order, then we can define the fouth rank elastic tensor $c_{ijkl}$ as

$$c_{ijkl} = \left(\frac{\partial \sigma_{ij}}{\partial \varepsilon_{kl}}\right)_{\partial \varepsilon_{kl}=0}$$

where $\varepsilon_{kl}$ and $\sigma_{ij}$ are, respectively, the stress and infinitesimal strain tensors. Hooke's law can now be expressed in its traditional form as

$$\sigma_{ij} = c_{ijkl}\ \varepsilon_{kl}$$

The coefficients of the elastic fourth-rank tensor $c_{ijkl}$ translate the linear relationship between the second-rank stress and infinitesimal strain tensors. The four indices $(ijkl)$ of the elastic tensor have values between 1 and 3, so that there are $3^4 = 81$ coefficients. The stress tensor is symmetric as we assume that stresses acting on opposite faces are equal and opposite; hence, there are no stress couples to produce a net rotation of the elastic material. The infinitesimal strain tensor is also symmetric; because we assume that pure and simple shear quantities are so small that their squares and products can be neglected. Due to the symmetric symmetry of stress and infinitesimal strain tensors, they only have six independent values rather than nine for the nonsymmetric case; hence, the first two $(i,j)$ and second two $(k,l)$ indices of the elastic tensor can be interchanged:

$$c_{ijkl} = c_{jikl} \quad \text{and} \quad c_{ijkl} = c_{ijlk}$$

The permutation of the indices caused by the symmetry of stress and strain tensors reduces the number of independent elastic coefficients to $6^2 = 36$ because the two pairs of indices $(i,j)$ and $(k,l)$ can only have six different values:

$$1 \equiv (1,\ 1)\ 2 \equiv (2,\ 2)\ 3 \equiv (3,\ 3)\ 4 \equiv (2,\ 3) = (3,\ 2)\ 5 \equiv (3,\ 1) = (1,\ 3)\ 6 \equiv (1,\ 2) = (2,\ 1)$$

It is practical to write a 6 by 6 table of 36 coefficients with two Voigt indices $m$ and $n$ $(c_{mn})$ that have values between 1 and 6, whereas the representation of the $c_{ijkl}$ tensor with 81 coefficients would be a printer's nightmare. The relation between the Voigt (mn) and tensor indices $(ijkl)$ can be expressed most compactly by

$$m = \delta_{ij}\, i + \left(1 - \delta_{ij}\right)(9 - i - j) \quad \text{and}$$
$$n = \delta_{kl}\, k + (1 - \delta_{kl})(9 - k - 1)$$

where $\delta_{ij}$ is the Kronecker delta ($\delta_{ij} = 1$ when $i = j$ and $\delta_{ij} = 0$ when $i \neq j$).

Combining the first and second laws of thermodynamics for stress–strain variables we can define the variation of the internal energy $(\mathrm{d}U)$ per unit volume of a deformed anisotropic elastic body as a function of entropy $(\mathrm{d}S)$ and elastic strain $(\mathrm{d}\varepsilon_{ij})$ at an absolute temperature $(T)$ as

$$\mathrm{d}U = \sigma_{ij}\, \mathrm{d}\varepsilon_{ij} + T\, \mathrm{d}S$$

$U$ and $S$ are called state functions. From this equation it follows that the stress tensor at constant entropy can be defined as

$$\sigma_{ij} = \left(\frac{\partial U}{\partial \varepsilon_{ij}}\right)_S = c_{ijkl}\varepsilon_{kl}$$

hence

$$c_{ijkl} = \left(\frac{\partial \sigma_{ij}}{\partial \varepsilon_{kl}}\right) \quad \text{and} \quad c_{klij} = \left(\frac{\partial \sigma_{kl}}{\partial \varepsilon_{ij}}\right)$$

and finally we can write the elastic constants in terms of internal energy and strain as

$$c_{ijkl} = \frac{\partial}{\partial \varepsilon_{kl}}\left(\frac{\partial U}{\partial \varepsilon_{ij}}\right)_S = \left(\frac{\partial^2 U}{\partial \varepsilon_{ij}\partial \varepsilon_{kl}}\right)_S = \left(\frac{\partial^2 U}{\partial \varepsilon_{kl}\partial \varepsilon_{ij}}\right)_S = c_{klij}$$

The fourth-rank elastic tensors are referred to as second-order elastic constants in thermodynamics, because they are defined as second-order derivatives of a state function (e.g., internal energy $\partial^2 U$ for adiabatic or Helmhotz free energy $\partial^2 F$ for isothermal constants) with respect to strain. It follows from these thermodynamic arguments that we can interchange the first pair of indices $(ij)$ with second $(kl)$:

$$c_{ijkl} = c_{jikl} \quad \text{and} \quad c_{ijkl} = c_{ijlk} \quad \text{and now} \quad c_{ijkl} = c_{klij}$$

The additional symmetry of $c_{ijkl} = c_{klij}$ permutation reduces the number of independent elastic coefficients from 36 to 21 and tensor with two Voigt indices is symmetric, $c_{mn} = c_{nm}$. Although we have illustrated the case of isentropic (constant entropy, equivalent to an adiabatic process for a reversible process such as elasticity) elastic constants which intervene in the propagation of elastic waves whose vibration is too fast for thermal diffusion to establish heat exchange to achieve isothermal conditions, these symmetry relations are also valid for isothermal elastic constants which are used in mechanical problems. The vast majority of elastic constants reported in the literature are determined by the propagation ultrasonic elastic waves and are adiabatic. More recently, elastic constants predicted by atomic modeling for mantle conditions of pressure, and in some cases temperature, are also adiabatic (see review by Karki *et al.* (2001), also *see* Chapter 2.06).

The elastic constants in the literature are presented in the form of $6 \times 6$ tables for the triclinic symmetry with 21 independent values; here the

independent values are shown in bold characters in the upper diagonal of $c_{mn}$ with the corresponding $c_{ijkl}$

$$\begin{bmatrix} \mathbf{c_{11}} & \mathbf{c_{12}} & \mathbf{c_{13}} & \mathbf{c_{14}} & \mathbf{c_{15}} & \mathbf{c_{16}} \\ c_{12} & \mathbf{c_{22}} & \mathbf{c_{23}} & \mathbf{c_{24}} & \mathbf{c_{25}} & \mathbf{c_{26}} \\ c_{13} & c_{23} & \mathbf{c_{33}} & \mathbf{c_{34}} & \mathbf{c_{35}} & \mathbf{c_{36}} \\ c_{14} & c_{24} & c_{34} & \mathbf{c_{44}} & \mathbf{c_{45}} & \mathbf{c_{46}} \\ c_{15} & c_{25} & c_{35} & c_{45} & \mathbf{c_{55}} & \mathbf{c_{56}} \\ c_{16} & c_{26} & c_{36} & c_{46} & c_{56} & \mathbf{c_{66}} \end{bmatrix}$$

$$= \begin{bmatrix} \mathbf{c_{1111}} & \mathbf{c_{1122}} & \mathbf{c_{1133}} & \mathbf{c_{1123}} & \mathbf{c_{1113}} & \mathbf{c_{1112}} \\ c_{1122} & \mathbf{c_{2222}} & \mathbf{c_{2233}} & \mathbf{c_{2223}} & \mathbf{c_{2213}} & \mathbf{c_{2212}} \\ c_{1133} & c_{2233} & \mathbf{c_{3333}} & \mathbf{c_{3323}} & \mathbf{c_{3313}} & \mathbf{c_{3312}} \\ c_{1123} & c_{2223} & c_{3323} & \mathbf{c_{2323}} & \mathbf{c_{2313}} & \mathbf{c_{2312}} \\ c_{1113} & c_{2213} & c_{3313} & c_{2313} & \mathbf{c_{1313}} & \mathbf{c_{1312}} \\ c_{1112} & c_{2212} & c_{3312} & c_{2312} & c_{1312} & \mathbf{c_{1212}} \end{bmatrix}$$

In the triclinic system there are no special relationships between the constants. On the other extreme is the case of isotropic elastic symmetry defined by just two coefficients. Note this is not the same as cubic symmetry, where there are three coefficients and that a cubic crystal can be elastically anisotropic. The isotropic elastic constants can be expressed in the four-index system as

$$c_{ijkl} = \lambda\delta_{ij}\delta_{kl} + \mu\left(\delta_{ik}\delta_{jl} + \delta_{il}\delta_{jk}\right)$$

where $\lambda$ is Lamé's coefficient and $\mu$ is the shear modulus. $\lambda$ and $\mu$ are often referred to as Lamé's constants after the French mathematician Gabriel Lamé, who first published his book *Leçons sur la théorie mathématique de l'élasticité des corps solides* in 1852. In the two-index Voigt system the independent values are

$$c_{11} = c_{22} = c_{33} = \lambda + 2\mu$$

$$c_{12} = c_{23} = c_{13} = \lambda$$

$$c_{44} = c_{55} = c_{66} = \frac{1}{2}(c_{11} - c_{12}) = \mu$$

In matrix form this is written as

$$\begin{bmatrix} \mathbf{c_{11}} & \mathbf{c_{12}} & c_{12} & 0 & 0 & 0 \\ c_{12} & c_{11} & c_{12} & 0 & 0 & 0 \\ c_{12} & c_{12} & c_{11} & 0 & 0 & 0 \\ 0 & 0 & 0 & \frac{1}{2}(c_{11} - c_{12}) & 0 & 0 \\ 0 & 0 & 0 & 0 & \frac{1}{2}(c_{11} - c_{12}) & 0 \\ 0 & 0 & 0 & 0 & 0 & \frac{1}{2}(c_{11} - c_{12}) \end{bmatrix}$$

where the two independent values are $c_{11}$ and $c_{12}$. Another symmetry that is very important in seismology is the transverse isotropic medium (or hexagonal crystal symmetry). In many geophysical applications of transverse isotropy, the unique symmetry direction (X3) is vertical and the other perpendicular elastic axes (X1 and X2) are horizontal and share the same elastic properties and velocities. It is very common in seismological papers to use the notation of Love (1927) for the elastic constants of transverse isotropic media where

$$\mathbf{A} = \mathbf{c}_{11} = \mathbf{c}_{22} = \mathbf{c}_{1111} = \mathbf{c}_{2222}$$
$$\mathbf{C} = \mathbf{c}_{33} = \mathbf{c}_{3333}$$

$$\mathbf{F} = \mathbf{c}_{13} = \mathbf{c}_{23} = \mathbf{c}_{1133} = \mathbf{c}_{2233}$$

$$\mathbf{L} = \mathbf{c}_{44} = \mathbf{c}_{55} = \mathbf{c}_{2323} = \mathbf{c}_{1313}$$

$$\mathbf{N} = \mathbf{c}_{66} = \frac{1}{2}(\mathbf{c}_{11} - \mathbf{c}_{12}) = \mathbf{c}_{1212} = \frac{1}{2}(\mathbf{c}_{1111} - \mathbf{c}_{1122})$$

and

$$\mathbf{A} - 2\mathbf{N} = \mathbf{c}_{12} = \mathbf{c}_{21} = \mathbf{c}_{11} - 2\mathbf{c}_{66} = \mathbf{c}_{1212} = \mathbf{c}_{2211} = \mathbf{c}_{1111} - 2\mathbf{c}_{1212}$$

$$\begin{bmatrix} \mathbf{c_{11}} & \mathbf{c_{12}} & \mathbf{c_{13}} & 0 & 0 & 0 \\ c_{12} & c_{11} & c_{13} & 0 & 0 & 0 \\ c_{13} & c_{13} & \mathbf{c_{33}} & 0 & 0 & 0 \\ 0 & 0 & 0 & \mathbf{c_{44}} & 0 & 0 \\ 0 & 0 & 0 & 0 & c_{44} & 0 \\ 0 & 0 & 0 & 0 & 0 & \frac{1}{2}(\mathbf{c_{11}} - \mathbf{c_{12}}) \end{bmatrix}$$

$$= \begin{bmatrix} \mathbf{A} & \mathbf{A} - 2\mathbf{N} & \mathbf{F} & 0 & 0 & 0 \\ \mathbf{A} - 2\mathbf{N} & \mathbf{A} & \mathbf{F} & 0 & 0 & 0 \\ \mathbf{F} & \mathbf{F} & \mathbf{C} & 0 & 0 & 0 \\ 0 & 0 & 0 & \mathbf{L} & 0 & 0 \\ 0 & 0 & 0 & 0 & \mathbf{L} & 0 \\ 0 & 0 & 0 & 0 & 0 & \mathbf{N} \end{bmatrix}$$

and the velocities in orthogonal directions that characterize a transverse isotropic medium are functions of the leading diagonal of the elastic tensor and are given as

$$\mathbf{A} = \mathbf{c}_{11} = \rho V^2{}_{\mathrm{PH}}\mathbf{C} = \mathbf{c}_{33} = \rho V^2{}_{\mathrm{PV}}\mathbf{L} = \mathbf{c}_{44} = \rho V^2{}_{\mathrm{SV}}\mathbf{N} = \mathbf{c}_{66} = \rho V^2{}_{\mathrm{SH}}$$

where $\rho$ is density, $V_{\mathrm{PH}}$ and $V_{\mathrm{PV}}$ are the velocities of horizontally (X1 or X2) and vertically (X3) propagating P-waves, $V_{\mathrm{SH}}$ and $V_{\mathrm{SV}}$ are the velocities of horizontally and vertically polarized S-waves propagating horizontally.

Elastic anisotropy can be characterized by taking ratios of the individual elastic coefficients. Thomsen (1978) introduced three parameters to characterize the elastic anisotropy of any degree, not just weak anisotropy, for transverse isotropic medium,

$$\varepsilon = \mathbf{c}_{11} - \mathbf{c}_{33}/2\,\mathbf{c}_{33} = A - C/2C$$

$$\gamma = \mathbf{c}_{66} - \mathbf{c}_{44}/2\,\mathbf{c}_{44} = N - L/2L$$

and

$$\delta* = \frac{1}{2}\mathbf{c}^2{}_{33}\left[2(\mathbf{c}_{13}+\mathbf{c}_{44})^2 - (\mathbf{c}_{33}-\mathbf{c}_{44})(\mathbf{c}_{11}+\mathbf{c}_{33}-2\mathbf{c}_{44})\right]$$

$$\delta* = \frac{1}{2}C^2\left[2(F+L)^2 - (C-L)(A+C-2L)\right]$$

Thomsen also proposed a weak anisotropy version of the $\delta*$ parameter,

$$\delta = \left[(\mathbf{c}_{13}+\mathbf{c}_{44})^2 - (\mathbf{c}_{33}-\mathbf{c}_{44})^2\right]/[2\mathbf{c}_{33}(\mathbf{c}_{33}-\mathbf{c}_{44})] = \left[(F+L)^2 - (C-L)^2\right]/[2C(C-L)]$$

These parameters go to zero in the case of isotropy and have values of much less than 1 (i.e., 10%) in the case of weak anisotropy. The parameter $\varepsilon$ describes the P-wave anisotropy and can be defined in terms of the normalized difference of the P-wave velocity in the directions parallel to the symmetry axis (X3, vertical axis) and normal to the symmetry axis (X12, horizontal plane). The parameter $\gamma$ describes the S-wave anisotropy and can be defined in terms of the normalized difference of the SH-wave velocity in the directions normal to the symmetry axis (X12, horizontal plane) and parallel to the symmetry axis (X3, vertical axis), but also in terms SH and SV, because SH parallel to the symmetry axis has the same velocity as SV normal to the symmetry axis:

$$\varepsilon = V\mathrm{p}(\mathrm{X12}) - V\mathrm{p}(\mathrm{X3})/V\mathrm{p}(\mathrm{X3}) = V_{\mathrm{PH}} - V_{\mathrm{PV}}/V_{\mathrm{PV}}$$

$$\gamma = V_{\mathrm{SH}}(\mathrm{X12}) - V_{\mathrm{SH}}(\mathrm{X3})/V_{\mathrm{SH}}(\mathrm{X3}) = V_{\mathrm{SH}}(\mathrm{X12}) - V_{\mathrm{SV}}(\mathrm{X12})/V_{\mathrm{SV}}(\mathrm{X12}) = V_{\mathrm{SH}} - V_{\mathrm{SV}}/V_{\mathrm{SV}}$$

Thomsen (1986) found that the parameter $\delta*$ controls most of the phenomena of importance for exploration geophysics, such as velocities inclined to the symmetry axis (vertical), some of which are non-negliable even when the anisotropy is weak. The parameter $\delta*$ is an awkard combination of elastic parameters, which is totally independent of the velocity in the direction normal to the symmetry axis (X12 horizontal plane) and which may be either postitive or negative. Mensch and Rasolofosaon (1997) have extended the application of Thomsen's parameters to anisotropic media of arbitary symmetery and the associated analysis in terms of the perturbation of a reference model that can exhibit strong S-wave anisotropy.

In the domain of one- or three-dimensional radial anisotropic seismic tomography, it has been the practice to use the parameters $\varphi$, $\xi$, and $\eta$ to characterize the transverse anisotropy, where

$$\varphi = \mathbf{c}_{33}/\mathbf{c}_{11} = C/A = V_{\mathrm{PV}}{}^2/V_{\mathrm{PH}}{}^2$$

$$\xi = \mathbf{c}_{66}/\mathbf{c}_{44} = N/L = V_{\mathrm{SH}}{}^2/V_{\mathrm{SV}}{}^2$$

$$\eta = \mathbf{c}_{13}/(\mathbf{c}_{11}-2\mathbf{c}_{44}) = F/(A-2L)$$

For characterizing the anisotropy of the inner core, some authors (e.g., Song, 1997) use a variant of Thomsen's parameters, $\varepsilon'' = (\mathbf{c}_{33}-\mathbf{c}_{11})/2\mathbf{c}_{11} = (C-A)/2A$ (positions of $\mathbf{c}_{11}$ and $\mathbf{c}_{33}$ reversed from Thomsen, double prime has been added to avoid confusion here with Thomsen's parameter)

$$\gamma = (\mathbf{c}_{66}-\mathbf{c}_{44})/2\mathbf{c}_{44} = (N-L)/2L$$

(same as Thomsen)

$$\sigma = (\mathbf{c}_{11}+\mathbf{c}_{33}-4\mathbf{c}_{44}-2\mathbf{c}_{13})/2\mathbf{c}_{11} = (A+C-4L-2F)/2A$$

(very different from Thomsen's $\delta*$)

others (e.g., Woodhouse *et al.*, 1986) use

$$\alpha = (\mathbf{c}_{33}-\mathbf{c}_{11})/A_{\mathrm{o}} = (C-A)/A_{\mathrm{o}}$$

$$\beta = (\mathbf{c}_{66}-\mathbf{c}_{44})/A_{\mathrm{o}}$$

$$\gamma = (\mathbf{c}_{11}-2\mathbf{c}_{44}-\mathbf{c}_{13})/A_{\mathrm{o}} = (A-2N-F)/A_{\mathrm{o}}$$

where $A_{\mathrm{o}} = \rho_{\mathrm{o}}V\mathrm{p}_{\mathrm{o}}{}^2$ is calculated using the density $\rho_{\mathrm{o}}$ and P-wave velocity $V\mathrm{p}_{\mathrm{o}}$ at the center of the spherically symmetric reference Earth model, PREM (Dziewoński and Anderson, 1981). With at least four different sets of triplets of anisotropy parameters to describe transverse isotropy in various domains of seismology, the situation is complex for a researcher who wants to compare the anisotropy from different published works. Even when comparisons are made,

for example, for the inner core (Calvet *et al.*, 2006), drawing conclusions may be difficult as the parameters refect only certain aspects of the anisotropy.

In studying the effect of symmetry of the elastic properties of crystals, one is directly concerned with only the 11 Laue classes and not the 32 point groups, because elasticity is a centrosymmetrical physical property. The velocity of an elastic wave depends on its direction of propagation in an anisotropic crystal, but not the positive or negative sense of the direction. In this chapter we are restricting our study to second-order elastic constants, corresponding to small strains characteristic elastic deformations associated with the propagation of seismic waves. If we wanted to consider larger finite strains or the effect of an externally applied stress, we would need to consider third-order elastic constants as the approximation adopted in limiting the components of the strain tensor to terms of the first degree in the derviatives is no longer justified. For second-order elastic constants the two cubic and two hexagonal Laue classes are not distinct (e.g., Brugger, 1965) and may be replaced by a single cubic and a single hexagonal class, which results in only nine distinct symmetry classes for crystals shown in **Table 1**.

**Table 1** Second-order elastic constants of all Laue crystal symmetries

Cubic (3) 23, *m*3, 432, $\bar{4}3m$, *m*3*m*

$$\begin{bmatrix} c_{11} & c_{12} & c_{12} & 0 & 0 & 0 \\ c_{12} & c_{11} & c_{12} & 0 & 0 & 0 \\ c_{12} & c_{12} & c_{11} & 0 & 0 & 0 \\ 0 & 0 & 0 & c_{44} & 0 & 0 \\ 0 & 0 & 0 & 0 & c_{44} & 0 \\ 0 & 0 & 0 & 0 & 0 & c_{44} \end{bmatrix}$$

Hexagonal (5) 6, $\bar{6}$, 6/m, 622, 6*mmm*, $\bar{6}2$m, 6/*mmm*

$$\begin{bmatrix} c_{11} & c_{12} & c_{13} & 0 & 0 & 0 \\ c_{12} & c_{11} & c_{13} & 0 & 0 & 0 \\ c_{13} & c_{13} & c_{33} & 0 & 0 & 0 \\ 0 & 0 & 0 & c_{44} & 0 & 0 \\ 0 & 0 & 0 & 0 & c_{44} & 0 \\ 0 & 0 & 0 & 0 & 0 & \frac{1}{2}(c_{11}-c_{12}) \end{bmatrix}$$

Trigonal (6) 32, 3*m*, $\bar{3}m$

$$\begin{bmatrix} c_{11} & c_{12} & c_{13} & c_{14} & 0 & 0 \\ c_{12} & c_{11} & c_{13} & -c_{14} & 0 & 0 \\ c_{13} & c_{13} & c_{33} & 0 & 0 & 0 \\ c_{14} & -c_{14} & 0 & c_{44} & 0 & 0 \\ 0 & 0 & 0 & 0 & c_{44} & c_{14} \\ 0 & 0 & 0 & 0 & c_{14} & \frac{1}{2}(c_{11}-c_{12}) \end{bmatrix}$$

Trigonal (7) 3, $\bar{3}$

$$\begin{bmatrix} c_{11} & c_{12} & c_{13} & c_{14} & -c_{25} & 0 \\ c_{12} & c_{11} & c_{13} & -c_{14} & c_{25} & 0 \\ c_{13} & c_{13} & c_{33} & 0 & 0 & 0 \\ c_{14} & -c_{14} & 0 & c_{44} & 0 & c_{25} \\ -c_{25} & c_{25} & 0 & 0 & c_{44} & c_{14} \\ 0 & 0 & 0 & c_{25} & c_{14} & \frac{1}{2}(c_{11}-c_{12}) \end{bmatrix}$$

Tetragonal (6) 422, 4*mm*, $\bar{4}2m$, 4/*mmm*

$$\begin{bmatrix} c_{11} & c_{12} & c_{13} & 0 & 0 & 0 \\ c_{12} & c_{11} & c_{13} & 0 & 0 & 0 \\ c_{13} & c_{13} & c_{33} & 0 & 0 & 0 \\ 0 & 0 & 0 & c_{44} & 0 & 0 \\ 0 & 0 & 0 & 0 & c_{44} & 0 \\ 0 & 0 & 0 & 0 & 0 & c_{66} \end{bmatrix}$$

Tetragonal (7), 4, $\bar{4}$ 4/*m*

$$\begin{bmatrix} c_{11} & c_{12} & c_{13} & 0 & 0 & c_{16} \\ c_{12} & c_{11} & c_{13} & 0 & 0 & -c_{16} \\ c_{13} & c_{13} & c_{33} & 0 & 0 & 0 \\ 0 & 0 & 0 & c_{44} & 0 & 0 \\ 0 & 0 & 0 & 0 & c_{44} & 0 \\ c_{16} & -c_{16} & 0 & 0 & 0 & c_{66} \end{bmatrix}$$

(*Continued*)

**Table 1** (Continued)

Orthorhombic (9) 222, *mm*2, *mmm*

$$\begin{bmatrix} c_{11} & c_{12} & c_{13} & 0 & 0 & 0 \\ c_{12} & c_{22} & c_{23} & 0 & 0 & 0 \\ c_{13} & c_{23} & c_{33} & 0 & 0 & 0 \\ 0 & 0 & 0 & c_{44} & 0 & 0 \\ 0 & 0 & 0 & 0 & c_{55} & 0 \\ 0 & 0 & 0 & 0 & 0 & c_{66} \end{bmatrix}$$

Mononclinic (13) 2, *m*, 2/*m*

$$\begin{bmatrix} c_{11} & c_{12} & c_{13} & 0 & c_{15} & 0 \\ c_{12} & c_{22} & c_{23} & 0 & c_{25} & 0 \\ c_{13} & c_{23} & c_{33} & 0 & c_{35} & 0 \\ 0 & 0 & 0 & c_{44} & 0 & c_{46} \\ c_{14} & c_{25} & c_{35} & 0 & c_{55} & 0 \\ 0 & 0 & 0 & c_{46} & 0 & c_{66} \end{bmatrix}$$

Triclinic (21) 1, $\overline{1}$

$$\begin{bmatrix} c_{11} & c_{12} & c_{13} & c_{14} & c_{15} & c_{16} \\ c_{12} & c_{22} & c_{23} & c_{24} & c_{25} & c_{26} \\ c_{13} & c_{23} & c_{33} & c_{34} & c_{35} & c_{36} \\ c_{14} & c_{24} & c_{34} & c_{44} & c_{45} & c_{46} \\ c_{15} & c_{25} & c_{35} & c_{45} & c_{55} & c_{56} \\ c_{16} & c_{26} & c_{36} & c_{46} & c_{56} & c_{66} \end{bmatrix}$$

The number in brackets is the number of independent constants.

## 2.2 Plane Waves and Christoffel's Equation

There are two types of elastic waves, which propagate in an isotropic homogeneous elastic medium, the faster compressional (or longitudinal) wave with displacements parallel to propagation direction and slower shear (or transverse) wave with displacements perpendicular to the propagation direction. In anisotropic elastic media there are three types of waves:one compressional wave and two shear waves with, in general, different velocities. In order to understand the displacements associated with different waves, their relationship to the propagation direction and elastic anisotropy, it is important to consider the equation of propagation of a mechanical disturbance in an elastic medium. If we ignore the effect of gravity, we can write the equation of displacement ($u_i$) as function of time ($t$) as

$$\rho\left(\frac{\partial^2 u_i}{\partial t^2}\right) = \left(\frac{\partial \sigma_{ij}}{\partial x_j}\right)$$

where $\rho$ is the density and $x_j$ is position. Using Hooke's law, stress can be written as

$$\sigma_{ij} = c_{ijkl}\left(\frac{\partial u_l}{\partial x_k}\right)$$

Hence, elasto-dynamical equation describing the inertial forces can be rewritten with one unknown (the displacement) as

$$\rho\left(\frac{\partial^2 u_i}{\partial t^2}\right) = c_{ijkl}\left(\frac{\partial^2 u_l}{\partial x_j x_k}\right)$$

The displacement of monochromatic plane wave can be described by any harmonic form as a function of time (e.g. Fedorov, 1968):

$$u = A\exp \mathrm{i}(k.x - \omega t)$$

where $A$ the amplitude vector, which gives the direction and magnitude of particle motion, $t$ is time, $n$ the propagation direction normal to the plane wavefront, $\omega$ the angular frequency, which is related to frequency by $f = \omega/2\pi$, $k$ is the wave vector which is related to the phase velocity ($V$) by $V = \omega/k$ and the plane wavefront normal ($n$) by $k = (2\pi/\lambda)n$, where $\lambda$ is the wavelength. For plane waves the total phase $\phi = (k.x - \omega t)$ is a constant along the wavefront. Hence, the equation for a surface of equal phase at any instant of time ($t$) is a plane perpendicular to the propagation unit vector ($n$). Now if we insert the solution for the time-dependant displacement into the elasto-dynamical equation, we find the

Christoffel equation first published by E.B. Christoffel in 1877:

$$C_{ijkl}s_j s_l p_k = \rho V^2 p_i \quad \text{or} \quad C_{ijkl}s_j s_l p_k = \rho p_i$$

$$\left(C_{ijkl}n_j n_l - \rho V^2 \delta_{ik}\right)p_k = 0 \quad \text{or} \quad \left(C_{ijkl}s_j s_l - \rho \delta_{ik}\right)p_k = 0$$

where $V$ are the phase velocities, $\rho$ is density, $p_k$ polarization unit vectors, $n_j$ propagation unit vector, and $s_j$ are the slowness vector of magnitude $1/V$ and the same direction as the propagation direction ($n$). The polarization unit vectors $p_k$ are obtained as eigenvectors and corresponding eigenvalues of the roots of the equation

$$\det|C_{ijkl}n_j n_l - \rho V^2 \delta_{ik}| = 0 \quad \text{or}$$
$$\det|C_{ijkl}s_j s_l - \rho \delta_{ik}| = 0$$

We can simplify this equation by introducing the Christoffel (Kelvin–Christoffel or acoustic) tensor $T_{ik} = C_{ijkl}n_j n_l$ and three wave moduli $M = \rho V^2$; hence, $\det|T_{ik} - M\delta_{ik}| = 0$. The equation can be written in full as

$$\begin{vmatrix} T_{11} - M & T_{12} & T_{13} \\ T_{21} & T_{22} - M & T_{23} \\ T_{31} & T_{32} & T_{33} - M \end{vmatrix} = 0$$

which upon expansion yields the cubic polynominal in $M$

$$M^3 - \mathrm{I}_T M^2 + \mathrm{II}_T M - \mathrm{III}_T = 0$$

where $\mathrm{I}_T = T_{ii}$, $\mathrm{II}_T = \frac{1}{2}(T_{ii}T_{jj} - T_{ij}T_{ij})$, and $\mathrm{III}_T = \det|T_{ij}|$ are the first, second, and third invariants of the Christoffel tensor. The three roots of the cubic polynominal in $M$ are the three wave moduli $M$. The eigenvectors ($e_j$) associated with each wave moduli can be found by solving $(T_{ij} - M\delta_{ij})e_j = 0$. Analytical solutions for the Christoffel tensor have been proposed in various forms by Červený (1972), Every (1980), Mainprice (1990), Mensch and Rasolofosaon (1997), and probably others.

The Christoffel tensor is symmetric because of symmetry of the elastic constants, and hence

$$T_{ik} = C_{ijkl}n_j n_l = C_{jikl}n_j n_l = C_{ijlk}n_j n_l = C_{klij}n_j n_l = T_{ki}$$

The Christoffel tensor is also invariant upon the change of sign of the propagation direction ($n$) as the elastic tensor is not sensitive to the presence or absence of a center of symmetry, being a centro-symmetric physical property. Because the elastic strain energy ($(1/2)C_{ijkl}\varepsilon_{ij}\varepsilon_{kl}$) of a stable crystal is always positive and real (e.g., Nye, 1957), the eigenvalues of the $3 \times 3$ Christoffel tensor (being a Hermitian matrix) are three positive real values of the wave moduli ($M$) corresponding to $\rho {V_\mathrm{p}}^2$, $\rho {V_\mathrm{s1}}^2$, $\rho {V_\mathrm{s2}}^2$ of the plane waves propagating in the direction $n$. The three eigenvectors of the Christoffel tensor are the polarization directions (also called vibration, particle movement or displacement vectors) of the three waves. As the Christoffel tensor is symmetric, the three eigenvectors (and polarization) vectors are mutually perpendicular. In the most general case, there are no particular angular relationships between polarization directions ($p$) and the propagation direction ($n$); however, typically the P-wave polarization direction is nearly parallel and the two S-waves polarizations are nearly perpendicular to the propagation direction and they are termed quasi-P or quasi-S waves. If polarizations of the P-wave and two S-waves are, respectively, parallel and perpendicular to the propagation direction, which may happen along a symmetry direction, then the waves are termed pure P and pure S or pure modes. Only velocities in pure mode directions can be directly related to single elastic constants (Neighbours and Schacher, 1967). In general, the three waves have polarizations that are perpendicular to one another and propagate in the same direction with different velocities, with $V_\mathrm{p} > V_\mathrm{s1} > V_\mathrm{s2}$. A propagation direction for which two (or all three) of the phase velocities are identical is called an acoustic axis, which occur even in crystals of triclinic symmetry. Commonly, the acoustic axis is associated with the two S-waves having the same velocity. The S-wave may be identified by their relative velocity $V_\mathrm{s1} > V_\mathrm{s2}$ or by their polarization being parallel to a symmetry direction or feature, for example, SH and SV, where the polarization is horizontal and vertical to the third axis of reference Cartesian frame of the elastic tensor (X3 in the terminology of Nye (1957), X3 is almost always parallel to the crystal $c$-axis) in mineral physics and perpendicular to the Earth's surface in seismology.

The velocity at which energy propagates in a homogenous anisotropic elastic medium is defined as the average power flow density divided by average total energy density and can be calculated from the phase velocity using the following relationship given by Fedorov (1968):

$${V_i}^\mathrm{e} = C_{ijkl}p_j p_l n_k / \rho V$$

The phase and energy velocities are related by a vector equation ${V_i}^\mathrm{e} \cdot n_i = V_i$. It is apparent from this relationship that $V^\mathrm{e}$ is not in general parallel to

propagation direction ($n$) and has a magnitude equal or greater to the phase velocity ($V = \omega/k$). The propagation of waves in real materials occurs as packets of waves typically having a finite band of frequencies. The propagation velocity of wave packet is called the group velocity and this is defined for plane waves of given finite frequency range as

$$V_i^g = (\partial\omega/\partial k_i)$$

The group velocity is in general different to the phase velocity except along certain symmetry directions. In lossless anisotropic elastic media the group and energy velocities are identical (e.g., Auld, 1990); hence, it is not necessary to evaluate the differential angular frequency versus wave vector to obtain the group velocity as $V^g = V^e$. The group velocity has direct measurable physical meaning that is not apparent for the energy or phase velocities.

Various types of plots have been used to illustrate the variation of velocity with direction in crystals. Velocities measured by Brillouin spectroscopy are displayed via graphs of velocity as a function of propagation directions used in the experiments. The phase velocities $V_p$,$V_{sh}$, and $V_{sv}$ of Stishovite are shown in **Figure 3**, using the elastic constants from Weidner *et al.* (1982); although this type of plot may be useful for displaying the experimental results, it does not convey the symmetry of the crystal. In crystal acoustics, the phase velocity and slowness surfaces have traditionally illustrated the anisotropy

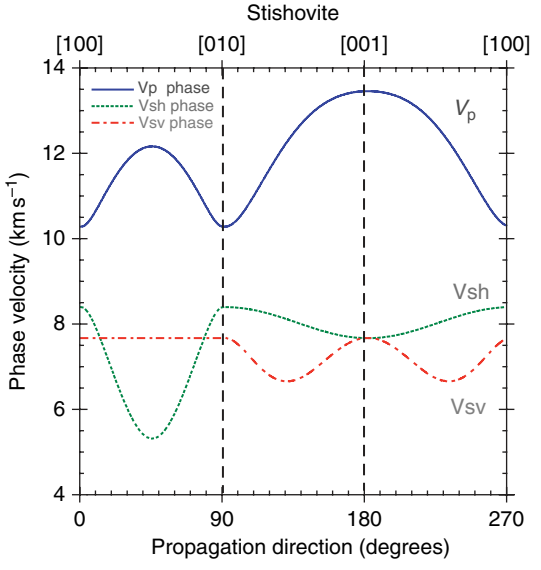


**Figure 3** The variation of velocity with direction for tetragonal Stishovite as described by Weidner *et al*. (1982).

of elastic wave velocity in crystals as a function of the propagation direction ($n$) and plots of the wavefront (ray or group) surface given by tracing the extremity of the energy velocity vector defined above. The normal to the slowness surface has the special property of being parallel to the energy velocity vector. The normal to the wavefront surface has the special property of being parallel to the propagation ($n$) and wave vector ($k$). We can illustrate these polar reciprocal properties using the elastic constants of the h.c.p. $\varepsilon$-phase of iron, which is considered to be the major constituent of the inner core, determined by Mao *et al.* (1998) at high pressure (**Figure 4**). Note that the twofold symmetry along the **a**$[2\bar{1}\bar{1}0]$ axis of hexagonal $\varepsilon$-phase is respected by the slowness and wavefront surfaces of the SH-waves. The wavefront surface can be regarded as a recording after 1 s of the propagation from a spherical point source at the center of the diagram. The wavefront is a surface that separates the disturbed regions from the undisturbed ones. Anisotropic media have velocities that vary with direction, and hence the phase velocity and the slowness surfaces with concave and convex undulations in three dimensions. The undulations are not sharp as velocities and slownesses change slowly with orientation. In contrast, the wave surface can have sharp changes in direction, called cusps or folded wave surfaces in crystal physics (e.g., Musgrave, 2003) and triplications or caustics in seismology (e.g.,Vavrycuk, 2003), particularly for S-waves, which correspond in orientation to undulations in the phase velocity and slowness surfaces. The high-pressure form of $SiO_2$ called Stishovite illustrates the various facets of the phase velocity, slowness, and wavefront surfaces in a highly anisotropic mineral

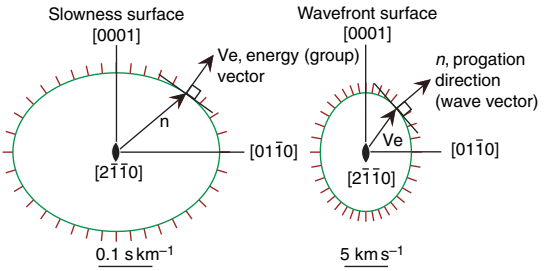


**Figure 4** The polar reciprocal relation between the slowness and wavefront surfaces in hexagonal $\varepsilon$-phase iron at 211 GPa using the elastic constants determined by Mao *et al*. (1998). The normal to the slowness surface is the energy vector (brown) and the normal to the wavefront surface is the propagation direction (parallel to the wave vector). Note the twofold symmetry on the surfaces.

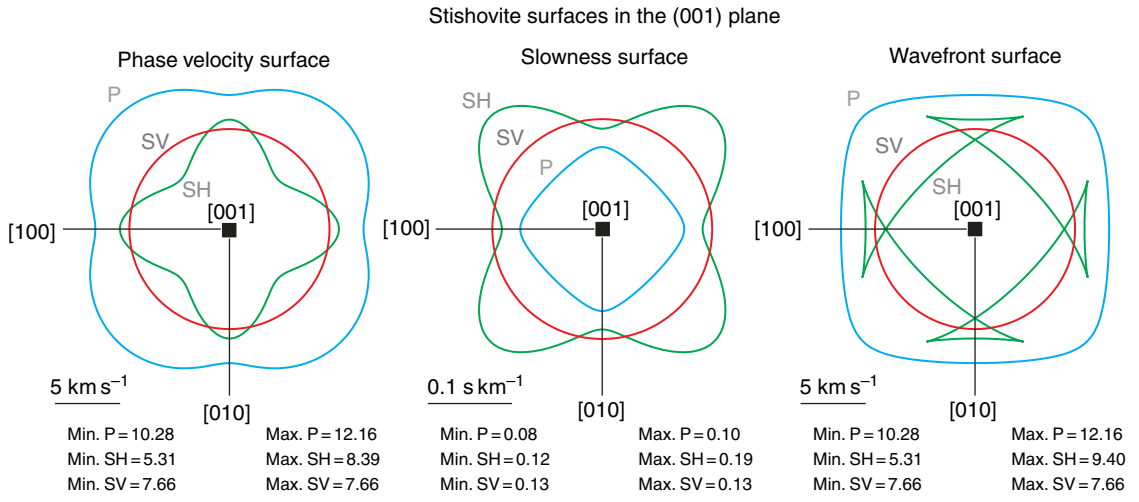


**Figure 5** The three surfaces used to characterize acoustic properties, the phase velocity, slowness, and wavefront surfaces for tetragonal Stishovite. Note fourfold symmetry of the surfaces and the cusps on the SH wavefront surface. The elastic constants of Stishovite were measured by Weidner *et al*. (1982) at ambiante conditions.

(**Figure 5**). Velocity clearly varies strongly with propagation direction; in the case of Stishovite, the variation for SH is very important, whereas SV is constant in the (001) plane. Stishovite has tetragonal symmetry; hence, the *c*-axis has fourfold symmetry that can clearly be identified in the various surfaces in (001) plane. There are orientations where the SH and SV surfaces intersect; hence, there is no shear wave splitting (S-wave birefringence) as both S-waves have the same velocity. The phase velocity and slowness surfaces have smooth changes in orientation corresponding to gradual changes in velocity. In contrast, along the **a**[100] and **b**[010] directions, the SH wavefront has sharp variations in orientation called cusps. The cusps on the SH wavefront are shown in more detail in **Figure 6**, where the cusps on the wavefront are clearly related to minima of the slowness (or maxima on the phase velocity) surface. The propagation of SH in the **a**[100] direction is instructive; if one considers seismometer at the point S, then seismometer will record first the arrival of wavefront AA′, then BB′ and finally CC′. The parabolic curved nature of the cusp AA′ is also at the origin of the word caustic to describe this phenomena by analogy with the convergent rays in optics, whereas the word triplication evokes the arrival of the three wavefronts. Although we are dealing with homogeneous anisotropic medium, a single crystal of stishovite, the seismometer will record three arrivals for SH, plus of course SV and P, giving

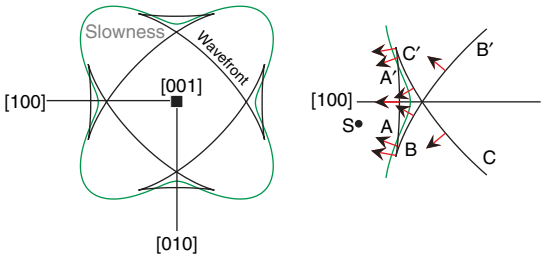


**Figure 6** Cusps on the wavefront surface of tetragonal Stishovite and its relation to the slowness surface in the [100] direction. The propagation directions of the wavefront are marked by arrows every 10° (see the text for detailed discussion).

a total of five arrivals for a single mechanical disturbance. Media with tetragonal elastic symmetry are not very common in seismology, whereas media with hexagonal (or transverse isotropic) symmetry are very common and has been postulated, for example, for the D″ layer above the core–mantle boundary (CMB) (e.g., Kendall, 2000). The three surfaces of the hexagonal $\varepsilon$-phase of iron are shown in **Figure 7** in the **a**$(2\bar{1}\bar{1}0)$ and **c**(0001) planes, which are respectively the perpendicular and parallel to the elastic symmetry axis (*c*-axis or X3) of transverse isotropic elastic symmetry. First, in this chapter the wave properties in the **a**$(2\bar{1}\bar{1}0)$ plane are considered. In this plane the maximum P-wave velocity is 45° from the *c*-axis and minimum parallel to the *a*- and

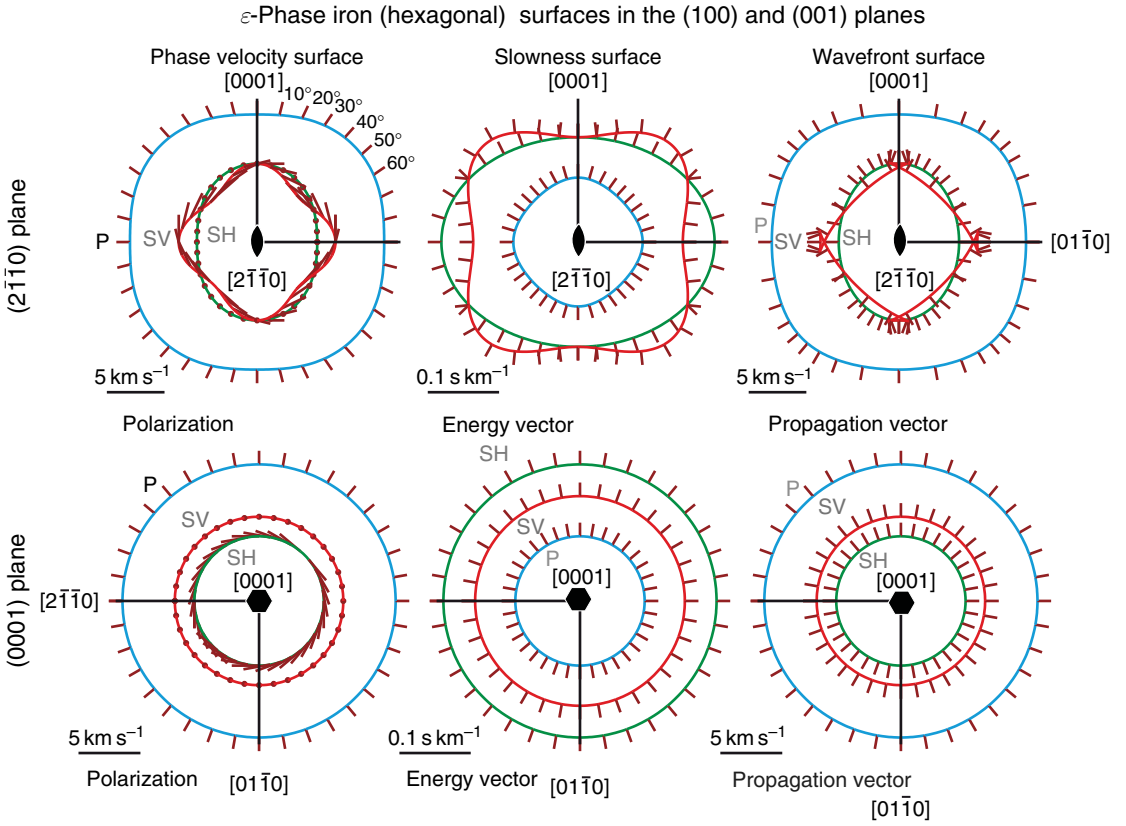


**Figure 7** Velocity surfaces of ε-phase of iron in the second-order prism and basal plane illustrating the anisotropy in a hexagonal or transverse isotropic structure. Note the perfectly isotropic (circular) velocity surfaces in the base plane. The polarizations are marked on the phase velocity surfaces and for the basal plane the polarizations for P are normal to the surface and parallel to the propagation direction, where as for S they are normal and vertical for SV and tangential and horizontal for SH as in an isotropic medium. The energy vector and propagation direction are normal to the slowness and wavefront surface in the basal plane.

*c*-axes. The maximum SH velocity is parallel to the *c*-axis and the minimum parallel to *b*-axis, where as the SV velocity has a maximum parallel to the *a*- and *c*-axes and a minimum 45° to the *c*-axis. The polarization direction of P-waves is not perpendicular to the phase velocity surface in general, and not parallel to the propagation direction, except along the symmetry directions **m**[01$\bar{1}$0] and **c**[0001] axes. The SH polarizations are all normal to the *c*-axis and hence they appear as points in the **a**(2$\bar{1}\bar{1}$0) plane. The SV polarizations are inclined to the *a*-axis; hence, they appear as lines of variable length depending on their orientation. The SH and SV velocity surfaces intersect parallel to the *c*-axis and at 60° from the *c*-axis, where they have the same velocity. The minima in the SV slowness surface along the *a*-and *c*-axes correspond to the cusps seen on the wavefront surface. The wave properties in the (0001) plane are completely different as both the P- and S-waves display a single velocity, hence the name transverse isotropy as the velocities do not vary with direction in this plane perpendicular (transverse) to the unique elastic symmetry axis (*c*-axis or X3). The isotropic nature of this plane is also shown by the polarizations of the P-waves, which are normal to the phase velocity surface, and parallel to the propagation direction, as in the isotropic case. Similarly for the S-waves, the polarization directions for SV are parallel and SH are normal to the symmetry axis, and both are perpendicular to the propagation direction.

The illustrations used so far are only two-dimensional sections of the anisotropic wave properties. Ideally, we would like to see the three-dimensional form of the velocity surfaces and polarizations. A three-dimensional plot of the P, SH, and SV velocities in **Figure 8** shows the geometrical relation of the polarizations to the crystallographic axes, but is too complicated to see the variation in velocities; only a few directions have been plotted for clarity.

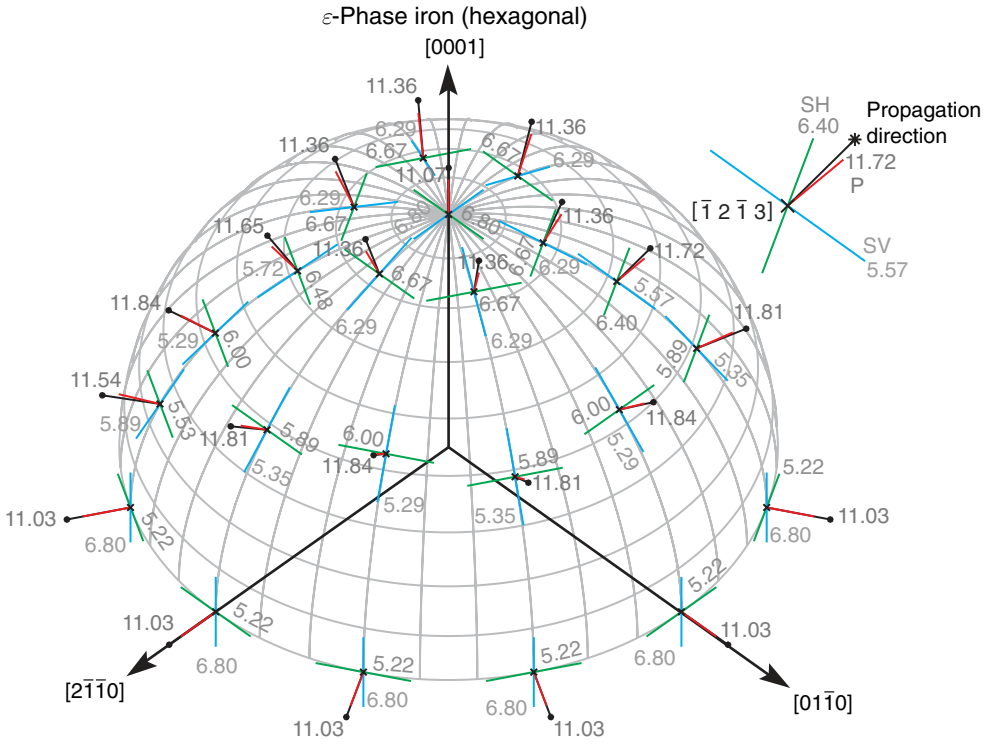


**Figure 8** A three-dimensional illustration of the propagation direction (black), P-wave polarization (red), SH-wave (green), and SV-wave (blue) in hexagonal $\varepsilon$-phase iron at 211 GPa. The sphere is marked with grid at 10° intervals. The SH-wave polarizations are organized around the [001] direction in a hexagonal pattern. The P-wave polarization is not in general parallel and hence the S-wave polarizations are not perpendicular to the propagation, as illustrated for the [1213] direction. However, along symmetry directions, such as [$2\bar{1}\bar{1}0$], the P-wave polarization is parallel and hence the S-wave polarizations are perpendicular to the propagation.

A more practical representation that is directly related to spherical plot in **Figure 8** is the pole figure plot of contoured and shaded velocities with polarizations shown in **Figure 9**. The circular nature of the velocity and polarization around the sixfold symmetry axis **c**[0001] is immediately apparent. The maximum shear wave splitting and SV velocity is in the basal (0001) plane. From the plot we can see that $\varepsilon$-phase of iron is very anisotropic at the experimental conditions of Mao *et al.* (1998) with a P-wave anisotropy of 7.1%. The shear wave anisotropy has a maximum of 26.3%, because in this transverse isotropic structure, SH has a minimum and SV has a maximum velocity in the basal plane. At first sight the pole figure plot of polarizations appears complex. To illustrate the representation of S-wave polarizations on a pole figure a single propagation direction in **Figure 10** has been drawn. In this chapter, stishovite has been chosen as an example mineral because it is very anisotropic and hence the angles between the polarizations are clearly not parallel (qP) or pendicular (qS1, qS2) to the propagation direction.

## 2.3 Measurement of Elastic Constants

Elastic properties can be measured by a various methods, including mechanical stress–strain, ultrasonic, resonant ultrasound spectroscopy Brillouin spectroscopy, nonhydrostatic radial X-ray diffraction, X-ray and neutron inelastic scattering, and shock measurements. In addition to physical measurements, atomic scale first-principles methods can predict elastic properties of crystals (see review by Karki *et al.* (2001), also *see* Chapter 2.06). The classical mechanical stress–strain measurements of elastic constants are no longer used due to the large errors and most compilations of single-crystal elastic constants (e.g., Bass, 1995; Isaak, 2001) are mainly based on ultrasonic measurements, the traditional technique at ambient conditions for large specimens. The measurement of the elastic constants for minerals from the deep Earth using classical techniques requires large (<1 $cm^3$) gem quality crystals. However, many minerals of the deep Earth are not stable, or meta-stable, at ambient conditions and no large gem quality crystals are available. Furthermore, the main applications of elastic constants

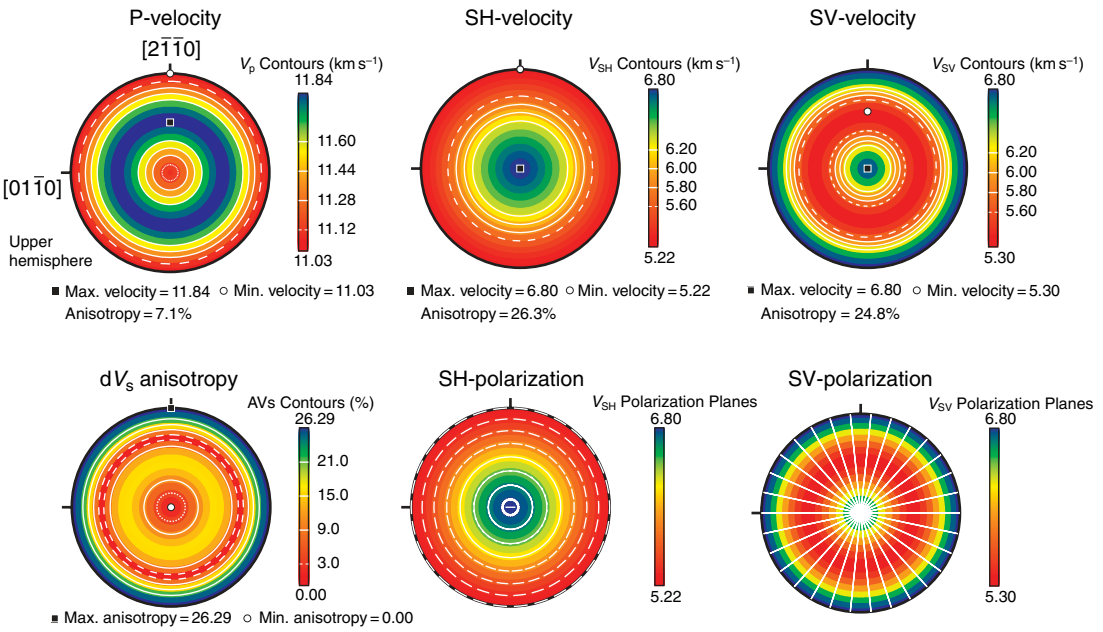


**Figure 9** The pole figure of plot for hexagonal $\varepsilon$-phase iron where the circular symmetry around the [0001] axis is clearly visible for velocities, d$V_s$ anisotropy and S-wave polarizations.

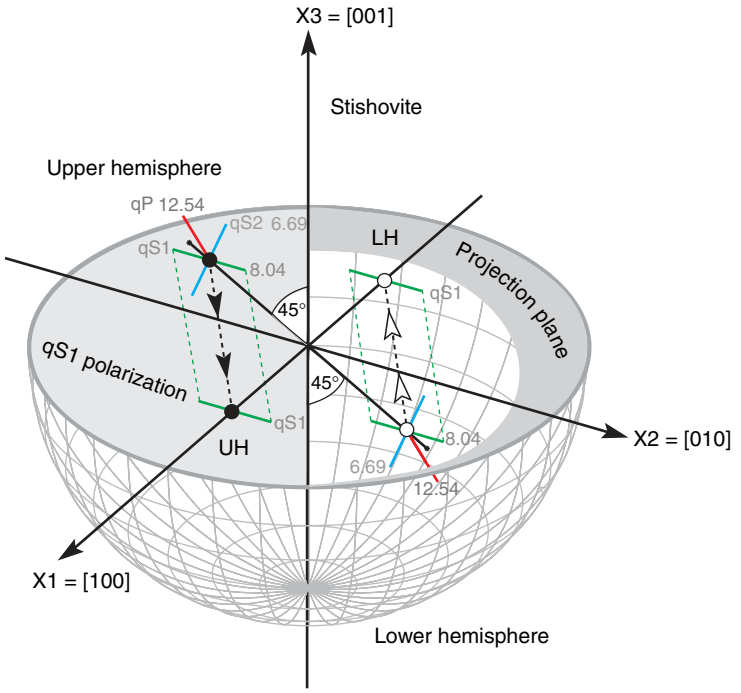


**Figure 10** The pole figure of plot for strongly anisotropic stishovite illustrating the projection of the qS1 polarization onto the equatorial plane of projection. On the left-hand side the upper hemisphere projection down on to the equatorial plane is shown. On the right-hand side the lower hemisphere projection up toward the equatorial plane is shown. The velocities and the polarizations for qP, qS1, and qS2 have the same velocities (in km s$^{-1}$) and orientations, respectively, for the propagation direction in the positive (upper hemisphere) or negative (lower hemisphere) sense due to the centrosymmetic property of elasticity. Note that the change from an upper hemisphere to lower hemisphere projection for a centrosymmetic property is achieved by a 180° rotation in azimuth around X3.

are for the interpretation of seismological data at the high pressure and temperature conditions of the Earth's mantle and core. Although ultrasonic techniques are still widely used, new methods are constantly being developed and refined for measurements at higher pressures and temperatures (Liebermann and Li, 1998; Li *et al.*, 2004; Jacobsen *et al.*, 2005).

Ultrasonic measurements require a mechanical contact between the transducers that produce and detect the ultrasonic signal and the sample. For experiments at high pressure and temperature the contact is generally made via the high-pressure pistons and a high-temperature ceramic buffer rod or directly with the diamond anvils. Various corrections are necessary to take into account the ray paths through the pistons and buffer rods and transducer-bond phase shift effects. The technique most commonly used is based on the ultrasonic interferometry method introduced by Jackson and Niesler (1982) to obtain accurate pressure derivatives of single-crystal MgO to 3 GPa in a piston cylinder apparatus. The use of ultrasonic interferometry in conjunction with synchrotron X-radiation in multianvil devices permits a more accurate measurement of elastic constants at simultaneous high pressure and temperature (Li *et al.*, 2004), as the sample length can be directly measured by X-radiography *in situ*, thereby reducing uncertainties in velocity measurements. A new gigahertz ultrasonic interferometer has recently been developed for the diamond anvil cell (Jacobsen *et al.*, 2005). The gigahertz frequency reduces the wavelength in minerals to a few micrometers, which allows the determination of velocity and the elastic constants for samples of a few tens of micrometers in thickness. Another ultrasonic technique called resonant ultrasound spectroscopy has been used to study the elastic constants of minerals with high precision to very high temperatures at ambient pressure (e.g., Isaak, 1992; Isaak *et al.*, 2005).

Brillouin scattering spectroscopy has become an established tool for measuring elastic constants since the introduction of laser sources and multipass Fabry–Perot interferometers (e.g., Vacher and Boyer, 1972). Unlike the ultrasonic techniques which usually measure the velocity in relatively few crystallographic directions, and where possible in pure mode directions, using Brillouin scattering the velocities can be measured along many propagation directions and the numerous velocities are inverted to obtain a least-squares determination of the elastic constants (Weidner and Carleton, 1977); hence, it is very suitable for the measurement of low-symmetry crystals. Brillouin scattering has several advantages for measurements of transparent minerals at high pressure and temperature in a diamond anvil cell; it only requires a small sample; no physical contact with the sample is required and the Brillouin peaks increase with temperature (Sinogeikin *et al.*, 2005). The elastic constants of MgO have been determined to high pressure (55 Gpa; Zha *et al.*, 2000) and high temperature (1500 K; Sinogeikin *et al.*, 2005) using Brillouin scattering. A related technique using laser-induced phonon spectroscopy in the form of impulsive scattering in a diamond anvil cell has been used to measure elastic constants of mantle minerals to 20 GPa (e.g., Chai *et al.*, 1977, 1997; Abramson *et al.*, 1997).

Several X-ray and neutron diffraction and scattering techniques (e.g., Fiquet *et al.*, 2004) have recently been developed to explore elastic behavior at extreme pressures (>100 GPa) in diamond anvils. Experiments using X-ray radial diffraction of polycrystalline samples under nonhydrostatic stress have been used to estimated the single-crystal elastic constants by using the measured lattice strains and crystal-preferred orientation combined with model polycrystalline stress distribution (e.g., Voigt or Reuss) (e.g., Mao *et al.*, 1998; Merkel *et al.*, 2005, 2006b). The uncertainties in the absolute value of the elastic constants may be on the order of 10–20% and model-dependent stress or strain distributions may be limited by the presence of elastic and plastic strain in some cases; however, this technique provides valuable information at extreme pressures. Inelastic X-ray scattering has provided volume averaged P-wave velocities of h.c.p. iron as a function of pressure to 110 GPa (Fiquet *et al.*, 2001). Using knowledge of the CPO combined with different scattering geometries, Antonangeli *et al.* (2004) have determined the P-wave velocities in several directions and $C_{11}$ elastic constant of h.c.p. iron, providing a valuable independent validation of results from radial diffraction. The nuclear-resonant inelastic X-ray scattering technique provides a direct probe of the phonon density of states. By the integration of the measured phonon density of states, the elastic and thermodynamic parameters are obtained; when combined with a thermal equation of state, the P- and S-wave velocities of h.c.p. iron have been determined to 73 GPa and 1700 K in a laser-heated diamond anvil cell by Lin *et al.* (2005), illustrating the rapid progress in this area.

## 2.4 Effective Elastic Constants for Crystalline Aggregates

The calculation of the physical properties from microstructural information (crystal orientation, volume fraction, grain shape, etc.) is important for upper-mantle rocks because it gives insight into the role of microstructure in determining the bulk properties; it is also important for synthetic aggregates experimentally deformed at simulated conditions of the Earth's interior. A calculation can be made for the *in situ* state at high temperature and pressure of the deep Earth for samples where the microstructure has been changed by subsequent chemical alteration (e.g., the transformation olivine to serpentine) or mechanically induced changes (e.g., fractures created by decompression). The *in situ* temperatures and pressures can be simulated using the appropriate single-crystal derivatives. Additional features not necessarily preserved in the recovered microstructure, such as the presence of fluids (e.g., magma) can be modeled (e.g., Blackman and Kendall, 1997; Mainprice, 1997; Williams and Garnero, 1996). Finally, the effect of phase change on the physical properties can also be modeled using these methods (e.g., Mainprice *et al.*, 1990). Modeling is essential for anisotropic properties as experimental measurements in many directions necessary to fully characterize anisotropy are not currently feasible for the majority of the temperature and pressure conditions found in the deep Earth.

In the following, we will only discuss the elastic properties needed for seismic velocities, but the methods apply to all tensorial properties where the bulk property is governed by the volume fraction of the constituent minerals. Many properties of geophysical interest are of this type, for example, thermal conductivity, thermal expansion, elasticity and seismic velocities. However, these methods do not apply to properties determined by the connectivity of a phase, such as the electrical conductivity of rocks with conductive films on the grain boundaries (e.g., carbon). We will assume that the sample may be microscopically heterogeneous due to grain size, shape, orientation, or phase distribution, but will be considered macroscopically uniform. The complete structural details of the sample are in general never known, but a 'statistically uniform' sample contains many regions, which are compositionally and structurally similar, each fairly representative of the entire sample. The local stress and strain fields at every point $\mathbf{r}$ in a linear elastic polycrystal completely determined by Hooke's law are as follows:

$$\sigma_{ij}(\mathbf{r}) = C_{ijkl}(\mathbf{r})\varepsilon_{kl}(\mathbf{r})$$

where $\sigma_{ij}(\mathbf{r})$is the stress tensor, $C_{ijkl}(\mathbf{r})$ is the elastic stiffness tensor, and $\varepsilon_{kl}(\mathbf{r})$ the strain tensor at point $\mathbf{r}$. The evaluation of the effective constants of a polycrystal would be the summation of all components as a function of position, if we know the spatial functions of stress and strain. The average stress $<\sigma>$ and strain $<\varepsilon>$ of a statistically uniform sample are linked by an effective macroscopic modulus $C^*$ that obeys Hookes's law of linear elasticity,

$$C^* = <\sigma><\varepsilon>^{-1}$$

where

$$<\varepsilon> = \frac{1}{V}\int \varepsilon(r)\,\mathrm{d}r$$

and

$$<\sigma> = \frac{1}{V}\int \sigma(r)\,\mathrm{d}r$$

and $V$ is the volume, the notation $<>$ denotes an ensemble average. The stress $\sigma(\mathbf{r})$ and strain $\varepsilon(\mathbf{r})$ distribution in a real polycrystal varies discontinuously at the surface of grains. By replacing the real polycrystal with a 'statistically uniform' sample, we are assuming that $\sigma(\mathbf{r})$ and strain $\varepsilon(\mathbf{r})$ are varying slowly and continuously with position $\mathbf{r}$.

A number of methods are available for determining the effective macroscopic effective modulus of an aggregate. We will briefly present these methods which try to take into account an increasing amount of microstructural information, which of course results in increasing theoretical complexity, but yields estimates which are closer to experimental values. The methods can be classified by using the concept of the order of the statistical probability functions used to quantitatively describe the microstructure (Kröner, 1978). A zero-order bound is given when one has no statistical information of the microstructure of the polycrystal and for example we do not know the orientation of the component crystals; in this case we have to use the single-crystal properties. The maximum and minimum of the single-crystal property are the zero-order bounds. The simplest and best-known averaging techniques for obtaining estimates of the effective elastic constants of polycrystals are the Voigt (1928) and Reuss (1929) averages. These averages only use the volume fraction of each phase, the orientation and the elastic constants of the single crystals or grains. In terms of statistical probability functions, these are first-order bounds as only the first-order correlation function is used, which is the

volume fraction. Note no information about the shape or position of neighboring grains is used. The Voigt average is found by simply assuming that the strain field is everywhere constant (i.e., $\varepsilon(\mathbf{r})$ is independent of $\mathbf{r}$). The strain at every position is set equal to the macroscopic strain of the sample. $C^*$ is then estimated by a volume average of local stiffnesses $C(\mathbf{g}_i)$ with orientation $\mathbf{g}_i$, and volume fraction $V_i$,

$$C^* \approx C^{\text{Voigt}} = \left[\sum_i V_i C(\mathbf{g}_i)\right]$$

Reuss average is found by assuming that the stress field is everywhere constant. The stress at every position is set equal to the macroscopic stress of the sample. $C^*$ or $S^*$ is then estimated by the volume average of local compliances $S(\mathbf{g}_i)$,

$$C^* \approx C^{\text{Reuss}} = \left[\sum_i V_i S(\mathbf{g}_i)\right]^{-1}$$

$$S^* \approx S^{\text{Reuss}} = \left[\sum_i V_i S(\mathbf{g}_i)\right]$$

$$C^{\text{Voigt}} \neq C^{\text{Reuss}} \quad \text{and} \quad C^{\text{Voigt}} \neq \left[S^{\text{Reuss}}\right]^{-1}$$

These two estimates are not equal for anisotropic solids with the Voigt being an upper bound and the Reuss a lower bound. A physical estimate of the moduli should lie between the Voigt and Reuss average bounds as the stress and strain distributions are expected to be somewhere between uniform strain (Voigt bound) and uniform stress (Reuss bound). Hill (1952) observed that arithmetic mean (and the geometric mean) of the Voigt and Reuss bounds, sometimes called the Hill or Voigt–Reuss–Hill (VRH) average, is often close to experimental values. The VRH average has no theoretical justification. As it is much easier to calculate the arithmetic mean of the Voigt and Reuss elastic tensors, all authors have tended to apply the Hill average as an arithmetic mean. In Earth sciences, the Voigt, Reuss, and Hill averages have been widely used for averages of oriented polyphase rocks (e.g., Crosson and Lin, 1971). Although the Voigt and Reuss bounds are often far apart for anisotropic materials, they still provide the limits within which the experimental data should be found.

Several authors have searched for a geometric mean of oriented polycrystals using the exponent of the average of the natural logarithm of the eigenvalues of the stiffness matrix (Matthies and Humbert, 1993). Their choice of this averaging procedure was guided by the fact that the ensemble average elastic stiffness $<C>$ should equal the inverse of the ensemble average elastic compliances $<S>^{-1}$, which is not true, for example, of the Voigt and Reuss estimates. A method of determining the geometric mean for arbitrary orientation distributions has been developed (Matthies and Humbert, 1993). The method derives from the fact that a stable elastic solid must have an elastic strain energy that is positive. It follows from this that the eigenvalues of the elastic matrix must all be positive. Comparison between Voigt, Reuss, Hill, and self-consistent estimates shows that the geometric mean provides estimates very close to the self-consistent method, but at considerably reduced computational complexity (Matthies and Humbert, 1993). The condition that the macroscopic polycrystal elastic stiffness $<C>$ must equal the inverse of the aggregate elastic compliance $<S>^{-1}$ would appear to be a powerful physical constraint on the averaging method (Matthies and Humbert, 1993). However, the arithmetic (Hill) and geometric means are very similar (Mainprice and Humbert, 1994), which tends to suggest that they are just mean estimates with no additional physical significance.

The second set of methods use additional information on the microstructure to take into account the mechanical interaction between the elastic elements of the microstructure. Mechanical interaction will be very important for rocks containing components of very different elastic moduli, such as solids, liquids, gases, and voids. The most important approach in this area is the 'self-consistent' (SC) method (e.g., Hill, 1965). The SC method was introduced for materials with a high concentration of inclusions where the interaction between inclusions is significant. In the SC method, an initial estimate of the anisotropic homogeneous background medium of the polycrystal is calculated using the traditional volume averaging method (e.g.,Voigt). All the elastic elements ( grains, voids, etc.) are inserted into the background medium using Eshelby's (1957) solution for a single ellipsoidal inclusion in an infinite matrix. The elastic moduli of the ensemble, inclusion, and background medium are used as the 'new' background medium for the next inclusion. The procedure is repeated for all inclusions and repeated in an iterative manner for the polycrystal until a convergent solution is found. The interaction is notionally taken into account by the evolution of the background medium that contains information about the inclusions, albeit in a homogenous form. As the inclusion can have an

ellipsoidal shape an additional microstructural parameter is taken into account by this type of model.

Several scientists (e.g., Bruner, 1976) have remarked that the SC progressively overestimates the interaction with increasing concentration. They proposed an alternative differential effective medium (DEM) method in which the inclusion concentration is increased in small steps with a re-evaluation of the elastic constants of the aggregate at each increment. This scheme allows the potential energy of the medium to vary slowly with inclusion concentration (Bruner, 1976). Since the addition of inclusions to the backgound material is made in very small increments, one can consider the concentration step to be very dilute with respect to the current effective medium. It follows that the effective interaction between inclusions can be considered negligible and we can use the inclusion theory of Eshelby (1957) to take into account the interaction. In contrast, the SC uses Eshelby's theory plus an iterative evaluation of the background medium to take into account the interaction. Mainprice (1997) has compared the results of SC and DEM for anisotropic oceanic crustal and mantle rocks containing melt inclusions and found the results to be very similar for melt fractions of less than 30%. At higher melt fractions the SC exhibits a threshold value around 60% melt, whereas the DEM varies smoothly up a 100% melt. The presence of a threshold in the SC calculations is due to the specific way that the interaction is taken into account. The estimates of both methods are likely to give relatively poor results at high fractions of a phase with strong elastic contrast with the other constituents as other phenomena, such as mechanical localization related to the percolation threshold, are likely to occur.

The third set of methods uses higher-order statistical correlation functions to take into account the first- or higher-order neighbor relations of the various microstructural elements. The factors that need to be statistically described are the elastic constants (determined by composition), orientation, and relative position of an element. If the element is considered to be small relative to grain size, then grain shape and the heterogeneity can be accounted for the relative position correlation function. Nearest neighbors can be taken into account using a two-point correlation function, which is also called an autocorrelation function by some authors. If we use the 'statistically uniform' sample introduced above, we are effectively assuming that all the correlation functions used to describe the microstructure up to order infinity are statistically isotropic; this is clearly a very strong assumption. In the special case where all the correlation functions up to order infinity are defined, Kröner (1978) has shown that the upper and lower bounds converge for the self-consistent method so that $C^{sc} = (S^{sc})^{-1}$. The statistical continuum approach is the most complete description and has been extensively used for model calculations (e.g., Beran *et al.*, 1996; Mason and Adams, 1999). Until recently, it has been considered too involved for practical application. With the advent of automated determination of crystal orientation and positional mapping using electron back-scattered diffraction (EBSD) in the scanning electron microscope (Adams *et al.*, 1993), digital microstructural maps are now available for the determination of statistical correlation functions. This approach provides the best possible estimate of the elastic properties but at the expense of considerably increased computational complexity.

The fact that there is a wide separation in the Voigt and Reuss bounds for anisotropic materials is caused by the fact that the microstructure is not fully described by such methods. However, despite the fact that these methods do not take into account such basic information as the position or the shape of the grains, several studies have shown that the Voigt or the Hill average are within 5–10% of experimental values for low porosity rocks free of fluids. For example, Barruol and Kern (1996) showed for several anisotropic lower crust and upper mantle rocks from the Ivrea zone in Italy that the Voigt average is within 5% of the experimentally measured velocity.

## 2.5 Seismic Properties of Polycrystalline Aggregates at High Pressure and Temperature

Orientation of crystals in a polycrystal can be measured by volume diffraction techniques (e.g., X-ray or neutron diffraction) or individual orientation measurements (e.g., U-stage and optical microscope, electron channelling or EBSD). In addition, numerical simulations of polycrystalline plasticity also produce populations of crystal orientations at mantle conditions (e.g., Tommasi *et al.*, 2004). An orientation, often given the letter **g**, of a grain or crystal in sample coordinates can be described by the rotation matrix between crystal and sample coordinates. In practice, it is convenient to describe the rotation by a triplet of Euler angles, for example, $\mathbf{g} = (\varphi 1\ \phi\ \varphi 2)$ used by Bunge (1982). One should be aware that there are

many different definitions of Euler angles that are used in the physical sciences. The orientation distribution function (ODF) $f(\mathbf{g})$ is defined as the volume fraction of orientations with an orientation in the interval between $\mathbf{g}$ and $\mathbf{g}+\mathrm{d}\mathbf{g}$ in a space containing all possible orientations given by

$$\Delta V/V = \int f(\mathbf{g})\,\mathrm{d}\mathbf{g}$$

where $\Delta V/V$ is the volume fraction of crystals with orientation $\mathbf{g}$, $f(\mathbf{g})$ is the texture function, and $\mathrm{d}\mathbf{g} = 1/8\pi^2 \sin\phi\ \mathrm{d}\varphi 1\ \mathrm{d}\phi\ \mathrm{d}\varphi 2$ is the volume of the region of integration in orientation space.

To calculate the seismic properties of a polycrystal, one must evaluate the elastic properties of the aggregate. In the case of an aggregate with a crystallographic fabric, the anisotropy of the elastic properties of the single crystal must be taken into account. For each orientation $\mathbf{g}$ the single-crystal properties have to be rotated into the specimen coordinate frame using the orientation or rotation matrix $g_{ij}$,

$$C_{ijkl}(\mathbf{g}) = g_{ip}\cdot g_{jq}\cdot g_{kr}\cdot g_{ls}\,C_{pqrs}(\mathbf{g}^{\circ})$$

where $C_{ijkl}(\mathbf{g})$ is the elastic property in sample coordinates, $g_{ij} = g(\varphi 1\ \phi\ \varphi 2)$ the measured orientation in sample coordinates, and $C_{pqrs}(\mathbf{g}^{\circ})$ is the elastic property in crystal coordinates.

The elastic properties of the polycrystal may be calculated by integration over all possible orientations of the ODF. Bunge (1982) has shown that integration is given as

$$<C_{ijkl}>^{m} = \int C_{ijkl}{}^{m}(\mathbf{g})\cdot f(\mathbf{g})\,\mathrm{d}g$$

where $<C_{\mathrm{ijkl}}>^{m}$ is the elastic properties of the aggregate of mineral $m$. Alternatively, it may be determined by simple summation of individual orientation measurements:

$$<C_{ijkl}>^{m} = \sum C_{ijkl}{}^{m}(\mathbf{g})\cdot v(\mathbf{g})$$

where $v(\mathbf{g})$ is the volume fraction of the grain in orientation $\mathbf{g}$. For example, the Voigt average of the rock for $m$ mineral phases of volume fraction $v(m)$ is given as

$$<C_{ijkl}>^{\mathrm{Voigt}} = \sum v(m)\ <C_{ijkl}>^{m}$$

The final step is the calculation of the three seismic phase velocities by the solution of the Christoffel equation, details of which are given above.

To calculate the elastic constants at pressures and temperatures, the single-crystal elastic constants are given at the pressure and temperature of their measurement by using the following relationship:

$$\begin{aligned} C_{ij}(PT) = {} & C_{ij}(P_{\mathrm{o}}\,T_{\mathrm{o}}) + (\mathrm{d}C_{ij}/\mathrm{d}P)\cdot\Delta P \\ & + \frac{1}{2}(\mathrm{d}^2 C_{ij}/\mathrm{d}P^2)\cdot\Delta P^2 + (\mathrm{d}C_{ij}/\mathrm{d}T)\cdot\Delta T \\ & + (\mathrm{d}^2 C_{ij}/\mathrm{d}P\mathrm{d}T)\cdot\Delta P\cdot\Delta T \end{aligned}$$

where $C_{ij}(PT)$ are the elastic constants at pressure $P$ and temperature $T$, $C_{ij}(P_{\mathrm{o}}T_{\mathrm{o}})$ the elastic constants at a reference pressure $P_{\mathrm{o}}$ (e.g., 0.1 MPa) and temperature $T_{\mathrm{o}}$ (e.g., 25°C), $\mathrm{d}C_{ij}/\mathrm{d}P$ is the first-order pressure derivative, $\mathrm{d}C_{ij}/\mathrm{d}T$ is the first-order temperature derivative, $\Delta P = P - P_{\mathrm{o}}$ and $\Delta T = T - T_{\mathrm{o}}$. The equation is a Maclaurin expansion of the elastic tensor as a function of pressure and temperature, which is a special case of a Taylor expansion as the series is developed about the elastic constants at the reference condtion $C_{ij}(P_{\mathrm{o}}T_{\mathrm{o}})$. The series only represent the variation of the $C_{ij}$ in their intervals of pressure and temperature of convergence; in other words, the pressure and temperature range of the experiments or atomic modeling calculations used to determine the derivatives. Note this equation is not a polynomial and care has to taken when using the results of data fitted to polynomials, as for example the second-order derivatives fitted to a polynomial should be multiplied by 2 for use in the equation above, for example, second-order pressure derivatives for MgO given by Sinogeikin and Bass (2002). Also, note this equation is not a Eulerian finite strain equation of state (e.g., Davies, 1974, see below) and data fit to such an equation will not have derivatives compatible with the equation above, for example, the pressure derivatives of Brucite determined by Jiang *et al.* (2006). The second-order pressure derivatives $\mathrm{d}^2 C_{ij}/\mathrm{d}P^2$ are available for an increasing number of mantle minerals (e.g., olivine, orthopyroxene, garnet, MgO) and first-order temperature derivatives seem to adequately describe the temperature dependence of most minerals, although second-order derivatives are also available in a few cases (e.g., garnet, fayalite, fosterite, rutile; see Isaak (2001) for references). Experimental measurements of the cross pressure–temperature derivatives $\mathrm{d}^2 C_{ij}/\mathrm{d}P\mathrm{d}T$ (that is the temperature derivative of the $C_{ij}/\mathrm{d}P$ at constant temperature) are still very rare. For example, despite the fact that MgO (periclase) is a well-studied reference material for high-pressure studies, the complete set of single-crystal cross-derivatives were measured for the first

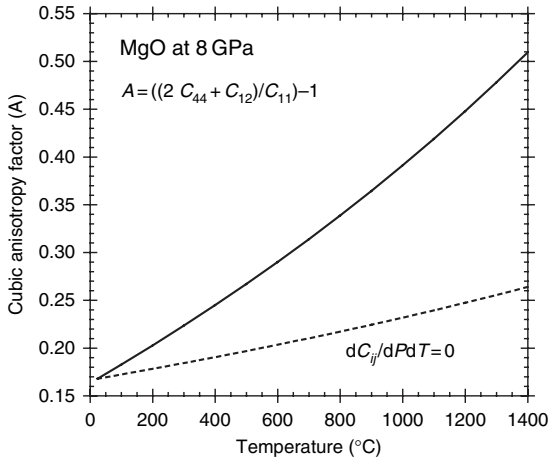


**Figure 11** An illustration of the importance of the cross pressure–temperature derivatives for cubic MgO at 8 GPa pressure. With increasing temperature at constant pressure, the anisotropy measured by the cubic anisotropy factor (*A*) increases by a factor of 2. Data from Chen *et al*. (1998).

time by Chen *et al.* (1998) to 8 GPa and 1600 K. The effect of the cross-derivatives on the $V_p$ and $dV_s$ anisotropy of MgO is dramatic; the anisotropy is increased by a factor of 2 when cross derivatives are used (**Figure 11**). Note when a phase transitions occurs, then the specific changes in elastic constants at pressures near the phase transition will have to be taken into account, for example, the $SiO_2$ polymorphs (Karki *et al.*, 1997b; Cordier *et al.*, 2004a; Carpenter, 2006). The seismic velocities also depend on the density of the minerals at pressure and temperature which can be calculated using an appropriate equation of state (Knittle, 1995). The Murnaghan equation of state derived from finite strain is sufficiently accurate at moderate compressions (Knittle, 1995) of the upper mantle and leads to the following expression for density as a function of pressure:

$$\rho(P) = \rho_o(1 + (K'/K)\cdot(P - P_o))^{1/K'}$$

where $K$ is bulk modulus, $K' = dK/dP$ the pressure derivative of $K$, $\rho_o$ is the density at reference pressure $P_o$ and temperature $T_o$. For temperature the density varies as

$$\rho(T) = \rho_o\left[1 - \int \alpha_v(T)dT\right] \approx \rho_o[1 - \alpha_{av}(T - T_o)]$$

where $\alpha_v(T) = (1/V)(\partial V/\partial T)$ is the volume thermal expansion coefficient as a function of temperature and $\alpha_{av}$ is an average value of thermal expansion which is constant over the temperature range (Fei, 1995). According to Watt (1988) an error of less 0.4% on the P- and S-velocity results from using $\alpha_{av}$ to 1100 K for MgO. For temperatures and pressures of the mantle, the density is described by

$$\rho(P, T) = \rho_o\left\{(1 + (K'/K)\cdot(P - P_o))^{1/K'}[1 - \alpha_{av}(T - T_o)]\right\}$$

An alternative approach for the extrapolation elastic constants to very high pressures is Eulerian finite strain theory (e.g., Davies, 1974). The theory is based on a Maclaurin expansion of the free energy in terms of Eulerian finite volumetric strain. For example, Karki *et al.* (2001) reformulated Davies's equations for the elastic constants in terms of finite volumetric strain ($f$) as

$$C_{ijkl}(f) = (1 + 2f)^{7/2} \times \left[C_{oijkl} + b_1 f + \frac{1}{2}b_2 f + \cdots\right] - P\Delta_{ijkl}$$

where

$$f = \frac{1}{2}\left[(V_o/V)^{2/3} - 1\right]$$

$$b_1 = 3K_o(dC_{oijkl}/dP) - 5C_{oijkl}$$

$$b_2 = 9K_o^2(d^2C_{oijkl}/dP^2) + 3(K_o/dP)(b_1 + 7C_{oijkl}) - 16b_1 - 49C_{oijkl}$$

$$\Delta_{ijkl} = -\delta_{ij}\delta_{kl} - \delta_{ik}\delta_{jl} - \delta_{il}\delta_{jk}$$

However, with advent of practical computational methods for applying first-principles (*ab initio*) methods to calculation of elastic constants of minerals at extreme pressures reduces the Eulerian finite strain theory to a descriptive tool, if tensors are available at the appropriate pressure (and temperature) conditions. The simple Maclaurin series expansions given above for pressure and temperature are a compact way of describing the variation of the elastic tenors in experimentations at high pressure and temperature. Extrapolation of the simple Maclaurin series expansions outside the range of experimental (or computational) data is not recommended, as the formulation is descriptive. The relative complexity of the Eulerian finite volumetric strain formulation has the merit of a physical basis and hence extrapolation beyond the experimental data range may be undertaken with caution. In practice, applications of the Eulerian finite volumetric strain formulation have been limited to high symmetry crystals (e.g., Li *et al.*, 2006b, cubic Ca-pervoskite, trigonal brucite;

Jiang *et al.*, 2006), a new thermodynamically correct formulation of the problem in terms of pressure and temperature has recently proposed by Stixrude and Lithgow-Bertelloni (2005a, 2005b).

## 2.6 Anisotropy Minerals in the Earth's Mantle and Core

To understand the anisotropic seismic behavior of polyphase rocks in the Earth's mantle, it is instructive to first consider the properties of the component single crystals. In this section emphasis is on the anisotropy of individual minerals rather than the magnitude of velocity. The percentage anisotropy ($A$) is defined here as $A = 200\ (V_{\text{maximum}} - V_{\text{minimum}})/(V_{\text{maximum}} + V_{\text{minimum}})$, where the maximum and minimum are found by exploring a hemisphere of all possible propagation directions. Note for P-wave velocities the anisotropy is defined by the maximum and minimum velocities in two different propagation directions, for example, the maximum $A$ is given by the maximum and minimum $V_p$ in a hemipshere, or for $V_p$ in two specific directions such as the vertical and horizontal can be used. For S-waves in an anisotropic medium there are two orthogonally polarized S-waves with different velocites for each propagation direction; hence, $A$ can be defined for each direction. The consideration of the single-crystal properties is particularly important for the transition zone (410–660 km) and lower mantle (below 660 km) as the deformation mechanisms and resulting preferred orientation of these minerals under the extreme conditions of temperature and pressure are very poorly documented by experimental investigations. In choosing the anisotropic single-crystal properties, where possible, the most recent experimental determinations have been included. A major trend in recent years is the use of computational modeling to determine the elastic constants at very high pressures and more recently at high temperatures. The theoretical modeling gives a first estimate of the pressure and temperature derivatives in a range not currently accessible to direct measurement (see review by Karki *et al.* (2001), also *see* Chapter 2.06). Although there is an increasing amount of single-crystal data available to high temperature or pressure, no data is available for simultaneous high temperature and pressure of the Earth's lower mantle or inner core (see **Figure 1** for the pressure and temperatures).

### 2.6.1 Upper mantle

The upper mantle (down to 410 km) is composed of three anisotropic and volumetrically important phases: olivine, enstatite (orthopyroxene), and diopside (clinopyroxene). The other volumetrically important phase is garnet, which is nearly isotropic and hence not of great significance to our discussion of anisotropy.

*Olivine.* A certain number of accurate determinations of the elastic constants of olivine are now available which all agree that the anisotropy of $V_p$ is 25% and maximum anistropy of $V_s$ is 18% at ambient conditions for a mantle composition of about Fo90. The first-order temperature derivatives have been determined between 295 and 1500 K for forsterite (Isaak *et al.*, 1989a) and olivine (Isaak, 1992). The first- and second-order pressure derivatives for olivine were first determined to 3 GPa by Webb (1989). However, a determination to 17 GPa by Zaug *et al.* (1993) and Abramson *et al.* (1997) has shown that the second-order derivative is only necessary for elastic stiffness modulus $C_{55}$. The first-order derivatives are in good agreement between these two studies. The second-order derivative for $C_{55}$ has proved to be controversial. Zaug *et al.* (1993) where first to measure nonlinear variation of $C_{55}$ with pressure, but other studies have not reproduced this behavior (e.g., for olivine: Chen *et al.*, 1996 and Zha *et al.*, 1998 or fosterite Zha *et al.*, 1996). The anisotropy of the olivine single crystal increases slightly with temperature ($+2\%$) using the data of Isaak (1992) and reduces slightly with increasing pressure using the data of Abramson *et al.* (1997).

*Orthopyroxene.* The elastic properties of orthopyroxene (Enstatite or Bronzite) with a magnesium number ($Mg/(Mg + Fe)$) near the typical upper mantle value of 0.9 has also been extensively studied. The $V_p$ anisotropy varies between 15.1% (En80 Bronzite; Frisillo and Barsch (1972)) and 12.0% (En100 Enstatite; Weidner *et al.* (1978)) and the maximum $V_s$ anisotropy between 15.1% (En80 Bronzite; Webb and Jackson, 1993), and 11.0% (En100 Enstatite; Weidner *et al.*, 1978). Some of the variation in the elastic constants and anisotropy may be related to composition and structure in the orthopyroxenes. The first-order temperature derivatives have been determined over a limited range between 298 and 623 K (Frisillo and Barsch, 1972). The first- and second-order pressure derivatives for Enstatite have been determined up to 12.5 GPa by Chai *et al.* (1997). This study confirms an earlier one of Webb and Jackson to 3 GPa that showed that first- and

second-order pressure derivatives are needed to describe the elastic constants at mantle pressures. The anisotropy of $V_p$ and $V_s$ does not vary significantly with pressure using the data of Chai *et al.* (1997) to 12.5 GPa. The anisotropy of $V_p$ and $V_s$ does increase by about 3% when extrapolating to 1000°C using the first-order temperature derivatives of Frisillo and Barsch (1972).

*Clinopyroxene.* The elastic constants of clinopyroxene (Diopside) of mantle composition have only been experimentally measured at ambient conditions (Levien *et al.*, 1979; Collins and Brown, 1998); both studies show that $V_p$ anisotropy is 29% and $V_s$ anisotropy is between 20% and 24%. There are no measured single-crystal pressure derivatives. In one of the first calculations of the elastic constants of a complex silicate at high pressure, Matsui and Busing (1984) predicted the first-order pressure derivatives of diopside from 0 to 5 GPa. The calculated elastic constants at ambient conditions are in good agreement with the experimental values and the predicted anisotropy for $V_p$ and $V_s$ of 35.4% and 21.0%, respectively, is also in reasonable agreement. The predicted bulk modulus of 105 GPa is close to the experimental value of 108 GPa given by Levien *et al.* (1979). The pressure derivative of the bulk modulus 6.2 is slightly lower than the value of $7.8 \pm 0.6$ given by Bass *et al.* (1981). Using the elastic constants of Matsui and Busing (1984), the $V_p$ anisotropy decreases from 35.4% to 27.7% and $V_s$ increases from 21.0% to 25.5% with increasing pressure from ambient to 5 GPa. In the absence of experimental measurements, the author would recommend using the values given by Matsui and Busing (1984). A major problem until recently was the lack of clinopyroxene temperature derivatives. Isaak *et al.* (2005) have mesured the temperature derivatives of chrome diopside to 1300 K at room pressure that are notably smaller than other mantle minerals. The single-crystal seismic properties of olivine, enstatite, and diopside at 220 km depth are illustrated in **Figure 12**. Garnet is nearly isotropic with $V_p$ anisotropy of 0.6% and $V_s$ of 1.3%. With an increasing interest in the water cycle in the deep Earth and subduction processes, the properties of hydrated phases are being studied. Although very little is currently known about the elastic properties of olivine containing water, the single-crystal elastic constants of the A-phase have

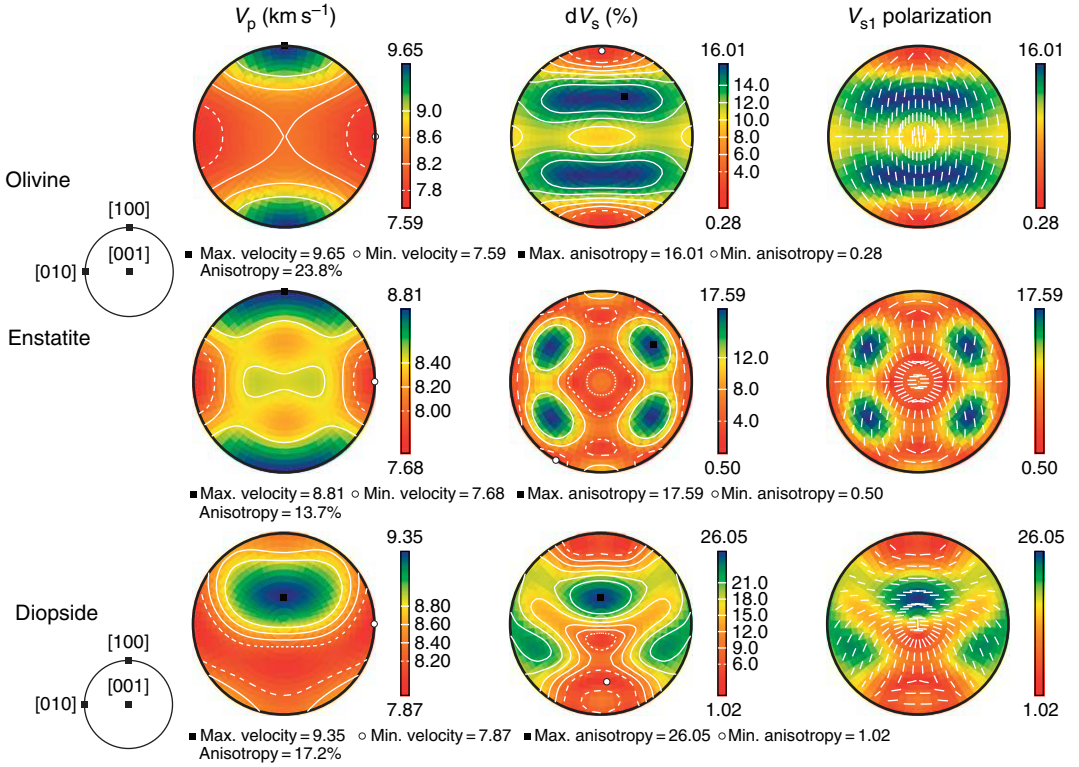


**Figure 12** Single-crystal anisotropic seismic properties of upper mantle minerals olivine (orthorhombic), enstatite (orthorhombic), and diopside (monoclinic) at about 220 km (7.1 GPa, 1250°C).

been determined at ambient conditions (Sanchez-Valle *et al.*, 2006). The A-phase is the only dense hydrous magnesium silicate occurring along the fosterite–humite join. The A-phase is hexagonal and can contain up 11.8 wt.% water and is about 8% less dense than olivine. The hydration of forsterite to phase A decreases the bulk and shear moduli by about 18% and 21%, respectively, while both compressional and shear wave velocities decrease by about 7%. These results suggest that water could be identified seismologically, if phase A is present in abundance in cold (below 1000°C at 15 GPa) subducted slabs. The A-phase is anisotropic with $V_p$ anisotropy of 11.6% and d$V_s$ of 15.8%. However, their actuel presence in the mantle is currently considered as speculative (see Jacobsen (2006)).

### 2.6.2 Transition zone

Over the last 20 years a major effort has been made to experimentally determine the phase petrology of the transition zone and lower mantle. Although single crystals of upper-mantle phases are readily available, single crystals of transition zone and lower mantle for elastic constant determination have to be grown at high pressure and high temperature. The petrology of the transition zone is dominated by garnet, majorite, wadsleyite, ringwoodite, calcium-rich perovskite, clinopyroxene, and possibly stishovite.

*Majorite.* The pure Mg end-member majorite of the majorite–pyrope garnet solid solution has tetragonal symmetry and is weakly anisotropic with 1.8% for $V_p$ and 9.1% for $V_s$ (Pacalo and Weidner, 1997). A study of the majorite–pyrope system by Heinemann *et al.* (1997) shows that tetragonal form of majorite is restricted to a composition of less 20% pyrope and hence is unlikely to exist in the Earth's transition zone. Majorite with cubic symmetry is nearly isotropic with $V_p$ anisotropy of 0.5% and $V_s$ of 1.1%. Pressure derivatives and temperature derivatives for majorite and majorite–pyrope have been determined by Sinogeikin and Bass (2002), respectively. Cubic majorite has very similar properties to pyrope garnet (Chai *et al.*, 1997) as might be expected. The elastic properties of sodium-rich Majorite have studied by Pacalo *et al.* (1992).

*Wadsleyite.* The elastic constants of $Mg_2SiO_4$ wadsleyite were first determined by Sawamoto *et al.* (1984) and this early determination was confirmed by Zha *et al.* (1987) with a $V_p$ anisotropy of 16% and $V_s$ of 17%. The $(Mg, Fe)_2SiO_4$ wadsleyite has slightly lower velocities and higher anisotropies (Sinogeikin *et al.*, 1998). The first-order pressure derivatives determined from the data of Zha *et al.* (1997) to 14 GPa show that the anisotropy of $Mg_2SiO_4$ wadsleyite decreases slightly with increasing pressure. At pressures corresponding to the 410 km seismic discontinuity (*c.* 13.8 GPa), the $V_p$ anisotropy would be 11.0% and $V_s$ 12.5%.

*Ringwoodite.* The elastic constants of $Mg_2SiO_4$ ringwoodite were first measured by Weidner *et al.* (1984) and $(Mg, Fe)_2SiO_4$ ringwoodite by Sinogeikin *et al.* (1998) at ambient conditions with $V_p$ anisotropy of 3.6% and 4.7%, and $V_s$ of 7.9% and 10.3%, respectively. Kiefer *et al.* (1997) have calculated the elastic constants of $Mg_2SiO_4$ ringwoodite to 30 GPa. Their constants at ambient conditions give a $V_p$ anisotropy of 2.3% and $V_s$ of 4.8% very similar to the experimental results of Weidner *et al.* (1984). There is a significant variation (5–0%) of the anisotropy of ringwoodite with pressure, 15 GPa (*c.* 500 km depth) the $V_p$ anisotropy is 0.4% and $V_s$ is 0.8%; hence, ringwoodite is nearly perfectly isotropic at transition zone pressures. Single-crystal temperature derivatives have been measured for ringwoodite (Jackson *et al.*, 2000), but none are available for wadsleyite. Olivine transforms to wadsleyite at about 410 km, and wadsleyite transforms to ringwoodite at about 500 km, both transformations result in a decrease in anisotropy with depth. The gradual transformation of clinopyroxene to majorite between 400 and 475 km would also result in a decrease in anisotropy with depth. The seismic anisotropy of wadsleyite and ringwoodite is illustrated in **Figure 13**. A recent *ab initio* molecular dynamics study by Li *et al.* (2006a) has shown that ringwoodite is nearly isotropic at transition zone conditions with P- and S-wave anisotropy close to 1%, extrapolated experimental values to a depth of 550 km (19.1 GPa, 1520°C) suggest that the $V_p$ and $V_s$ anisotropy are 3.3% and 8.2%. Both Ringwoodite and Wadsleyite have hydrous forms. Wadsleyite can contain up to 3.3 wt.% water, in fact perfectly anhydrous Wadsleyite is unknown. No single-crystal elastic constants are available for hydrous Wadsleyite. Ringwoodite can contain up to 2.5 wt.% water and the single-crystal elastic properties of pure Mg end member (Inoue *et al.*, 1998; Wang *et al.*, 2003) and Fo90 hydrous ringwoodite (Jacobsen *et al.*, 2004) have be measured at ambiante conditions. The pressure derivatives for Fo90 hydrous ringwoodite have recently been determined to 9 GPa (Jacobsen and Smyth, 2006). Hydrous ringwoodite has the same anisotropy as the anhydrous mineral at ambient pressure. Both forms have an anisotropy that decreases with pressure, the hydrous from would become

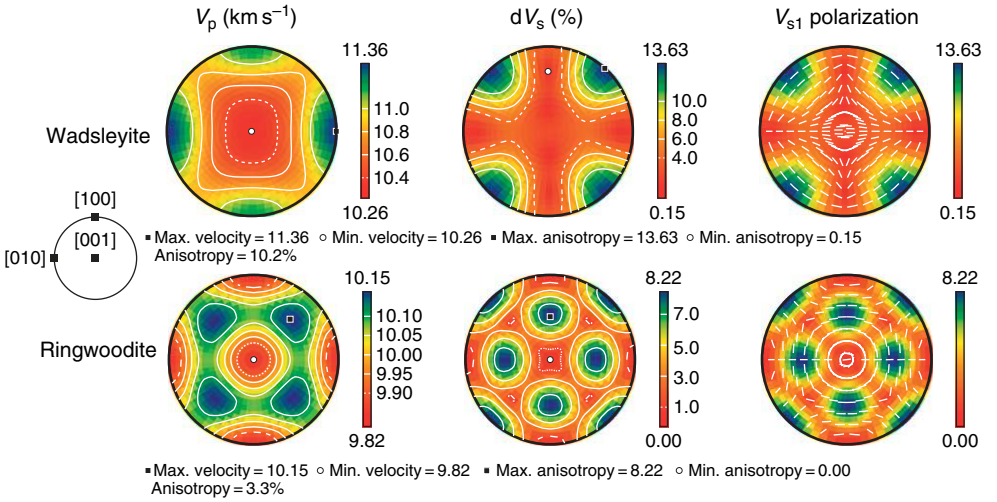


**Figure 13** Single-crystal anisotropic seismic properties of transition zone minerals wadsleyite (orthorhombic) at about 450 km (15.2 GPa, 1450°C) and ringwoodite (cubic) at about 550 km (19.1 GPa, 1520°C).

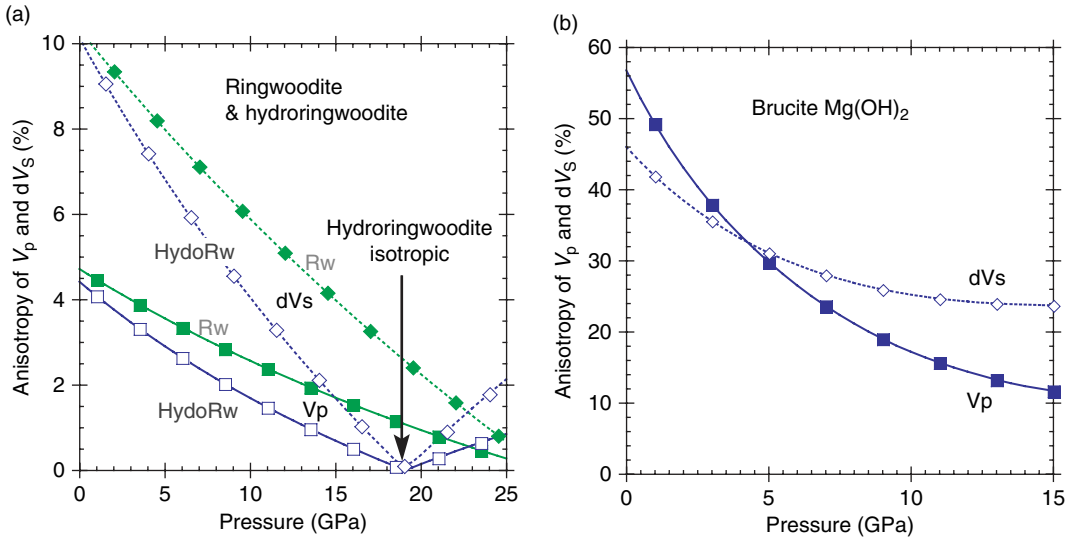


**Figure 14** The variation of seismic P and S anisotropy with increasing pressure for hydrous minerals. Note the decrease in anisotropy with increasing pressure. (a) Ringwoodite (cubic) and hydrous ringwoodite (cubic)). (see text for details). (b) Brucite (trigonal). (a) Data from Jacobsen SD and Smyth JR (2006) Effect of water on the sound velocities of ringwoodite in the transition zone. In: Jacobsen SD and van der Lee S (eds.) *Geophysical Monograph Series, 168: Earth's Deep Water Cycle*, pp. 131–145. Washington, DC: American Geophysical Union. (b) Data from Jiang F, Speziale S and Duffy TS (2006) Single-crystal elasticity of brucite, $Mg(OH)_2$, to 15 GPa by Brillouin scattering. *American Mineralogist* 91: 1893–1900.

isotropic at about 17 GPa (**Figure 14**(**a**)). Comparison with Brucite $Mg(OH)_2$ is interesting as it is a model system for understanding dense hydrous magniesium minerals (alphabet phases) under hydrostatic compression and an important structural unit of many layer silicates, such as chlorite, lizardite and talc. The single-crystal elastic constants of Brucite have recently been measured to a pressure of 15 GPa by Jiang *et al.* (2006). The seismic anisotropy of brucite is exceptionally high at ambient conditions with P- and S-wave anisotropy of 57% and 46%, respectively. As in hydrous ringwoodite both forms of anisotropy decrease with increasing pressure being 12% and 24% at 15 GPa for P- and S-wave anisotropy of 57% and 46%, respectively (**Figure 14**(**b**)). The stronger decrease of P-wave anisotropy compared to S-wave is probably related to the very important linear compressibility along the *c*-axis. The apparent symmetry of the

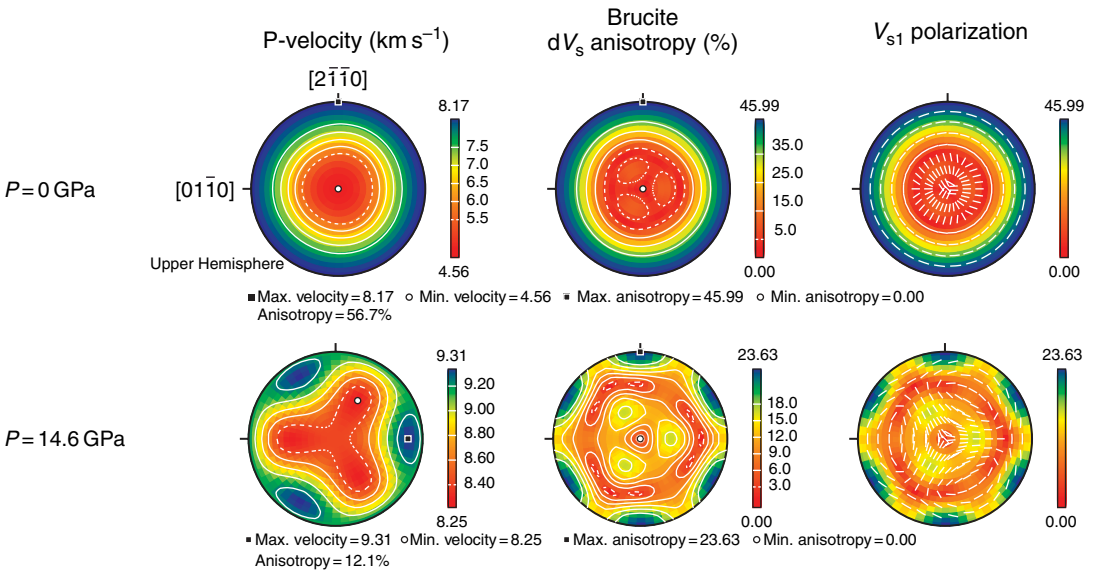


**Figure 15** Single-crystal anisotropic seismic properties of brucite (trigonal) at 0 and 14.6 GPa, data from Jiang *et al*. (2006). Note the change in velocity distribution of P-waves, d$V_s$ anisotropy and S1 polarization orientations, which reflect the nearly hexagonal symmetry of Brucite's elastic properties at low pressure and the increasingly trigonal nature (threefold *c*-axis at the center of the pole figure) with increasing pressure.

seismic anisotropy of brucite changes with pressure (**Figure 15**). Brucite is stable to 80 GPa and modest temperatures, so it could be an anisotropic component of cold subducted slabs.

### 2.6.3 Lower mantle

The lower mantle is essentially composed of perovskite, ferripericlase, and possibly minor amount of $SiO_2$ in the form of stishovite in the top part of the lower mantle (e.g., Ringwood, 1991). Ferripericlase is the correct name for (Mg, Fe),O with small percentage of iron, less than 50% in Mg site; previously this mineral was incorrectly called magnesiowustite, which should have more than 50% Fe. It is commonly assumed that there is about 20% Fe in ferripericlase in the lower mantle. $MgSiO_3$ may be in the form of perovskite or possibly ilmenite. The ilmenite structured $MgSiO_3$ is most likely to occur at the bottom of the transition zone and top of the lower mantle. In addition, perovskite transforms to postperovskite in the D″ layer, although extact distribution with depth (or pressure) of the phases will depend on the local temperature and their iron content.

*Perovskite ($MgSiO_3$, $CaSiO_3$).* The first determination of the elastic constants of pure $MgSiO_3$ perovskite at ambient conditions was given by Yeganeh-Haeri *et al.* (1989). However this determination has been replaced by a more accurate study of a better quality crystal (Yeganeh-Haeri, 1994). The 1994 study gives $V_p$ anisotropy of 13.7% and $V_s$ of 33.0%. The [010] direction has the maximum d$V_s$ anisotropy. A new measurement of the elastic constants of $MgSiO_3$ perovskite at ambient conditions was made by Sinogeikin *et al.* (2004), gives $V_p$ anisotropy of 7.6% and d$V_s$ of 15.4%, which has very similar velocity distribution to the determination of Yeganeh-Haeri (1994), but the anisotropy is reduced by a factor of 2. Karki *et al.* (1997a) calculated the elastic constants of $MgSiO_3$ perovskite 140 GPa at 0 K. The calculated constants are in close agreement with the experimental measurements of Yeganeh-Haeri (1994) and Sinogeikin *et al.* (2004). Karki *et al.* (1997a) found that significant variations in anisotropy occurred with increasing pressure, first decreasing to 6% at 20 GPa for $V_p$ and to 8% at 40 GPa for $V_s$ and then increasing to 12% and 16%, respectively, at 140 GPa. At the 660 km seismic discontinuity (*c.* 23 GPa) the $V_p$ and $V_s$ anisotropy would be 6.5% and 12.5%, respectively. Recent progress in finite temperature first-principles methods for elastic constants has allowed their calculation at lower mantle pressures and temperatures. Oganov *et al.* (2001) calculated the elastic constants of Mg-perovskite at two pressures and three temperatures for the lower mantle (**Figure 16**). More recently, Wentzcovitch *et al.* (2004) have calculated the elastic constants over the complete range of lower mantle conditions and produced pressure and temperature derivatives.

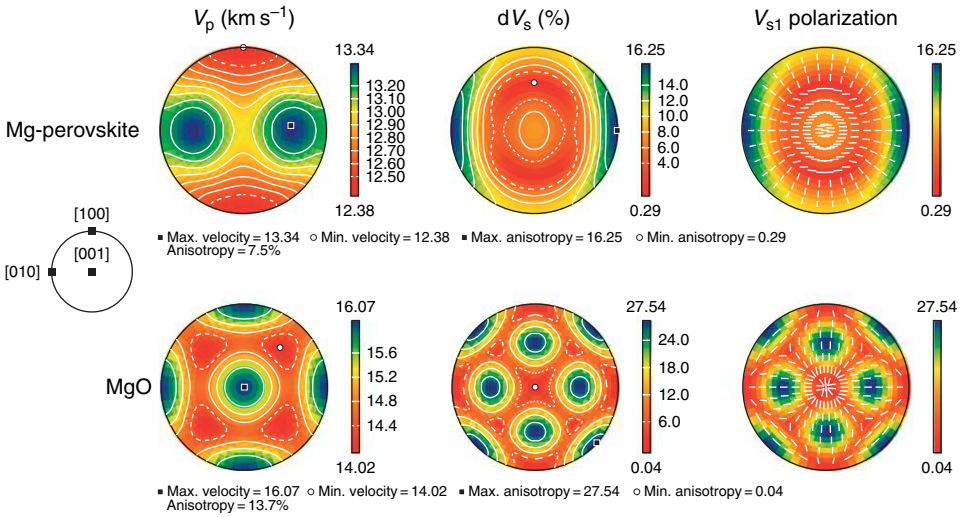


**Figure 16** Single-crystal anisotropic seismic properties of lower mantle minerals Mg-perovskite (orthorhombic) and MgO (periclase – cubic) at about 2000 km (88 GPa, 3227°C) using the elastic constants determined at high PT by Oganov *et al*. (2001) and Karki *et al* (2000) respectively.

The results for pure Mg-perovskite from Oganov *et al.* and Wentzcovitch *et al.* agree quite closely for P-wave anisotropy, but Oganov's elastic constants give a higher S-wave anisotropy. At ambient conditions the results from all studies are very similar with $V_p$ anisotropy is 13.7% and the $V_s$ anisotropy is 33.0%. When extrapolated along a geotherm using the pressure and temperature derivatives of Wentzcovitch *et al.* (2004) the P- and S-wave anisotropies about the same at 8% at 1000 km depth and again similar anisotropies of 13% at 2500 km depth. The other perovskite structure present in the lower mantle is $CaSiO_3$ perovskite, recent *ab initio* molecular dynamics study by Li *et al.* (2006b) has shown that this mineral is nearly isotropic at lower mantle conditions with P- and S-wave anisotropy close to 1%.

*$MgSiO_3$ ilmenite.* Experimental measurements by Weidner and Ito (1985) have shown that $MgSiO_3$ ilmenite of trigonal symmetry is very anisotropic at ambient conditions with $V_p$ anisotropy of 21.1% and $V_s$ of 36.4%. Pressure derivatives to 30 GPa have been obtained by first-principles calculation (Da Silva *et al.*, 1999) and the anisotropy decreases with increasing pressure to 9.9% for P-waves and 24.8% for S-waves at 30 GPa.

*Ferripericlase.* The other major phase is ferripericlase (Mg, Fe)O, for which the elastic constants have been determined. The elastic constants of the pure end-member periclase MgO of the MgO–FeO solid solution series has been measured to 3 GPa by Jackson and Niesler (1982). Isaak *et al.* (1989a, 1989b) have measured the temperature derivatives for MgO to 1800 K. Both these studies indicate a $V_p$ anisotropy of 11.0% and $V_s$ of 21.5% at ambient conditions. Karki *et al.* (1997c) calculated the elastic constants of MgO to 150 GPa at 0 K. The thermoelasticty of MgO at lower mantle temperatures and pressures has been studied by Isaak *et al.* (1990), Karki *et al.* (1999, 2000) (**Figure 16**), and more recently by Sinogeikin *et al.* (2004, 2005); there is good agreement between these studies for the elastic constants and pressure and temperature derivatives. However, the theoretical studies do not agree with experimentally measured cross pressure–temperature derivatives of Chen *et al.* (1998). At the present time only the theoretical studies permit the exploration of the seimic properties of MgO at lower mantle conditions. They find considerable changes in anisotropy is preserved at high temperature with increasing pressure, along a typical mantle geotherm, MgO is isotropic near the 670 km discontinuity, but the anisotropy of P- and S-waves increases rapidly with depth reaching 17% for $V_p$ and 36% for $V_s$ at the D″ layer. The anisotropy of MgO increases linearly from 11.0% and 21.5% for $V_p$ and $V_s$, respectively, at ambient conditions to 20% and 42%, respectively, at 1800 K according to the data of Isaak *et al.* (1989b). The effect of temperature on anisotropy is more important a low pressure than at lower mantle pressures, where the effect of pressure dominates according to the results of Karki *et al.* (1999). Furthermore, not only the magnitude of the anisotropy of MgO, but also the

orientation of the anisotropy changes with increasing pressure according to the calculations of Karki *et al.* (1999), for example, the fastest $V_p$ is parallel to [111] at ambient pressure and becomes parallel to [100] at 150 GPa pressure and fastest S-wave propagating in the [110] direction has a polarization parallel to [001] at low pressure that changes to [1–10] at high pressure. Ferripericlase–magnesiowustite solid solution series has been studied at ambient conditions by Jacobsen *et al.* (2002), for ferripericlase with 24% Fe the P-wave anisotropy is 10.5% and maximum S-wave is 23.7%, slightly higher than pure MgO at the same conditions. Data are required at lower mantle pressures to evaluate if the presence of iron has a significant effect on anisotropy of ferripericlase of mantle composition.

*$SiO_2$ polymorphs.* – The free $SiO_2$ in the transition zone and the top of the lower mantle (to a depth of 1180 km or 47 GPa) will be in the form of stishovite. The original experimental determination of the single-crystal elastic constants of stishovite by Weidner *et al.* (1982) and the more recent calculated constants of Karki *et al.* (1997b) both indicate a $V_p$ and $V_s$ anisotropy at ambient conditions of 26.7–23.0% and 35.8–34.4%, respectively, making this a highly anisotropic phase. The calculations of Karki *et al.* (1997a) show that the anisotropy increases dramatically as the phase transition to $CaCl_2$ structured $SiO_2$ is approached at 47 GPa. The $V_p$ anisotropy increases from 23.0% to 28.9% and $V_s$ from 34.4% to 161.0% with increasing pressure from ambient to 47 GPa. The maximum $V_p$ is parallel to [001] and the minimum parallel to [100]. The maximum $dV_s$ is parallel to [110] and the minimum parallel to [001].

*Postperovskite.* Finally, this new phase is present in the D″ layer. Discovered and published in May 2004 by Murakami *et al.* (2004), the elastic constants at 0 K were rapidly established at low (0 GPa) and high (120 GPa) pressure by static atomistic calculations (Iitaka *et al.*, 2004; Oganov and Ono, 2004; Tsuchiya *et al.*, 2004). From these first results we can see that Mg-postperovskite is very different to Mg-perovskite as there are substantial changes in the distribution of the velocity anisotropy with increasing pressure (**Figure 17**). At zero pressure the anisotropy is very high, 28% and 47% for

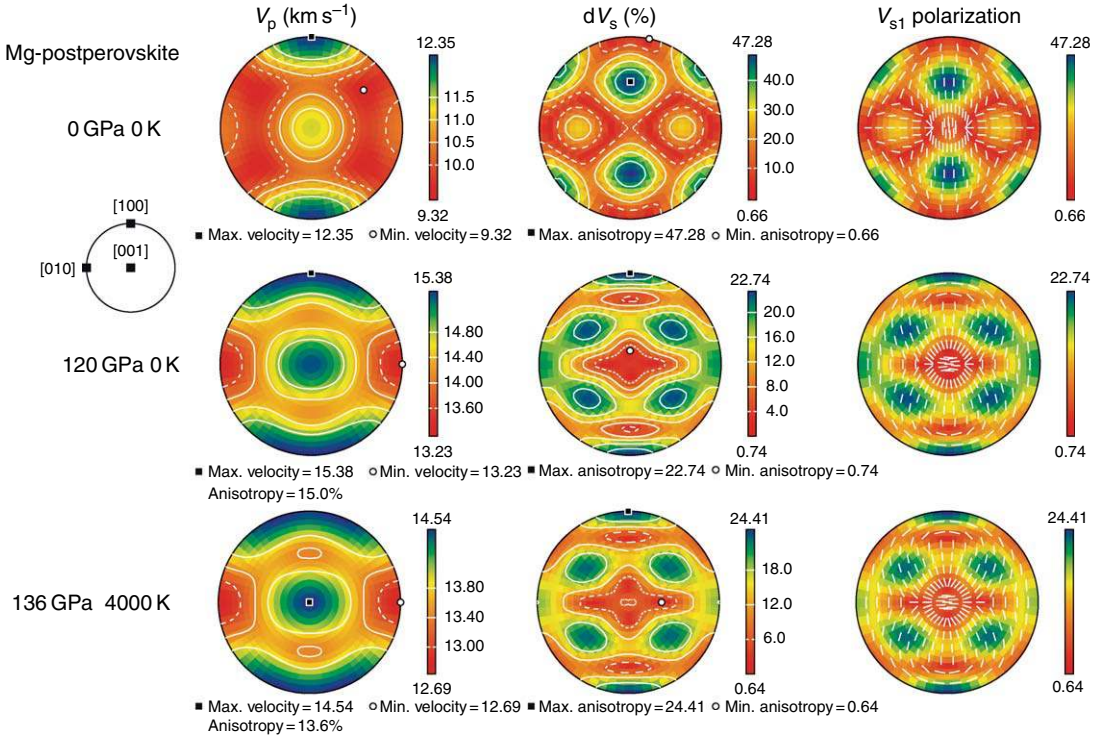


**Figure 17** Single-crystal anisotropic seismic properties of the D″ layer mineral Mg-postperovskite (orthorhombic). Increasing the pressure from 0 to 120 GPa at a temperature of 0 K decreases the anisotropy and also changes the distribution the maximum velocities and S-wave polarizations. Elastic constants calculated by Tsuchiya *et al*. (2004). Increasing the pressure to 136 GPa and temperature to 4000 K, there are relatively minor changes in the anisotropy. Elastic constants calculated by Stackhouse *et al*. (2005).

P- and S-waves, respectively. The maximum for $V_p$ is parallel to [100] with small submaxima parallel to [001] and minimum near [111]. The shear wave splitting ($dV_s$) has maxima parallel to <101> and <110>. At 120 GPa the anisotropy has reduced to 15% and 22% for P- and S-waves, respectively. The distribution of velocities has changed, with the P maximum still parallel to [100] and submaximum parallel to [001] which is now almost the same velocity as parallel to [100], the minimum is now parallel to [010]. The S-wave splitting maxima have also changed and are now parallel to <111>. Apparently, the compression of the postperovskite stucture has caused important elastic changes as in MgO. An *ab initio* molecular dynamics study by Stackhouse *et al.* (2005) at high temperature revealed that the velocity distribution and anisotropy were little affected by inceasing the temperature from 0 to 4000 K when at a pressure of 136 GPa (**Figure 17**). Wentzcovitch *et al.* (2006) produced a more extensive set of high-pressure elastic constants and pressure and temperature derivatives, similar P distributions and slightly different shear wave splitting pattern with maximum along the [001] axis which is not present in the Stackhouse *et al.* velocity surfaces or in high pressure 0 K results.

In conclusion for the mantle, we can say that the general trend favors an anisotropy decrease with increasing pressure and increase with increasing temperature; olivine is a good example of this behavior for minerals in upper mantle and transition zone. The changes are limited to a few percent in most cases. The primary causes of the anisotropy changes are minor crystal structural rearrangements rather than velocity changes due to density change caused by compressibility with pressure or thermal expansion with temperature. The effect of temperature is almost perfectly linear in many cases; some minor nonlinear effects are seen in diopside, MgO, and $SiO_2$ polymorphs. Nonlinear effects with increasing pressure on the elastic constants cause the anisotropy of wadsleyite, ringwoodite to first decrease. In the case of the lower mantle minerals Mg-perovskite and MgO, there is a steady increase in the anisotropy in increasing depth; this is a very marked effect for MgO. Stishovite also shows major changes in anisotropy in the pressure range close to the transformation to the $CaCl_2$ structure. The single-crystal temperature derivatives of wadsleyite, ilmenite $MgSiO_3$, and stishovite are currently unknown which make quantitative seismic anisotropic modeling of the transition zone and upper part of the lower-mantle speculative. To illustrate the variation of anisotropy as a function of mantle conditions of temperature and pressure, the seismic properties along a mantle geotherm (**Figure 18**) were calculated. The mantle geotherm is based on the PREM model for the pressure scale. The temperature scale is based on the continental geotherm of Mercier (1980) from the surface to 130 km and Ito and Katsura (1989) for the transition zone and Brown and Shankland (1981) for the lower mantle. The upper-mantle minerals olivine ($V_p$, $V_s$) and enstatite ($V_p$) show a slight increase of anisotropy in the first 100 km due to the effect of temperature. With increasing depth, the trend is for decreasing anisotropy except for $V_s$ of enstatite and diopside. In the transition zone and lower mantle, the situation is more complex due to the presence of phase transitions. In the transition zone diopside may be present to about 500 km with an increasing $V_s$ and decreasing $V_p$ anisotropy with depth. Wadsleyite is less anisotropic than olivine at 410 km, but significantly more anisotropic than ringwoodite found below 520 km. Although the lower mantle is known to be seismically isotropic, the constituent minerals are anisotropic. MgO shows important increase in anisotropy with depth (10–30%), at 670 km it is isotropic and 2800 km it is very anisotropic, possibly being candidate mineral to explain anisotropy of the D″ layer. Mg-perovskite is strongly anisotropic (*c.* 10%) throughout the lower mantle. The $SiO_2$ polymorphs are all strongly anisotropic, particularly for S-waves. If free silica is present in the transition zone or lower mantle, due perhaps to the presence of subducted basalt (e.g., Ringwood, 1991), then even a small volume fraction of the $SiO_2$ polymorphs could influence the seismic anisotropy of the mantle. However, to do so, the $SiO_2$ polymorphs would have to be oriented, either due to dislocation glide (plastic flow), oriented grain growth, or anisometric crystal shape (viscous flow) (e.g., Mainprice and Nicolas, 1989). Given that the $SiO_2$ polymorphs are likely to be 10% less by volume (Ringwood, 1991) and hence would not be the load-bearing framework of the rock, it is more likely that the inequant shape of $SiO_2$ polymorphs would control their orientation during viscous flow.

### 2.6.4 Inner core

Unlike the mantle the Earth's inner core is composed primarily of iron, with about 5 wt.% nickel and very small amounts of other siderophile elements such as

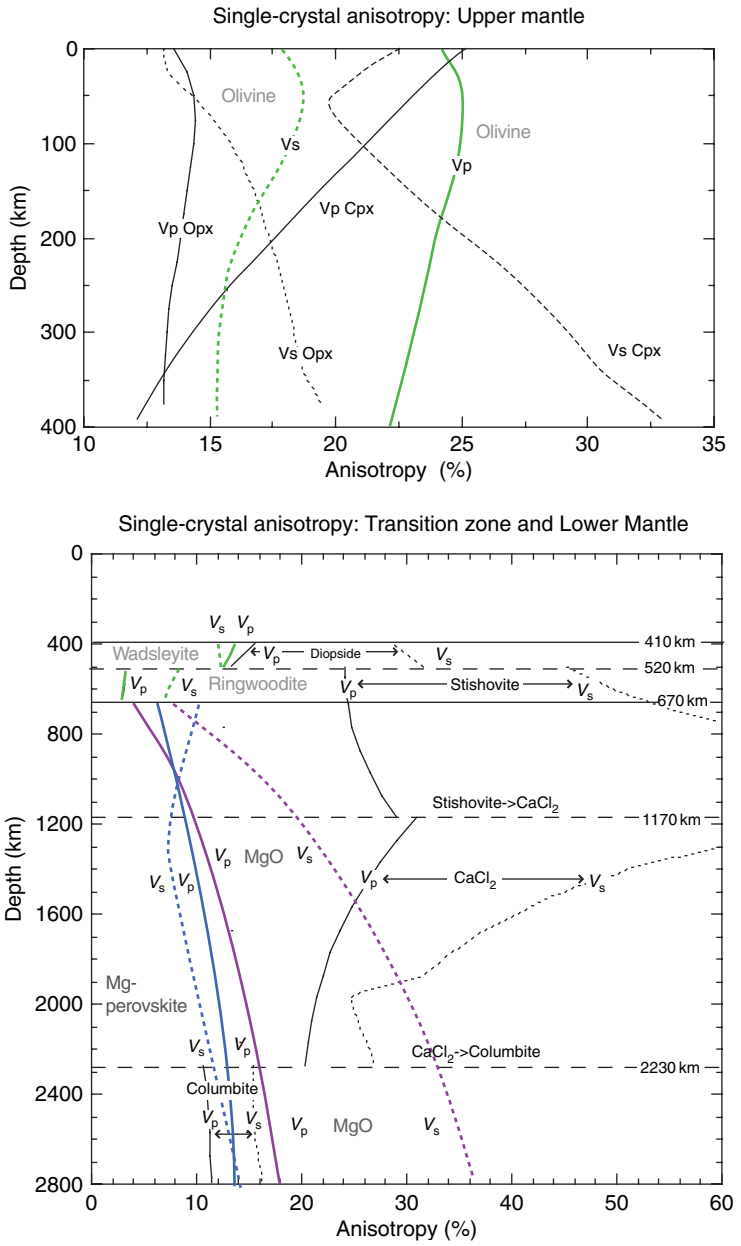


**Figure 18** Variation of single-crystal seismic anisotropy with depth. The phases with important volume fractions (see **Figure 1**) (olivine, wadsleyite, ringwoodite, Mg-perovskite, and MgO) are highlighted by a thicker line. P-wave anisotropy is the full line and the S-wave is the dashed line (see text fro details).

chromium, manganese, phosphorus, cobalt, and some light elements such as are oxygen, sulfur, and silicon. The stable structure of iron at ambient conditions is body-centered cubic (b.c.c.). When the pressure is increased above 15 GPa iron transforms to an h.c.p. structure called the $\varepsilon$-phase. At high pressure and temperature iron most likely remains h.c.p. However, there have been experimental observations of a double hexagonal close-packed structure (d.h.c.p.) (Saxena *et al.*, 1996) and a distorted h.c.p. structure with orthorhombic symmetry (Andrault *et al.*, 1997). Atomic modeling at high pressure and high temperature suggests that the h.c.p. structure is still stable at temperatures above 3500 K in pure iron (Vočadlo *et al.*, 2003a), although the energy differences between the h.c.p. and b.c.c. structures is very

small and the authors speculate that the b.c.c. structure may be stabilized by the presence of light elements. A suggestion echoed by the seismic study of Beghein and Trampert (2003). To make a quantitative anisotropic seismic model to compare with observations, one needs either velocity measurements or the elastic constants of single-crystal h.c.p. iron at the conditions of the inner core. The measurement or first-principles calculation of the elastic constants of iron is major challenge for mineral physics. The conditions of the inner core are extreme with pressures from 325 to 360 GPa, and temperatures from 5300 to 5500 K. To date experimental measurements have been using diamond anvil cells to achieve the high pressures on polycrystalline h.c.p. iron. Inelastic X-ray scattering has been used to measure $V_p$ at room temperature and high pressure up to 110 GPa at 298 K (Fiquet *et al.*, 2001), up to 153 GPa (Mao *et al.*, 2001) and the anisotropy of $V_p$ has been characterized in two directions up to 112 GPa (Antonangeli *et al.*, 2004). $V_p$ has been determined at simultaneous high pressure and temperature up to 300 GPa and up to 1200 K from X-ray Debye–Waller temperature factors (Dubrovinsky *et al.*, 2001) and up to 73 GPa and 1700 K using inelastic X-ray scattering by Lin *et al.* (2005). Radial X-ray diffraction has been used to measure the elastic constants of polycrystalline iron with simultaneous measurement of the CPO at room temperature and pressures up to 211 GPa (Singh *et al.*, 1998; Mao *et al.*, 1998 (with corrections, 1999); Merkel *et al.*, 2005), which is still well below inner-core pressures. The experimental results are plotted in **Figure 19** as $V_p$, $V_{SH}$, and $V_{SV}$ of a hexagonal media. Note that the polycrystals have a strong uniaxial (fiber) CPO with high concentration of *c*-axes parallel to compression direction of the diamond anvil cell as the symmetry axis and hence has hexagonal elastic symmetry like the single crystal.

In order to simulate the *in situ* conditions the static (0 K), elastic constants have been calculated at inner-core pressures (Stixrude and Cohen, 1995). The calculated elastic constants predict maximum P-wave maximum velocity parallel to the *c*-axis and the difference in velocity between the *c*- and *a*-axes is quite small (**Figure 20**). The anisotropy of the calculated elastic constants being quite low required that the crystal-preferred orientation is very strong; it was even suggested that inner core could be a single crystal of h.c.p. iron to be compatible with the seismic observations, and that *c*-axis is aligned with Earth's rotation axis. Other studies with calculations in static conditions include Steinle-Neumann *et al.* (2001) and Vočadlo *et al.* (2003b), which indicated a higher anisotropy for P-waves than Stixrude and Cohen (1995), but with same P-wave distribution with a maximum parallel to the *c*-axis. The first attempt to introduce temperature into first-principles methods for iron by Laio *et al.* (2000) produced estimates of the isotropic bulk and shear modulus at inner-core conditions (325 GPa and 5400 K) and single-crystal elastic constants at conditions comparable with the

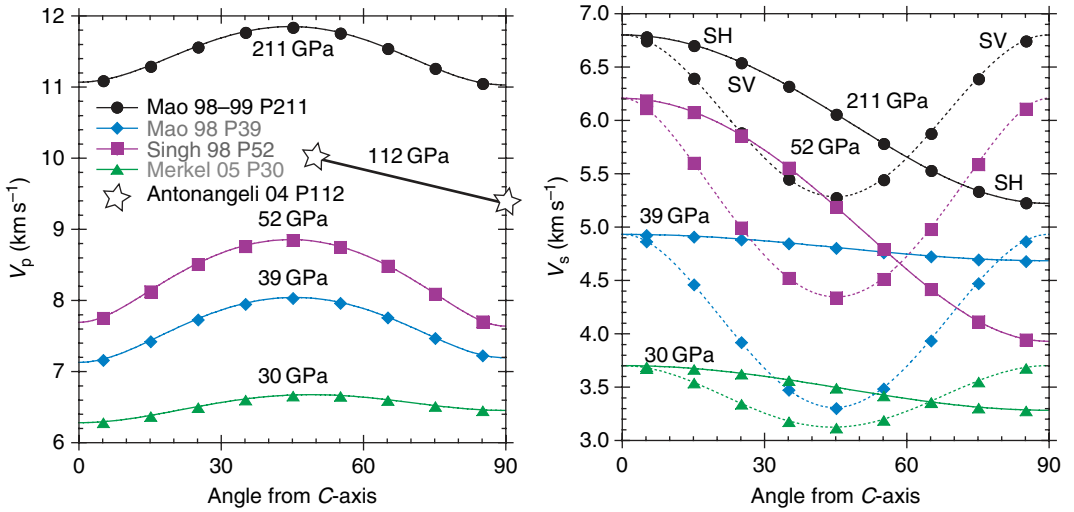


**Figure 19** The seismic velocities at ambient temperature in single-crystal hexagonal $\varepsilon$-phase iron calculated from the experimentally determined elastic constants or measured velocity in the case of Antonangeli *et al*. (2004) (see text for discussion).

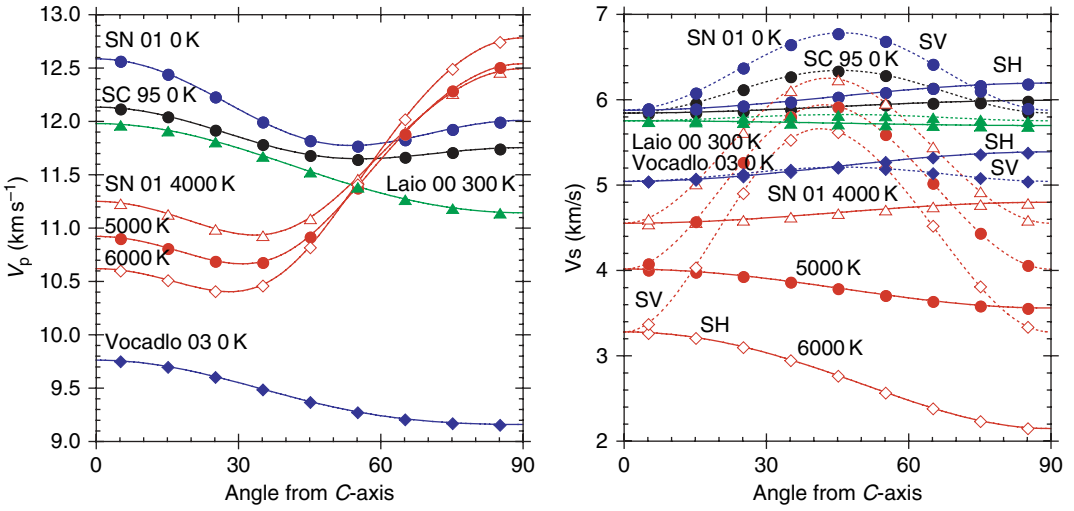


**Figure 20** The seismic velocities at 0 K or high temperature in single-crystal hexagonal e-phase iron calculated from the theoretically determined elastic constants (see text for discussion).

experimental study of Mao *et al.* (1998) (210 GPa and 300 K). The first study of simulate inner core temperatures (up to 6000 K) and pressures by Steinle-Neumann *et al.* (2001) produced two unexpected results, first the increase of the unit cell axial *c*/*a* ratios by a large amount (10%) with increasing temperature, and second the migration of the P-wave maximum velocity to the basal plane at high temperature. These new high-temperature results required a radical change in the seismic anisotropy model with one-third of *c*-axes being aligned normal to the Earth's rotation axis giving an excellent agreement with travel time differences. However, recently new calculations (Gannarelli *et al.*, 2003, 2005; Sha and Cohen, 2006) have failed to reproduce the large change in *c*/*a* axial ratios with temperature, which casts some doubt on the elastic constants of Steinle-Neumann *et al.* at high temperature. It should be said that high-temperature first-principls calculations represent frontier science in this area. What is perhaps even more troublesome is that there is very poor agreement, or perhaps one should say total disagreement, between experimental results and first principles for P- and S-wave velocity distribution in single-crystal h.c.p. iron at low temperature and high pressure where methods are considered to be well established. Experimental techniques can be criticized as one has to use polycrystalline samples and so the results represent a lower bound on anisotropy of the single-crystal elastic constants. The diamond anvil cells imposed a strong axial strain on the samples that results in a very strong orientation of *c*-axes parallel to the compression axis that can be used as reasonable proxy for a single crystal, even before corrections for the presence of CPO are made. The radial X-ray diffraction techniques allow the measurement of the CPO (texture) *in situ*; on the other hand, it requires a model of the microscopic stress–strain distribution to determine the single-crystal elastic constants, where at present simple models like the constant stress (Reuss) are used. The fact that the samples undergo elastic and plastic strain complicates the rigorous interpretation of this type of experiment (Weidner *et al.*, 2004; Merkel *et al.*, 2006b) in terms of elastic constants. One reassuring observation is that different experimental techniques, for example, radial X-ray diffraction and inelastic X-ray scattering, both give a similar P-wave velocity distribution with the maximum velocity at 45° to the *c*- and *a*-axes and an apparently increasing anisotropy with increasing pressure. All reports of first-principles calculations at 0 K give similar P-wave velocity with the maximum parallel to the *c*-axis. However, differences can be seen in the magnitude of the anisotropy and the position of the minimum velocity, minimum at 50° from the *c*-axis (Stixrude and Cohen, 1995; Steinle-Neumann *et al.*, 2001) or at 90° (Laio *et al.*, 2000; Vočadlo *et al.*, 2003b). The differences between experiment and theory are even more flagrant for S-waves. The experimental data show that SH is greater than SV except at more than 60° from the *c*-axis, SH has maximum parallel to the *c*-axis, and SV has minimum velocity at 45° to the *c*-axis. Results from theory show more variability

between authors, SV is greater than SH, and SV has maximum velocity at 45° to the *c*-axis in the work of Stixrude and Cohen (1995) and Steinle-Neumann *et al.* (2001), which is the exact opposite of the experimental results. Laio *et al.* (2000) and Vočadlo *et al.* (2003b) have a much lower S-wave anisotropy than in the experiments. From this brief survey of recent results in this field, it is clear that there is still much to do to unravel the meaning of seismic anisotropy of the inner core and physics of iron at high pressure and temperature in particular. Although the stability of h.c.p. iron at inner-core conditions has been questioned from time to time on experimental or theoretical grounds, that the inner core may not be pure iron (e.g., Poirier, 1994), the major problem at the present time is to get agreement between theory and experiment at the same physical conditions. Interpretation of the mechanisms responsible for inner-core seismic anisotropy is out of the question without a reliable estimate of elastic constants of h.c.p. iron; indeed if the inner core is composed of h.c.p. iron (e.g., Beghein and Trampert, 2003; Vočadlo *et al.*, 2003a), nowhere in the Earth is Francis Birch's 'high pressure language' (positive proof = vague suggestion etc, Birch, 1952) more appropriate.

# 3 Rock Physics

## 3.1 Introduction

In this section the contribution of CPO to seismic anisotropy in the deep Earth with cases of olivine and the role of melt is illustrated. The CPO in rocks of upper-mantle origin is now well established (e.g., Mercier, 1985; Nicolas and Christensen, 1987; Mainprice *et al.*, 2000) as direct samples are readily available from the first 50 km or so, and xenoliths provide further sampling down to depths of about 220 km. Ben Ismaïl and Mainprice (1998) created a database of olivine CPO patterns from a variety of the upper-mantle geodynamic environments (ophiolites, subduction zones, and kimberlites) with a range of microstructures. However, for the deeper mantle (e.g., Wenk *et al.*, 2004) and inner core (e.g., Merkel *et al.*, 2005) we had to rely traditionally on high-pressure and -temperature experiments to characterize the CPO at extreme conditions. In recent years, the introduction of various types of polycrystalline plasticity models to stimulate CPO development for complex strain paths has allowed a high degree of forward modeling using either slip systems determined from studying experimentally deformed samples using transmission electron microscopy (e.g., wadsleyite – Thurel *et al.*, 2003; ringwoodite – Karato *et al.*, 1998), X-ray diffraction peak broadening analysis for electron radiation sensitive minerals (e.g., Mg-perovskite – Cordier *et al.*, 2004b) or predicted systems from atomic-scale modeling of dislocations (e.g., olivine – Durinck *et al.*, 2005a, 2005b; ringwoodite – Carrez *et al.*, 2006). The polycrystalline plasticity modeling has allowed forward modeling of upper mantle (e.g., Chastel *et al.*, 1993; Blackman *et al.*, 1996; Tommasi, 1998), transition zone (e.g., Tommasi *et al.*, 2004), lower mantle (e.g., Wenk *et al.*, 2006), D″ layer (e.g., Merkel *et al.*, 2006a), and the inner core (e.g., Jeanloz and Wenk, 1988; Wenk *et al.*, 2000).

## 3.2 Olivine the Most Studied Mineral: State of the Art – Temperature, Pressure, Water, Melt, ETC

Until the papers by Jung and Karato (2001), Katayama *et al.* (2004), and Katayama and Karato (2006) were published, the perception of olivine dominated flow in the upper mantle was quite simple with [100]{0kl} slip be universally accepted as the mechanism responsable for plastic flow and the related seismic anisotropy (e.g., Mainprice *et al.*, 2000). The experimental deformation of olivine in hydrous conditions at 2 GPa pressure and high temperature by Karato and co-workers produced a new type of olivine CPO developed at low stress with [001] parallel to the shear direction and (100) in the shear plane, which they called C-type, which is associated with high water content. They introduced a new olivine CPO classification that illustrated the role of stress and water content as the controlling factors for the development of five CPO types (A, B, C, D, and E) (**Figure 21**). The five CPO types are assumed to represent the dominant slip system activity on A ≡ [100](010), B ≡ [001](010), C ≡ [001](100), D ≡ [100]{0kl}, and E ≡ [100](001). The Ben Ismaïl and Mainprice (1998) olivine CPO database with 110 samples has been taken and the percentages for each CPO type and added an additional class called AG-type (or axial b- [010] girdle by Tommasi *et al.*, 2000) have been estimated which is quite common in naturally deformed samples. The CPO types in percentage of the database are A-type (49.5%), D-type (23.8%), AG-type (10.1%), E-type (7.3%), B-type (7.3%), and C-type (1.8%). It is clear that CPO associated with [100] direction

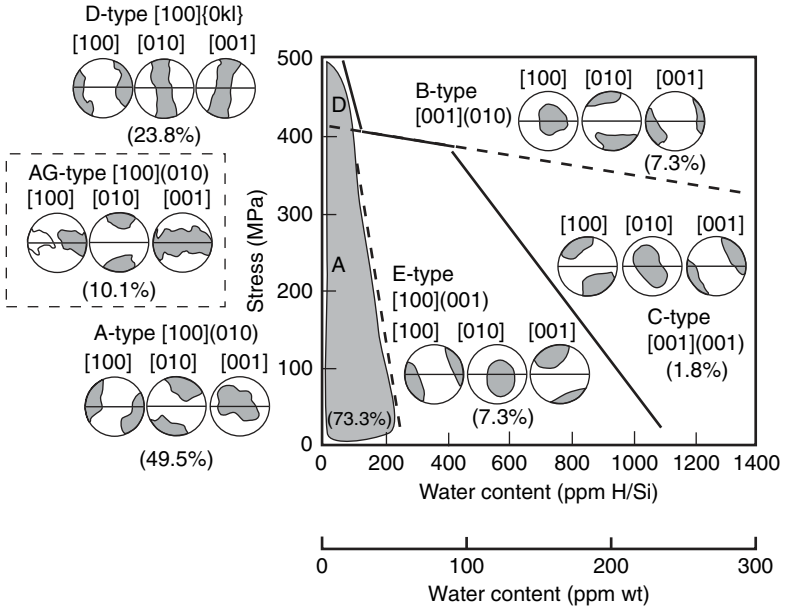


**Figure 21** The classification of olivine CPO proposed by Jung and Karato (2001) as a function of stress and water content. The water content scale in ppm H/Si is that originally used by Jung and Karato. The water content scale in ppm wt is more recent calibration used by Bolfan-Casanova (2005). The numbers in brackets are the percentage of samples with the fabric types found in the database of Ben Ismaïl and Mainprice (1998).

slip (A, AG, D, E types) represent 90.8% of the database and therefore only 9.2% are associated with [001] direction slip (B and C types). Natural examples of all CPO types taken from the database are shown in **Figure 22**, with the corresponding seismic properties in **Figure 23**. There is only one unambiguous C-type sample and another with transitional CPO between B and C types. The database contains samples from palaeo-mid ocean ridges (e.g., Oman ophiolite), the circum Pacific suduction zones (e.g., Philippines, New Caledonia, Canada) and subcontinental mantle (e.g., kimberlite xenoliths from South Africa). There have been some recent reports of the new olivine C-type CPO (e.g., Mizukami *et al.*, 2004) associated with high water content and others from ultrahigh pressure (UHP) rocks (e.g., Xu *et al.*, 2006) have relatively low water contents. It is instructive to look at the solubility of water in olivine to understand the potential importance of the C-type CPO. In **Figure 24**, the experimentally determined solubility of water in nominally anhydrous upper-mantle silicates (olivine, cpw, opx, and garnet) in the presence of free water are shown over the upper-mantle pressure range. The values given in the review by Bolfan-Casanova (2005) are in $H_2O$ ppm wt using the calibration of Bell *et al.* (2003), so the values of Karato *et al.* in $H/10^6$ Si using the infra-red calibration of Paterson (1982) have to be multiplied by 0.22 to obtain $H_20$ ppm wt. If free water is available, then olivine can incorporate, especially below 70 km depth, many times the concentration necessary for C-type CPO to develop according to the results of Karato and co-workers.

Why is it that the C-type CPO is relatively rare? It is certain that deforming olivine moving slowly toward the surface will lose its water due to the rapid diffusion of hydrogen. For example, even xenoliths transported to the surface in a matter of hours lose a significant fraction of their initial concentration (Demouchy *et al.*, 2006). Hence, it very plausible that in the shallow mantle (less than about 70 km depth), the C-type will not develop because the solubility of water is too low in olivine at equilibrium conditions and that 'wet' olivine upwelling from greater depths and moving toward the surface by slow geodynamic processes will lose their excess water by hydrogen diffusion. In addition, any 'wet' olivine coming into contact with basalt melt tends to 'dehydrate' as the solubility of water in the melt phase is hundreds to thousands of times greater than olivine (e.g., Hirth and Kohlstedt, 1996). The melting will occur in upwelling 'wet' peridotites at a well-defined depth when the solidus is exceeded and the volume fraction

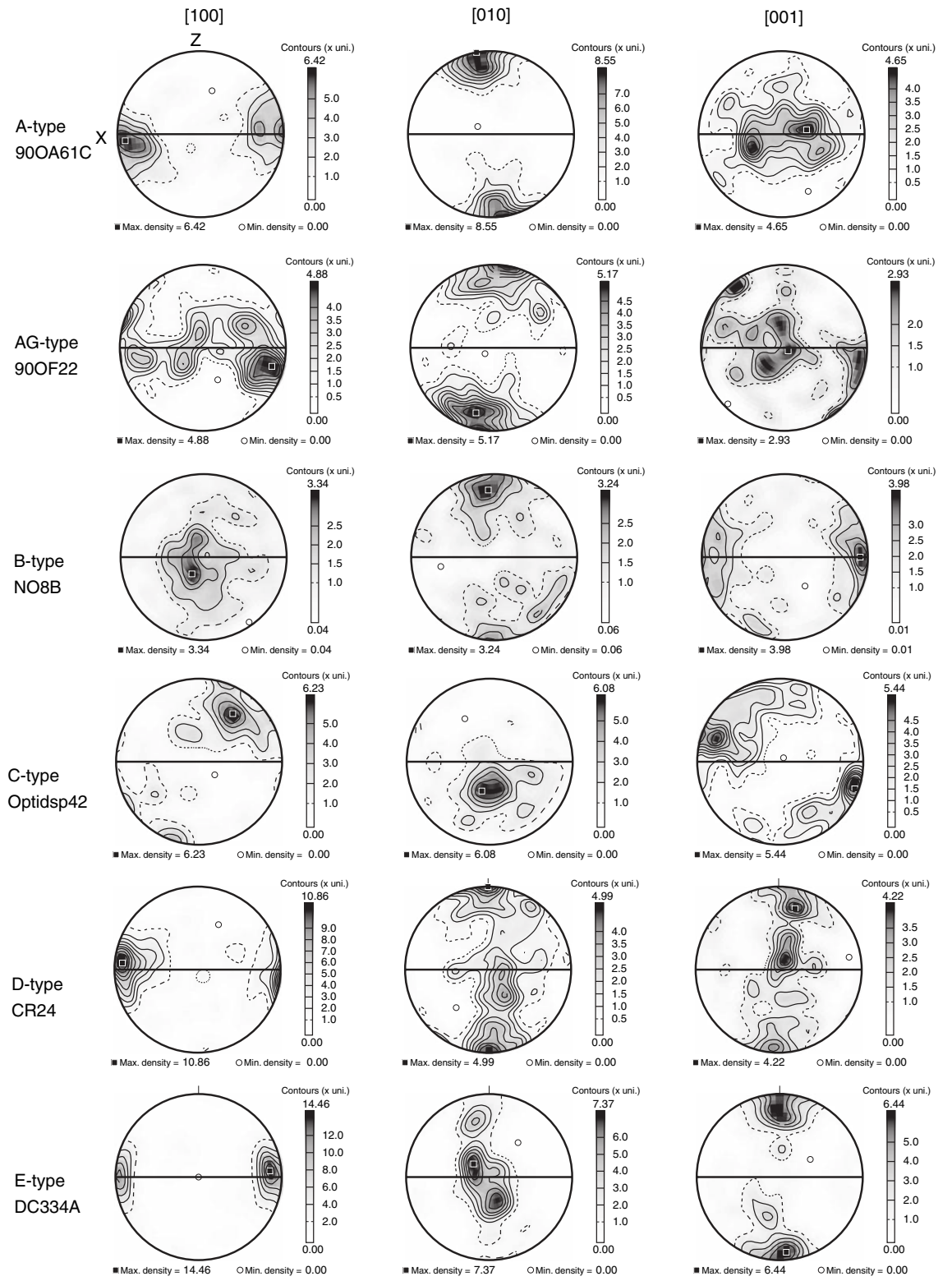


**Figure 22** Natural examples of olivine CPO types from the Ben Ismaïl and Mainprice (1998) database, except the B-type sample NO8B from K. Mishibayashi (per.com., 2006). X marks the lineation, the horizontal line is the foliation plane. Contours given in times are uniform.

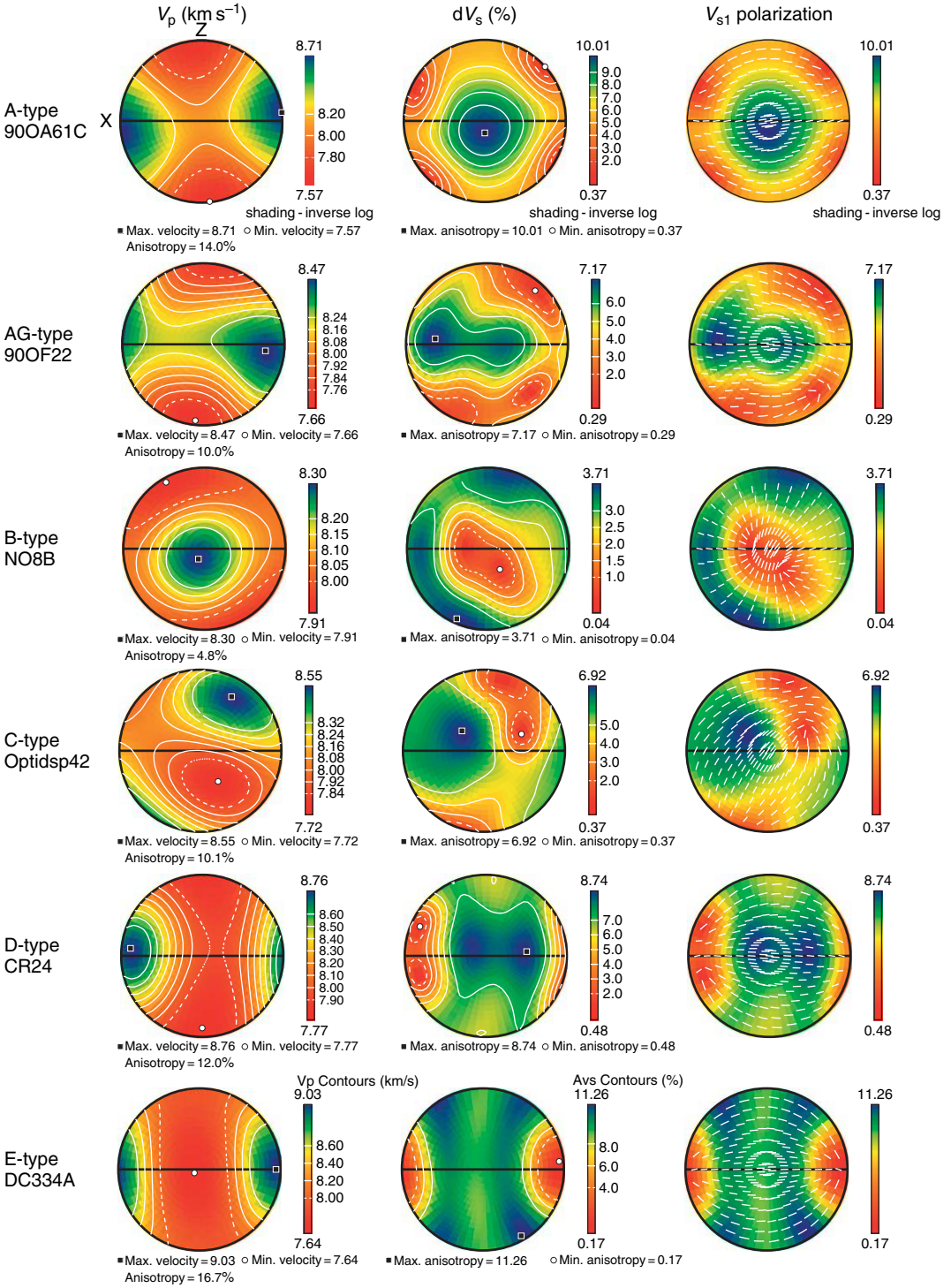


**Figure 23** Anisotropic seismic properties of olivine at 1000°C and 3 GPa with CPO of the samples in **Figure 20**. X marks the lineation, the horizontal line is the foliation plane.

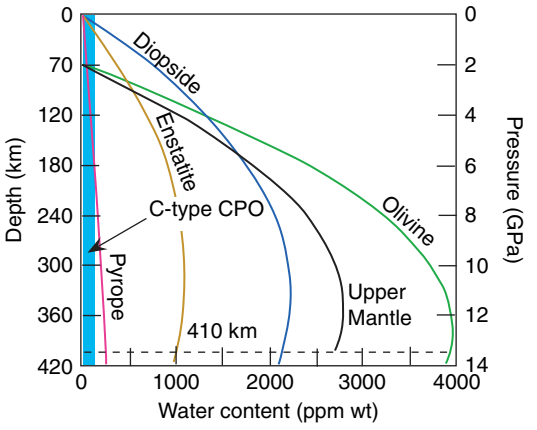


**Figure 24** The variation of the water content of upper mantle silicates in the presence of free water from Bolfan-Casanova (2005). The water content of the experimentally produced C-type CPO by Jung and Karato is indicated by the light blue region.

of melt produced is controlled by the amount of water present. Karato and Jung (1998) estimate that melting is initiated at about 160 km in the normal mid-ocean ridge (NMORB) source regions and at greater depth of 250 km in back-arc-type MORB with the production of 0.25–1.00% melt, respectively. Given the small melt fraction the water content olivine is unlikely to be greatly reduced. As more significant melting will of course occur when the 'dry' soldius is exceeded with 0.3% melt per km melting at about 70 km, then melt (3% or more) is quickly produced and the water content of olivine will be greatly reduced. So the action of reduced solubility and selective partitioning of water into the melt phase are likely made the first 70 km of oceanic mantle olivine very dry. The other region where water is certainly present is in subduction zones, where relatively water-rich sediments, oceanic crust, and partly hydrated oceanic lithosphere will add to the hydrous budget of the descending slab. Partial melting is confined in the mantle wedge to the hottest regions, where the temperatures approach the undisturbed asthenospheric conditions at 45–70 km depth, and 5–25 wt.% melt will be produced by a lherzolitic source (Ulmer, 2001). Hence even in the mantle wedge the presence of large volume fractions of melt is likely to reduce the water content of olivine to low levels, possibly below the threshold of the C-type CPO, for depths shallower than 70 km.

Is water the only reason controlling the development of the C-type fabric or [001] direction slip in general? The development of slip in the [001] direction on (010) and (100) planes at high stresses in olivine has been known experimentally since transmission electron microscopy study of Phakey *et al.* (1972). Recently, Couvy *et al.* (2004) have produced B- and C-type CPO in fosterite at very high pressure (11GPa) using nominally dry starting materials. However, as pointed out by Karato (2006) the infrared spectrophotometry of the deformed samples revealed the present of water, presumably due to the dehydatation of sample assembly at high pressure. However, concentration of water in the fosterite increases linearly with time at high pressure, whereas the CPO is acquired at the beginning of the experiment in the stress-relaxation tests conducted by Couvy *et al.* (2004), so it is by no means certain that significant water was present at the beginning of the experiment. Mainprice *et al.* (2005) suggested that pressure was the controlling variable, partly inspired by recent atomic modeling of dislocations in fosterite (Durinck *et al.*, 2005b), which shows that the energy barrier for [100] direction slip increases with hydrostatic pressure, whereas for [001] it is constant, which could explain the transition form [100] to [001] with pressure. It remains a possibility that [001] slip occurs at high pressure in dry samples, but experiments with better control of water content are needed to confirm or deny this possibility.

What are the seismic consequences of the recent discovery of C-type CPO in experiments in hydrous conditions? The classic view of mantle flow dominated by [100]{0kl} slip is not challenged by this new discovery as most of the upper mantle is will be dry and at low stress. The CPO associated with [100] slip, that is, 90.8% of the Ben Ismaïl and Mainprice database (1998), produces seismic azimuthal anisotropy for horizontal flow with maximum $V_p$, polarization of the fastest S-wave parallel to the flow direction and $V_{SH} > V_{SV}$. The seismic properties of all the CPO types are shown in **Figure 23**. It remains to apply the C-, B-, and possibly E-type fabrics to hydrated section of the upper mantle. Katayama and Karato (2006) propose that the mantle wedge above subduction zones are regions where the new CPO types are likely to occur, with the B-type CPO occurring in the low-temperature (high stress and wet) subduction where an old plate is subducted (e.g., NE Japan). The B-type fabric would result anisotropy parallel normal to plate motion (i.e., parallel to the trench). In the back-arc, the A-type (or E-type reported by Michibayashi *et al.* (2006) in the back-arc region of NE Japan) fabric is likely dominant because water content is significantly reduced in this region due to

the generation of island arc magma. Changes in the dominant type of olivine fabric can result in complex seismic anisotropy, in which the fast shear-wave polarization direction is parallel to the trench in the fore-arc, but is normal to it in the back-arc (Kneller *et al.*, 2005). In higher-temperture subduction zones (e.g., NW America, Cascades) the C-type CPO will develop in the mantle wedge (low stress and wet), giving rise to anisotropy parallel to plate motion (i.e., normal to the trench). Although these models are attractive, trench parallel flow was first described by Russo and Silver (1994) for flow beneath the Nasca Plate, where there is a considerable path length of anisotropic mantle to generate the observed differential arrival time of the S-waves. On the other hand, a well-exposed peridotite body analog of arc-parallel flow of south central Alaska reveals that horizontal stretching lineations and olivine [100] slip directions are subparallel to the Talkeetna arc for over 200 km, clearly indicating that mantle flow was parallel to the arc axis (Mehl *et al.*, 2003). The measured CPO of olivine shows that the E-type fabric is dominant along the Talkeetna arc; in this case, foliation is parallel to the Moho suggesting arc parallel shear with a horizontal flow plane. Tommasi *et al.* (2006) also report the E-type fabric with trench parallel tectonic context in a highly depleted peridotie massif from the Canadian Cordillera in dunites associated with high degrees of melting, and hence probably dry, whereas harzburgites have an A-type fabric. In limiting the path length to the region of no melting, in coldest part of the mantle wedge, above the plate, the vertical thickness is also constrained to about 45–70 km depth, if one accepts the arguments for melting (Ulmer, 2001). For NE Japan the volcanic front is about 70 km above the top of the slab defined by the hypocenter distribution of intermediate-depth earthquakes (Nakajima and Hasegawa, 2005, their figure1), typical S-wave delay times are 0.17 s (maximum 0.33 s, minimum 0.07 s). The delay times from local slab sources are close to the minimum of 0.07 s for trench parallel fast S-wave polarizations to the east of the volcanic front (i.e., above the coldest part of the mantle wedge) and are over 0.20 s for the trench normal values (i.e., the back-arc side). Are these CPO capable of producing a recordable seismic anisotropy over such a short path length? The vertical S-wave anisotropy can be estimated from the delay time given by Nakajima and Hasegawa (2005) (e.g., 0.17 s), the vertical path length (e.g., 70 km), the average S-wave velocity (e.g., 4.46 km $s^{-1}$) to give a 1.1% S-wave anisotropy, which is less than maximum S-wave anisotropy of 1.7% given for a B-type CPO in a vertical direction given by Katayama and Karato (2006) for horizontal flow, so B-type CPO is compatible with seismic delay time, even if we allow some complexity in the flow pattern. The case for C-type in the high-temperature subduction zones is more difficult to test, as the S-wave polarization pattern will be the same for C- and A-types (Katayama and Karato, 2006). The clear seismic observations of fast S-wave polarizations parallel to plate motion (trench normal) given for the Cascadia (Currie *et al.*, 2004) and Tonga (Fischer *et al.*, 1998) subduction zones, which would be compatible with A- or C-types. In general, some care has to taken to separate below slab, slab, and above slab anisotropy components to test mantle wedge anisotropy.

### 3.3 Seismic Anisotropy and Melt

The understanding of the complex interplay between plate separation, mantle convection, adiabatic decompression melting, and associated volcanism at mid-ocean ridges in the upper mantle (e.g., Solomon and Toomey, 1992), presence of melt in the deep mantle in the D″ layer (e.g., Williams and Garnero, 1996) and inner core (Singh *et al.*, 2000) are challenges for seismology and mineral physics. For the upper mantle two contrasting approaches have been used to study mid-ocean ridges, on the one hand marine geophysical (mainly seismic) studies of active ridges and on the other hand geological field studies of ophiolites, which represent 'fossil' mid-ocean ridges. These contrasting methods have yielded very different views about the dimensions of the mid-ocean ridge or axial magma chambers (AMCs). The seismic studies have given us three-dimensional information about seismic velocity and attenuation in the axial region. The critical question is how can this data be interpreted in terms of geological structure and processes? To do so we need data on the seismic properties at seismic frequencies of melt containing rocks, such as hartzburgites, at the appropriate temperature and pressure conditions. Until recently laboratory data for filling these conditions was limited for direct laboratory measurements to isotropic aggregates (e.g. Jackson *et al.*, 2002), but deformation of initially isotropic aggregates with a controlled melt fraction in shear (e.g., Zimmerman *et al.*, 1999; Holtzman *et al.*, 2003) allows simultaneous development of the CPO and anisotropic melt distribution. To obtain information concerning anisotropic rocks, one can use various modeling techniques to estimate

the seismic properties of idealized rocks (e.g., Mainprice, 1997; Jousselin and Mainprice, 1998; Taylor and Singh, 2002) or experimentally deformed samples in shear (e.g., Holtzman *et al.*, 2003). This approach has been used in the past for isotropic background media with random orientation distributions of liquid filled inclusions (e.g., Mavko, 1980; Schmeling, 1985; Takei, 2002). However, their direct application to mid-ocean ridge rocks is compromised by two factors. First, field observations on rock samples from ophiolites show that the harzburgites found in the mid-ocean ridges have strong crystal-preferred orientations (e.g., Nicolas and Boudier, 1995), which results in the strong elastic anisotropy of the background medium. For the case of the D″ layer and the inner core the nature of the background media is not well defined and an isotropic medium has been assumed (Williams and Garnero, 1996; Singh *et al.*, 2000). Second, field observations show that melt films tend to be segregated in the foliation or in veins, so that the melt-filled inclusions should be modeled with a preferred shape orientation.

The rock matrix containing melt inclusions is modeled using effective medium theory, to represent the overall elastic behavior of the body. The microstructure of the background medium is represented by the elastic constants of the crystalline rock, including the CPO of the minerals and their volume fractions. Quantitative estimates of how rock properties vary with composition and CPO can be divided into two classes. There are those that take into account only the volume fractions with simple homogenous strain or stress field and upper and lower bounds for anisotropic materials such as Voigt–Reuss bounds, which give unacceptably wide bounds when the elastic contrast between the phases is very strong, such as a solid and a liquid. The other class takes into account some simple aspects of the microstructure, such as inclusion shape and orientation. There are two methods for the implementation of the inclusions in effective medium theory to cover a wide range of concentrations; both methods are based on the analytic solution for the elastic distortion due to the insertion of a single inclusion into an infinite elastic medium given by Eshelby (1957). The uniform elastic strain tensor inside the inclusion ($\varepsilon_{ij}$) is given by

$$\varepsilon_{ij} = \frac{1}{2}\left(G_{ikjl} + G_{jkil}\right) C_{klmn}\, \varepsilon^{*} mn$$

where $G_{ikjl}$ is the tensor Green's function associated with displacement due to a unit force applied in a given direction, $C_{klmn}$ are the components of the background medium elastic stiffness tensor and $\varepsilon^{*}_{mn}$ is the eigenstrain or stress-free strain tensor due to the imaginary removal of the inclusion from the constraining matrix. The symmetrical tensor Green's function $G_{ikjl}$ is given by Mura (1987)

$$G_{ikjl} = \frac{1}{4\pi}\int_0^{\pi} \sin\theta \, \mathrm{d}\theta \int_0^{2\pi} \left(K_{ij}^{-1}(x) x_k x_1\right) \mathrm{d}\phi$$

with $K_{ip}(x) = C_{ijpl} x_j x_l$, the Christoffel stiffness tensor for direction ($x$), and $x_1 = \sin\theta \cos\phi / a_1$, $x_2 = \sin\theta \sin\phi / a_2$ and $x_3 = \cos\theta / a_3$ .

The angles $\theta$ and $\phi$ are the spherical coordinates that define the vector $x$ with respect to the principal axes of the ellipsoidal inclusion. The semiaxes of the ellipsoid are given by $a_1$, $a_2$, and $a_3$. The integration to obtain the tensor Green's function must be done by numerical methods, as no analytical solutions exist for a general triclinic elastic background medium. Greater numerical efficiency, particularly for inclusions with large axial ratios, is achieved by taking the Fourier transform of $G_{ikjl}$ and using the symmetry of the triaxial ellipsoid to reduce the amount of integration (e.g., Barnett, 1972). The self-consistent (SC) method introduced by Hill (1965) uses the solution for a single inclusion and approximates the interaction of many inclusions by replacing the background medium with the effective medium.

In the formulation of SC scheme by Willis (1977), a ratio of the strain inside the inclusion to the strain in the host medium can be identified as $A_i$,

$$A_i = \left[I + G(C_i - C^{\mathrm{scs}})\right]^{-1}$$

$$\langle \varepsilon^{\mathrm{scs}} \rangle = \sum_{i=1}^{i=n} V_i A_i \langle \sigma^{\mathrm{scs}} \rangle = \sum_{i=1}^{i=n} V_i C_i A_i$$

$$C^{\mathrm{scs}} = \langle \sigma^{\mathrm{scs}} \rangle \langle \varepsilon^{\mathrm{scs}} \rangle^{-1}$$

where $I$ is the symmetric four rank unit tensor $I_{ijkl} = (1/2)\ (\delta_{ik}\ \delta_{jl} + \delta_{il}\ \delta_{jk})$, $\delta_{ik}$ is the Kronecker delta, $V_i$ is volume fraction and $C_i$ are the elastic moduli of the $i$th inclusion. The elastic contants of the SC scheme ($C^{\mathrm{scs}}$) occur on both sides of the equation because of the stain ratio factor ($A$), so that solution has to be found by iteration. This method is the most widely used in Earth sciences, being relatively simple to compute and well established (e.g., Kendall and Silver, 1996, 1998). Certain consider that when the SC is used for two phases, for example, a melt added to a solid crystalline background matrix, the melt inclusions are isolated (not connected) below 40% fluid content, and the solid and fluid phases can only be considered to be mutually fully

interconnected (bi-connected) between 40% and 60%. For our application to magma bodies, one would expect such interconnection at much lower melt fractions. The second method is DEM. This models a two-phase composite by incrementally adding inclusions of melt phase to a crystalline background phase and then recalculating the new effective background material at each increment. McLaughlin (1977) derived the tensorial equations for DEM as follows:

$$\frac{\mathrm{d}C^{\mathrm{DEM}}}{\mathrm{d}V} = \frac{1}{(1-V)}\left(C_i - C^{\mathrm{DEM}}\right)A_i$$

Here again the term $A_i$ is the strain concentration factor coming from the Eshelby formulation of the inclusion problem. To evaluate the elastic moduli ($C^{\mathrm{DEM}}$) at a given volume fraction $V$, one needs to specify the starting value of $C^{\mathrm{DEM}}$ and the component that is the inclusion. Unlike the SC, the DEM is limited to two components A and B. Either A or B can be considered to be the included phase. The initial value of $C^{\mathrm{DEM}}$ is clearly defined at 100% of phase A or B. The incremental approach allows the calculations at any composition irrespective of starting concentrations of original phases. This method is also implemented numerically and addresses the drawback of the SC in that either phase can be fully interconnected at any concentration. Taylor and Singh (2002) attempted to take advantages of both of these methods and minimize their shortcomings by using a combined effective medium method, a combination of the SC and DEM theory. Specifically, they used the formulation originally proposed by Hornby *et al.* (1994) for shales, an initial melt-crystalline composite is calculated using the SC with melt fraction in the range 40–60% where they claim that each phase (melt and solid) is connected and then uses the DEM method to incrementally calculate the desired final composition that may be at any concentration with a bi-connected microstructure.

To illustrate the effect on oriented melt inclusions, the data from the study of a harzburgite sample (90OF22) collected from the Moho transition zone of the Oman ophiolite (Mainprice, 1997) will be used. The crystal-preferred orientation and petrology of the sample have been described by Boudier and Nicolas (1995) and CPO of the olivine (AG type) is given in **Figure 22**. The mapping area records a zone of intense melt circulation below a fast spreading palaeo mid-ocean ridge at a level between the asthenospheric mantle and the oceanic crust. The DEM effective medium method combined with Gassmann's (1951) poro-elastic theory to ensure connectivity of the melt system at low frequency relevant to seismology is used (see Mainprice (1997) for further details and references). The harzburgite (90OF22) has a composition of 71% olivine and 29% opx. The composition combined with CPO of the constituent minerals and elastic constants extrapolated to simulate conditions of 1200°C and 200 MPa where the basalt magma would be liquid predicts the following P-wave velocities in the principal structural direction $X = 7.82$, $Y = 7.69$, $Z = 7.38\ \mathrm{km\,s^{-1}}$ ($X$ = lineation, $Z$ = normal to foliation, $Y$ is perpendicular to $X$ and $Z$). The crystalline rock with no melt has essentially an orthorhombic seismic anisotropy. First, by adding the basalt spherical basalt inclusions, the velocities for P- and S-waves decrease and attuation increases (**Figure 25**) with increasing melt fraction and the rock becomes less anisotropic, but preserves its orthorhombic symmetry. When pancake-shaped basalt inclusions with $X{:}Y{:}Z = 50{:}50{:}1$ are added, to simulate the distribution of melt in the foliation plane observed by Boudier and Nicolas (1995), certain aspects of the original orthorhombic symmetry of the rock are preserved, such as the difference between $V_{\mathrm{p}}$ in the $X$- and $Y$-directions. However, many velocities and attenuations change illustrating the domination of the transverse isotropic symmetry with $Z$-direction symmetry axis associated with the pancake-shaped basalt inclusions. The $V_{\mathrm{p}}$ in the $Y$-direction decreases rapidly with increasing melt fraction, causing the seismic anisotropy of P-wave velocities between $Z$ and $X$ or $Y$ to increase. The contrast in behavior for P-wave attenuation is also very strong with attenuation ($Q^{-1}$) increasing for $Z$ and decreasing for $X$- and $Y$-directions. For the S-waves, the effects are even more dramatic and more like a transverse isotropic behavior. The S-waves propagating in $X$-direction with a $Y$-polarization, $V_{\mathrm{s}}X(Y)$, and those propagating in the $Y$-direction with $X$-polarization, $V_{\mathrm{s}}Y(X)$ (see **Figure 26** for directions), are fast velocities; because they are propagating along the $XY$ (foliation) plane with polarizations in $XY$ plane, we can call these $V_{\mathrm{SH}}$ waves for a horizontal foliation. In contrast, all the other S-waves have either their propagation or polarization (or both) direction in the $Z$-direction and have the same lower velocity, these we can call $V_{\mathrm{SV}}$. Similarly for the S-wave attenuation $V_{\mathrm{SH}}$ is less attenuated than $V_{\mathrm{SV}}$. From this study we can see that a few percent of aligned melt inclusions with high axial ratio can change the symmetry and increase the anisotropy of crystalline aggregate (see

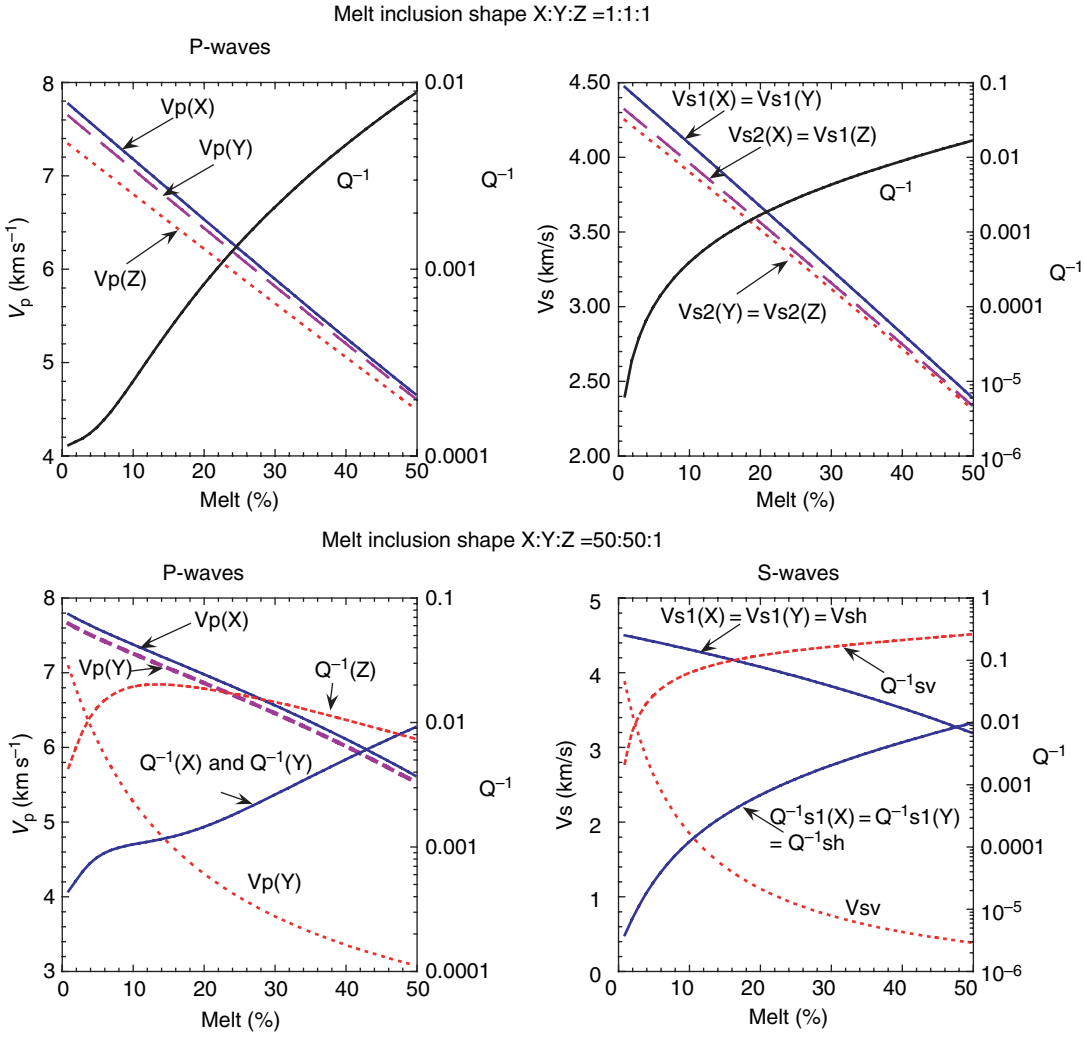


**Figure 25** The effect of increasing basalt melt fraction on the seismic velocities and attenuation ($Q^{-1}$) of a hartzburgite (see text for details).

Figure 26 for summary), completely replacing the anisotropy associated with crystalline background medium in the case of S-waves. Taylor and Singh (2002) come to the same conclusion, that S-wave anisotropy is an important diagnostic tool for the study of magma chambers and regions of partial melting.

One of the most ambitious scientific programs in recent years was the Mantle Electromagnetic and Tomography (MELT) Experiment that was designed to investigate the forces that drive flow in the mantle beneath a mid-ocean ridge, MELT Seismic Team, (1998). Two end-member models often proposed can be classified into two groups; the flow is a passive response to diverging plate motions, or buoyancy forces supplied a plate-independent component variation of density caused by pressure release partial melting of the ascending peridotite. The primary objective in this study was to constrain the seismic structure and geometry of mantle flow and its relationship to melt generation by using teleseismic body waves and surface waves recorded by the MELT seismic array beneath the superfast spreading southern East Pacific Rise (EPR). The observed seismic signal was expected to be the product of elastic anisotropy caused by the alignment of olivine crystals due to mantle flow and the presence of aligned melt channels or pockets of unknown structure at depth (e.g., Kendall 1994; Blackman *et al.*, 1996; Blackman and Kendall, 1997; Mainprice 1997). Observations

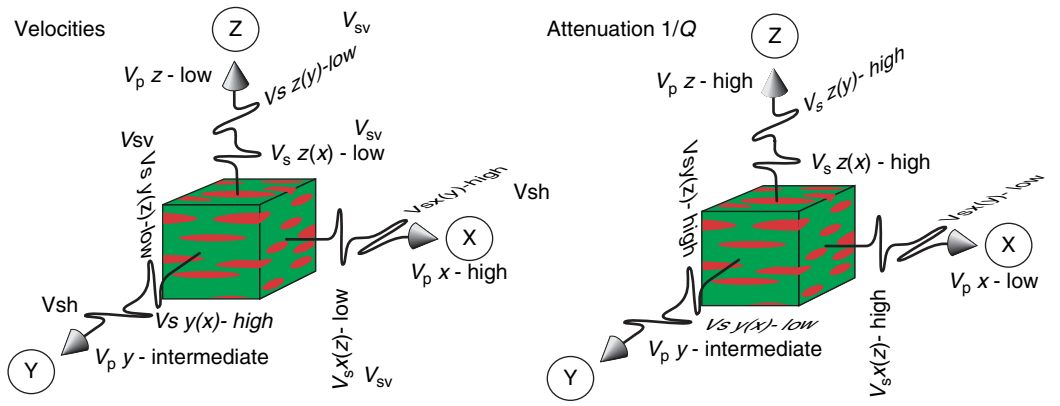


**Figure 26** A graphical illustration of the 'pancake'-shaped melt inclusions (red) in the foliation (*XY*) plane (where *X* is the lineation) and the relation between velocity and attenuation ($Q^{-1}$). The melt is distributed in the foliation plane. The velocities have an initial orthorhombic symmetry with $V_p$ $X > Y > Z$. The directions of high velocity are associated with low attenuation. P-waves normal to the foliation have the lowest velocity. S-waves with polarizations in the foliation (*XY*) plane have the highest velocities ($V_{SH}$). Diagram inspired a figure in the thesis of Barruol (1993).

revealed that on the Pacific plate (western) side of the EPR had lower seismic velocities (Forsyth *et al.*, 1998; Toomey *et al.*, 1998) and greater shear wave splitting (Wolfe and Solomon, 1998). The shear wave splitting showed that the fast shear polarization was consistently parallel to the speading direction, and at no time parallel to the ridge axis with no null splitting being recorded near the ridge axis. In addition, the delay time between S-wave arrivals on the Pacific plate was twice that of the Nasca plate. P delays decreased within 100 km of the ridge axis (Toomey *et al.*, 1998) and Rayleigh surface waves indicated a decrease in azimuthal anisotropy near the ridge axis. Any model of the EPR must take into account that the average spreading rate at 17° S on the ridge is 73 mm $yr^{-1}$ and the ridge migrates 32 mm $yr^{-1}$ to the west. Anisotropic modeling of the P and S data within 500 km of the ridge axis by Toomey *et al.* (2002) and Hammond and Toomey (2003) showed that a best-fitting finite-strain hexagonal-symmetry two-dimensional flow model had an asymmetric distribution of higher melt fraction and temperature, dipping to the west under the Pacific plate and lower melt fraction and temperature with an essentially horizontal structure under the Nasca plate. Hammond and Toomey (2003) introduce low melt fractions, <2%) in relaxed (connected) cuspate melt pockets (Hammond and Humphreys, 2000) to match the observed velocities. Blackman and Kendall (2002) used a three-dimensional texture flow model to predicted pattern of upper-mantle flow beneath the EPR oceanic spreading center with asymmetric asthenospheric flow pattern. Blackman and Kendall (2002) explored a series of models for the EPR and found that asymmetric thermal structure proposed by Toomey *et al.* (2002) produced the model in closest agreement with seismic observations. The three-dimensional model shows that shear wave splitting will be lowest at about 50 km to the west of the EPR on the Pacific plate with similar low value at 400 km to the east on the Nasca plate, and not the ridge axis because of the underlying asymmetric mantle structure. The MELT experiment has shown that melt flow beneath a fast spreading ridge is more complicated than originally predicted, with a deep asymmetric structure present to 200 km depth. The influence of the near surface configuration (e.g., ridge migration) was also important in controlling the asthenospheric return flow toward the Pacific superswell in the west (Hammond and Toomey, 2003). The influence of melt geometry appears to be small in the case of the EPR, as the essential anisotropic seismic structure is captured by models that do not have melt geometries with strong shape-preferred orientation. The situation may be different for the oceanic crust at fast oceanic spreading centers. The seismic anisotropy in regions of important melt production, such as Iceland (Bjarnason *et al.*, 2002), does not show the influence of melt geometry on anisotropy, but rather the influence of large-scale mantle flow. In other contexts, such as the rifting, for example, the Red Sea (Vauchez *et al.*, 2000) and East African Rifts (Kendall *et al.*, 2004), the melt geometry does seem to have an important influence of seismic anisotropy.

## 4 Conclusions

In this chapter some aspects of seismology that have a bearing on the geodynamics of the deep interior of the Earth have been reviewed. In particular, the emphasis is on the importance of seismic anisotropy and the variation of anisotropy on a global and regional basis. In the one-dimensional PREM model (Dziewoński and Anderson, 1981), anisotropy was confined to the first 250 km of the upper mantle. Subsequently, other studies of the mantle found various additional forms of global anisotropy associated with the transition zone, the 670 km boundary layer, and the D″ layer (e.g., Montagner, 1994a, 1994b; Montagner and Kennett, 1996; Montagner, 1998). The most recent global studies using more complete data sets and new methods of analysis emphasize the exceptionally strong nature of the upper-mantle anisotropy, the anisotropy of the D″ layer and no significant deviation from the original isotropic PREM for the rest of the mantle (e.g., Beghein *et al.*, 2006; Panning and Romanowicz, 2006). To explain velocity variations that are observed in the mantle studies using probabilistic tomography, the authors put the emphasis on chemical heterogeneity and lateral temperature variations in the mantle (Trampert *et al.*, 2004; Deschamps and Trampert, 2003). Trampert and van der Hilst (2005) argue that spatial variations in bulk major element composition dominates buoyancy in the lowermost mantle, but even at shallower depths, its contribution to buoyancy is comparable to thermal effects. The case of the D″ layer is perhaps even more challenging, as it is clearly a region with strong temperature and compositional gradients (e.g., Lay *et al.*, 2004), but also a regionally varying seismic anisotropy (e.g., Maupin *et al.*, 2005; Wookey *et al.*, 2005a) with an overall global signature (e.g., Montagner and Kennett, 1996; Beghein *et al.*, 2006; Panning and Romanowicz, 2006). The inner core has well-known travel time variations that can be modeled to fit various single or double concentric layered anisotropy scenarios. Recent studies (Ishii and Dziewoński, 2002; Beghein and Trampert, 2003) tend to favor a difference in anisotropy between the outermost and innermost inner core; however, they disagree in the magnitude and symmetry of the anisotropy. The most recent study (Calvet *et al.*, 2006) further suggests that data set is too poor to distinguish between several current models. In the mantle and the inner core, there are often differences between studies at the global and regional scales, and differences between one- and three-dimensional global models. The seismic sampling over different radial and lateral length scales using surface and body waves of variable frequency has made reference models very important in the reporting and understanding of complex data sets. Kennett (2006) has shown, for example, that it is difficult to achieve comparable P- and S-wave definition for the whole mantle. Mineral physics can play important role because a representation based on elastic moduli rather than wave speeds would provide a better interpretation in terms of composition, temperature, and anisotropy.

In addressing the basics of elasticity, wave propagation in anisotropic crystals and the nature of the anisotropy polycrystalline aggregate with CPO, the author hopes to have provided some of keys necessary for the interpretation of seismic anisotropy. CPO produced by plastic deformation is the link between deformation history and the seismic anisotropy of the Earth's deep interior. We have seen above that many regions of the mantle (e.g., lower mantle) do not have a pronounced seismic anisotropy. However, from mineral physics we have seen that in the upper mantle olivine has a strong elastic anisotropy, in the transition zone wadsleyite is quite anisotropic, in the lower mantle Mg-perovskite and MgO have inceasing anisotropy with depth, in the D″ layer postperovskite is very anisotropic and the inner-core h.c.p. iron is moderately anisotropic. In addition, if we add minerals from the hydrated mantle in suduction regions, such as the A-phase, hydro-ringwoodite, and brucite, these can be quite anisotropic to exceeding anisotropic in the case of brucite. Potentially, the mineralogy suggests that seismic anisotropy could be present if these minerals have a CPO. Aligned melt inclusions and compositional layers can also produce anisotropy. To understand why there are regions in the deep Earth that have no seismic anisotropy is clearly a challenge for mineral physics, seismology, and geodynamics.

## References


Abramson EH, Brown JM, Slutsky LJ, and Zaug J (1997) The elastic constants of San Carlos olivine to 17 GPa. *Journal of Geophysical Research* 102: 12253–12263.

Adams BL, Wright SL, and Kunze K (1993) Orientation mapping: The emergence of a new microscopy. *Metallurgical Transactions A* 24: 819–831.

Anderson DL (1979) Deep structure of the continents. *Journal of Geophysical Research* 84: 7555–7560.

Anderson OL and Isaak DG (1995) Elastic constants of mantle minerals at high temperature. In: Ahrens TJ (ed.) *Handbook of Physical Constants*, pp. 64–97. Washington, DC: American Geophysical Union special publication.

Andrault D, Fiquet G, Kunz M, Visocekas F, and Häusermann D (1997) The orthorhombic structure of iron: An *in situ* study at high temperature and high pressure. *Science* 278: 831–834.
Antonangelia D, Occellia F, Requardta H, Badro J, Fiquet G, and Krisch M (2004) Elastic anisotropy in textured hcp-iron to 112 GPa from sound wave propagation measurements. *Earth and Planetery Science Letters* 225: 243–251.
Auld BA (1990) *Acoustic Fields and Waves in Solids*, 2nd edn., vol. 1, 425 pp. Malabar, FL: Krieger Publication.
Barnett DM (1972) The precise evaluation of derivatives of the anisotropic elastic Green's functions. *Physica Status Solidi (b)* 49: 741–748.
Barruol G (1993) *Pétrophysique de la croûte inférieure. Rôle de l'Anisotropies Sismiques sur la Réflectivité et Déphasage des ondes S*. Thesis Université Montpellier II. 272pp.
Barruol G and Kern H (1996) P and S waves velocities and shear wave splitting in the lower crustal/upper mantle transition (Ivrea Zone). Experimental and calculated data. *Physics of the Earth and Planetary Interiors* 95: 175–194.
Bass JD (1995) Elastic properties of minerals, melts, and glasses. In: Ahrens TJ (ed.) *Handbook of Physical Constants*, pp. 45–63. Washington, DC: American Geophysical Union special publication.
Bass JD, Liebermann RC, Weidner DJ, and Finch SJ (1981) Elastic properties from acoustic and volume compression experiments. *Physics of the Earth and Planetary Interiors* 25: 140–158.
Beghein C and Trampert J (2003) Robust normal mode constraints on the inner-core anisotropy from model space search. *Science* 299: 552–555.
Beghein C, Trampert J, and van Heijst HJ (2006) Radial anisotropy in seismic reference models of the mantle. *Journal of Geophysical Research* 111: B02303 (doi:10.1029/2005JB003728).
Bell DR, Rossman GR, Maldener A, Endisch D, and Rauch F (2003) Hydroxide in olivine: A quantitative determination of the absolute amount and calibration of the IR spectrum. *Journal of Geophysical Research* 108 (doi:10.1029/2001JB000679).
Ben Ismail W and Mainprice D (1998) An olivine fabric database: An overview of upper mantle fabrics and seismic anisotropy. *Tectonophysics* 296: 145–157.
Beran MJ, Mason TA, Adams BL, and Olsen T (1996) Bounding elastic constants of an orthotropic polycrystal using mesurements of the microstructure. *Journal of Mechanics Physics Solids* 44: 1543–1563.
Berryman JG (2000) Seismic velocity decrement ratios for regions of partial melt in the lower mantle. *Geophysical Research Letters* 27: 421–424.
Bergman MI (1997) Measurements of elastic anisotropy due to solidification texturing and the implications for the Earth's inner core. *Nature* 389: 60–63.
Bjarnason IT, Silver PG, Rümpker G, and Solomon SC (2002) Shear wave splitting across the Iceland hot spot: Results from the ICEMELT experiment. *Journal of Geophysical Research* 107(B12): 2382 (doi:10.1029/2001JB000916).
Blackman DK and Kendall J-M (1997) Sensitivity of teleseismic body waves to mineral texture and melt in the mantle beneath a mid-ocean ridge. *Philosophical Transactions of the Royal Society of London A* 355: 217–231.
Blackman DK, Kendall J-M, Dawson P, Wenk H-R, Boyce D, and Phipps MJ (1996) Teleseismic imaging of subaxial flow at mid-ocean ridges: Travel-time effects of anisotropic mineral texture in the mantle. *Geophysical Journal International* 127: 415–426.
Blackman DK and Kendall J-M (2002) Seismic anisotropy in the upper mantle, 2, Predictions for current plate boundary flow models. *Geochemistry Geophysics Geosystems* 3(9): 8602 (doi:10.1029/2001GC000247).
Birch F (1940) The alpha–gamma transformation of iron at high pressure, and the problem of the Earth's magnetism. *American Journal of Science* 235: 192–211.
Birch F (1952) Elasticity and constitution of the Earth's interior. *Journal of Geophysical Research* 57: 227–286.
Bolfan-Casanova N (2005) Water in the Eath's mantle. *Mineralogical Magazine* 63(3): 229–257.
Boudier F and Nicolas A (1995) Nature of the Moho transition zone in the Oman ophiolite. *Journal of Petrology* 36: 777–796.
Boyd FR (1973) A pyroxene geotherm. *Geochemica etCosmochimica Acta* 37: 2533–2546.
Bozhilov KN, Green HW, II, and Dobrzhinetskaya L (1999) Clinoenstatite in the Alpe Arami periodotite: Additional evidence for very high-pressure. *Science* 284: 128–132.
Buffett BA and Wenk H-R (2001) Texturing of the Earth's inner core by Maxwell stresses. *Nature* 413: 60–63.
Bunge HJ (1982) *Texture Analysis in Materials Sciences*, 593 pp. London: Buttleworth.
Brown JM and Shankland TJ (1981) Thermodynamic parameters in the Earth as determined from seismic profiles. *Geophysical Journal of the Royal Astronomical Society* 66: 579–596.
Brugger K (1965) Pure modes for elastic waves in crystals. *Journal of Applied Physics* 36: 759–768.
Bruner WM (1976) Comments on Seismic velocities in dry and saturated cracked solids. *Journal of Geophysical Research* 81: 2573–2576.
Calvet M, Chevrot S, and Souriau A (2006) P-wave propagation in transversely isotropic media II. Application to inner core anisotropy: Effects of data averaging, parametrization and *a priori* information. *Physics of the Earth and Planetary Interiors* 156: 21–40.
Červený V (1972) Seismic rays and ray intensities in inhomogeneous anisotropic media. *Geophysical Journal of the Royal Astronomical Society* 29: 1–13.
Carpenter MA (2006) Elastic properties of minerals and the influence of phase transitions. *American Mineralogist* 91: 229–246.
Carrez P, Cordier P, Mainprice D, and Tommasi A (2006) Slip systems and plastic shear anisotropy in Mg2SiO4 Ringwoodite: Insights from numerical modelling. *European Journal of Mineralogy* 18: 149–160.
Chai M, Brown JM, and Slutsky LJ (1977) The elastic constants of a pyrope–grossular–almandine garnet to 20 GPa. *Geophysical Research Letters* 24: 523–526.
Chai M, Brown JM, and Slutsky LJ (1997) The elastic constants of an aluminous orthopyroxene to 12.5 GPa. *Journal of Geophysical Research* 102: 14779–14785.
Chastel YB, Dawson PR, Wenk H-R, and Bennet K (1993) Anisotropic convection with implications for the upper mantle. *Journal of Geophysical Research* 98: 17757–17771.
Chen G, Li B, and Liebermann RC (1996) Selected elastic moduli of single-crystal olivines from ultrasonic experiments to mantle pressures. *Science* 272: 979–980.
Chen G, Liebermann RC, and Weidner DJ (1998) Elasticity of single-crystal MgO to 8 gigapascals and 1600 kelvin. *Science* 280: 1913–1916.
Collins MD and Brown JM (1998) Elasticity of an upper mantle clinopyroxene. *Physics and Chemistry of Minerals* 26: 7–13.
Cordier P, Mainprice D, and Mosenfelder JL (2004a) Mechanical instability near the stishovite - CaCl2 phase transition: Implications for crystal preferred orientations and seismic properties. *European Journal of Mineralogy* 16: 387–399.
Cordier P, Ungàr T, Zsoldos L, and Tichy G (2004b) Dislocation creep in MgSiO3 perovskite at conditions of the Earth's uppermost lower mantle. *Nature* 428: 837–840.

Couvy H, Frost DJ, Heidelbach F, *et al.* (2004) Shear deformation experiments of forsterite at 11 GPa - 1400°C in the multianvil apparatus. *European Journal of Mineralogy* 16: 877–889.
Crampin S (1984) Effective anisotropic elastic constants for wave propagation through cracked solids. *Geophysical Journal of the Royal Astronomical Society* 76: 135–145.
Creager KC (1992) Anisotropy of the inner core from differential travel times of the phases PKP and PKIKP. *Nature* 356: 309–314.
Creager KC (1997) Inner core rotation rate from small-scale heterogeneity and time-varying travel times. *Science* 278: 1284–1288.
Creager KC (1999) Large-scale variations in inner-core anisotropy. *Journal of Geophysical Research* 104: 23127–23139.
Creager KC (2000) Inner core anisotropy and rotation. In: Karato S-I, Stixrude L, Liebermann R, Masters G, and Forte A (eds.) *Geophysical Monograph Series, 117: Mineral Physics and Seismic Tomography from the Atomic to the Global Scale*, pp. 89–114. Washington, DC: American Geophysical Union.
Crosson RS and Lin JW (1971) Voigt and Reuss prediction of anisotropic elasticity of dunite. *Journal of Geophysical Research* 76: 570–578.
Currie CA, Cassidy JF, Hyndman R, and Bostock MG (2004) Shear wave anisotropy beneath the Cascadia subduction zone and Western North America craton. *Geophysical Journal International* 157: 341–353.
Da Silva CRS, Karki BB, Strixrude L, and Wentzcovitch RM (1999) *Ab initio* study of the elastic behavior of MgSiO3 ilmenite at high pressure. *Geophysical Research Letters* 26: 943–946.
Davies GF (1974) Effective elastic moduli under hydrostatic stress I, Quasi-harmonic theory. *Journal of Physics and Chemistry of Solids* 35: 1513–1520.
Demouchy S, Jacobsen SD, Gaillard F, and Stern CR (2006) Rapid magma ascent recorded by water diffusion profiles in mantle olivine. *Geology* 34: 429–432 (doi: 10.1130/G22386.1).
Deschamps F and Trampert J (2003) Mantle tomography and its relation to temperature and composition. *Physics of the Earth and Planetetary Interiors* 140: 277–291.
Deuss A and Woodhouse JH (2001) Seismic observations of splitting of the mid-mantle transition zone discontinuity in Earth's mantle. *Science* 294: 354–357.
Deuss A and Woodhouse JH (2002) A systematic search for mantle discontinuities using SS-precursors. *Geophysical Research Letters* 29(8) (doi:10.1029/2002GL014768).
Deuss A, Woodhouse JH, Paulssen H, and Trampert J (2000) The observation of inner core shear waves. *Geophysical Journal International* 142: 67–73.
Doornbos DJ (1974) The anelasticity of the inner core. *Geophysical Journal of the Royal Astronnomical Society* 38: 397–415.
Dubrovinsky LS, Dubrovinskaia NA, and Le Bihan T (2001) Aggregate sound velocities and acoustic Gruneisen parameter of iron up to 300 GPa and 1,200 K. *Proceedings of the National Academy of Sciences USA* 98: 9484–9489.
Duffy TS and Vaughan MT (1988) Elasticity of enstatite and its relationship to crystal structure. *Journal of Geophysical Research* 93: 383–391.
Duffy TS, Zha CS, Downs RT, Mao HK, and Hemley RJ (1995) Elasticity of forsterite to 16 GPa and the composition of the upper mantle. *Nature* 378: 170–173.
Durek JJ and Romanowicz B (1999) Inner core anisotropy inferred by direct inversion of normal mode spectra. *Geophysical Journal International* 139: 599–622.
Durinck J, Legris A, and Cordier P (2005a) Influence of crystal chemistry on ideal plastic shear anisotropy in forsterite: First principle calculations. *American Mineralologist* 90: 1072–1077.
Durinck J, Legris A, and Cordier P (2005b) Pressure sensitivity of olivine slip systems: First-principle calculations of generalised stacking faults. *Physics and Chemistry of Minerals* 32: 646–654.
Dziewoński AM and Anderson DL (1981) Prelininary reference Earth model. *Physics of the Earth and Planetary Interiors* 25: 297–356.
Eshelby JD (1957) The determination of the elastic field of a ellipsoidal inclusion, and related problems. *Proceedings of the Royal Society of London, A* 241: 376–396.
Every AG (1980) General closed-form expressions for acoustic waves in elastically anisotropic solids. *Physical Review B* 22: 1746–1760.
Fedorov FI (1968) *Theory of Elastic Waves in Crystals*, 375 pp. New York: Penum Press.
Fei Y (1995) Thermal expansion. In: Ahrens TJ (ed.) *Minerals Physics and Crystallography: A Handbook of Physical Constants*, pp. 29–44. Washington, DC: American Geophysical Union.
Fiquet G, Badro G, Guyot F, Requardt H, and Krisch M (2001) Sound velocities in iron to 110 Gigapascals. *Science* 292: 468–471.
Fiquet G, Badro J, Guyot F, *et al.* (2004) Application of inelastic X-ray scattering to measurements of acoustic wave velocities in geophysical materials at very high pressure. *Physics of the Earth and Planetery Interiors* 143–144: 5–18.
Fischer KM, Fouch MJ, Wiens DA, and Boettcher MS (1998) Anisotropy and flow in Pacific subduction zone back-arcs. *Pure and Applied Geophysics* 151: 463–475.
Flanagan MP and Shearer PM (1998) Global mapping of topography on transition zone velocity discontinuties by stacking SS precursors. *Journal of Geophysical Research* 103: 2673–2692.
Forsyth DW, Webb SC, Dorman LM, and Shen Y (1998) Phase velocities of Rayleigh waves in the MELT experiment of the East Pacific Rise. *Science* 280: 1235–1238.
Fouch MJ and Rondenay S (2006) Seismic anisotropy beneath stable continental interiors. *Physics of the Earth and Planetary Interiors* 158: 292–320.
Frisillo AL and Barsch GR (1972) Measurement of single-crystal elastic constants of bronzite as a function of pressure and temperature. *Journal of Geophysical Research* 77: 6360–6384.
Fukao Y, Widiyantoro S, and Obayashi M (2001) Stagnant slabs in the upper and lower mantle transition region. *Reviews of Geophysics* 39: 291–323.
Garnero EJ, Revenaugh JS, Williams Q, Lay T, and Kellogg LH (1998) Ultralow velocity zone at the core–mantle boundary. In: Gurnis M, Wysession ME, Knittle E, and Buffett BA (eds.) *The Core–Mantle Boundary Region*, pp. 319–334. Washington, DC: American Geophysical Union.
Garnero EJ (2000) Heterogeneity of the lowermost mantle. *Annual Review of Earth and Planetary Sciences* 28: 509–537.
Garnero EJ, Maupin V, Lay T, and Fouch MJ (2004) Variable azimuthal anisotropy in Earth's lowermost mantle. *Science* 306: 259–260.
Gaherty JB and Jordan TH (1995) Lehmann discontinuity as the base of an anisotropic layer beneath continents. *Science* 268: 1468–1471.
Gannarelli CMS, Alfè D, and Gillan MJ (2003) The particle-in-cell model for *ab initio* thermodynamics: Implications for the elastic anisotropy of the Earth's inner core. *Physics of the Earth and Planetary Interiors* 139: 243–253.
Gannarelli CMS, Alfè D, and Gillan MJ (2005) The axial ratio of hcp iron at the conditions of the Earth's inner core. *Physics of the Earth and Planetary Interiors* 152: 67–77.

Garcia R (2002) Seismological and mineralogical constraints on the inner core fabric. *Geophysical Research Letters* 29: 1958 (doi:10.1029/2002GL015268).
Garcia R and Souriau A (2000) Inner core anisotropy and heterogeneity level. *Geophysical Research Letters* 27: 3121–3124.
Garcia R and Souriau A (2001) Correction to: Inner core anisotropy and heterogeneity level. *Geophysical Research Letters* 28: 85–86.
Gassmann F (1951) Uber die elastizitat poroser medien. *Vier. der Natur Gesellschaft* 96: 1–23.
Glatzmaier GA and Roberts PH (1995) A three dimensional convective dynamo solution with rotating and finitely conducting inner core and mantle. *Physics of the Earth and Planetetary Intereriors* 91: 63–75.
Glatzmaier GA and Roberts PH (1996) Rotation and magnetism of Earth's inner core. *Science* 274: 1887–1891.
Gubbins D (1981) Rotation of the inner core. *Journal of Geophysical Research* 86: 11695–11699.
Haggerty SE and Sautter V (1990) Ultra deep (>300 km) ultramafic, upper mantle xenoliths. *Science* 248: 993–996.
Hammond WC and Humphreys ED (2000) Upper mantle seismic wave velocity: Effects of realistic partial melt geometries. *Journal of Geophysical Research* 105: 10975–10986.
Hammond WC and Toomey DR (2003) Seismic velocity anisotropy and heterogeneity beneath the Mantle Electromagnetic and Tomography Experiment (MELT) region of the East Pacific Rise from analysis of P and S body waves. *Journal of Geophysicsl Research* 108(B4): 2176 (doi:10.1029/2002JB001789).
Harte B and Harris JW (1993) Lower mantle inclusions from diamonds. *Terra Nova* 5 (supplement 1): 101.
Heinemann S, Sharp TG, Sharp SF, and Rubie DC (1997) The cubic–teragonal phase transition in the system majorite (Mg4Si4O12) – pyrope (Mg3Al2Si3O12) and garnet symmetry in the Earth's transition zone. *Physics and Chemistry of Minerals* 24: 206–221.
Helffrich GR and Wood BJ (1996) 410 km discontinuity sharpness and the form of the olivine $\alpha$–$\beta$ phase diagram: Resolution of apparent seismic contradictions. *Geophysical Journal International* 126: F7–F12.
Hess HH (1964) Seismic anisotropy of the uppermost mantle under oceans. *Nature* 203: 629–631.
Hill R (1952) The elastic behaviour of a crystalline aggregate. *Proceedings of the Physics Society of London Series. A* 65: 349–354.
Hill R (1965) A self consistent mechanics of composite materials. *Journal of Mechanics and Physics of Solids* 13: 213–222.
Hirth G and Kohlstedt DL (1996) Water in the oceanic upper mantle: Implications for rheology, melt extration and the evolution of the lithosphere. *Earth and Planetetary Science Letters* 144: 93–108.
Holtzman B, Kohlstedt DL, Zimmerman ME, Heidelbach F, Hiraga T, and Hustoft J (2003) Melt segregation and strain partitioning: Implications for seismic anisotropy and mantle flow. *Science* 301: 1227–1230.
Hornby BE, Schwartz LM, and Hudson JA (1994) Anisotropic effective-medium modelling of the elastic properties of shales. *Geophysics* 59: 1570–1583.
Iitaka T, Hirose K, Kawamura K, and Murakami M (2004) The elasticity of the MgSiO3 postperovskite phase in the Earth's lowermost mantle. *Nature* 430: 442–445.
Inoue T, Weidner DJ, Northrup PA, and Parise JB (1998) Elastic properties of hydrous ringwoodite ($\gamma$-phase) in Mg2SiO4. *Earth and Planetary Science Letters* 160: 107–113.
Irifune T, Ringwood AE, and Hibberson WO (1994) Subduction of continental crust and terrigenous and pelagic sediments: An experimental study. *Earth and Planetary Science Letters* 126: 351–368.
Isaak DG (1992) High-temperature elasticity of iron-bearing olivine. *Journal of Geophysical Research* 97: 1871–1885.
Isaak DG (2001) Elastic properties of minerals and planetary objects. In: Levy M, Bass H, and Stern R (eds.) *Handbook of Elastic Properties of Solids, Liquids, and GasesVolume III: Elastic Properties of Solids: Biological and Organic Materials, Earth and Marine Sciences*, pp. 325–376. New York: Academic Press.
Isaak DG, Anderson OL, Goto T, and Suzuki I (1989a) Elasticity of single-crystal forsterite measured to 1,700 K. *Journal of Geophysical Research* 94: 5895–5906.
Isaak DG, Anderson OL, and Goto T (1989b) Measured elastic moduli of single-crystal MgO up to 1800 K. *Physics and Chemistry of Minerals* 16: 704–713.
Isaak DG, Cohen RE, and Mehl MJ (1990) Calculated elastic and thermal properties of MgO at high pressures and temperatures. *Journal of Geophysical Research* 95: 7055–7067.
Isaak DG and Ohno I (2003) Elastic constants of chrome-diopside: Application of resonant ultrasound spectroscopy to monoclinic single-crystals. *Physics and Chemistry of Minerals* 30: 430–439.
Isaak DG, Ohno I, and Lee PC (2005) The elastic constants of monoclinic single-crystal chrome-diopside to 1,300 K. *Physics and Chemistry of Minerals* 32: (doi:10.1007/s00269-005-0047-9).
Ishii M, Dziewoński AM, Tromp J, and Ekström G (2002b) Joint inversion of normal mode and body wave data for inner core anisotropy: 2. Possible complexities. *Journal of Geophysical Research* 107: (doi:10.1029/2001JB000713).
Ishii M and Dziewoński AM (2002) The innermost inner core of the Earth: Evidence for a change in anisotropic behavior at the radius of about 300 km. *Proceedings of the National Academy of Sciences USA* 99: 14026–14030.
Ishii M and Dziewoński AM (2003) Distinct seismic anisotropy at the centre of the Earth. *Physics of the Earth and Planetary Interiors* 140: 203–217.
Ishii M, Tromp J, Dziewoński AM, and Ekström G (2002a) Joint inversion of normal mode and body wave data for inner core anisotropy: 1. Laterally homogeneous anisotropy. *Journal of Geophysical Research* 107: (doi:10.1029/2001JB000712).
Ito E and Katsura T (1989) A temperature profile of the mantle transition zone. *Geophyical Research Letters* 16: 425–428.
Jackson I and Niesler H (1982) The elasticity of periclase to 3 GPa and some geophysical implications. In: Akimoto S and Manghnani MH (eds.) *High-Pressure Research in Geophysics*, pp. 93–113. Japan: Center for Academic Publications.
Jackson I, Fitz GJD, Faul UH, and Tan BH (2002) Grainsize sensitive seismic wave attenuation in polycrystalline olivine. *Journal of Geophysical Research* 107(B12): 2360 (doi:10.1029/2001JB001225).
Jackson JM, Sinogeikin SV, Bass JD, and Weidner DJ (2000) Sound velocities and elastic properties of $\gamma$-Mg2SiO4 to 873K by Brillouin spectroscopy. *American Minerologist* 85: 296–303.
Jacobsen SD, Reichmann HJ, Spetzler HA, *et al.* (2002) Structure and elasticity of single-crystal (Mg,Fe)O and a new method of generating shear waves for gigahertz ultrasonic interferometry. *Journal of Geophysical Research* 107: 2037 (doi:10.1029/2001JB000490).
Jacobsen SD, Smyth JR, Spetzler H, Holl CM, and Frost DJ (2004) Sound velocities and elastic constants of ironbearing hydrous ringwoodite. *Physics of the Earth and Planetary Interiors* 143–144: 47–56.

Jacobsen SD, Reichmann HJ, Kantor A, and Spetzler HA (2005) A gigahertz ultrasonic interferometer for the diamond anvil cell and high-pressure elasticity of some iron-oxide minerals. In: Chen J, Wang Y, Duffy TS, Shen G, and Dobrzhinetskaya LF (eds.) *Advances in High-Pressure Technology for Geophysical Applications*, pp. 25–48. Amsterdam: Elsevier.

Jacobsen SD (2006) Effect of water on the equation of state of nominally anhydrous minerals. *Reviews in Mineralogy and Geochemistry* 62: 321–342.

Jacobsen SD and Smyth JR (2006) Effect of water on the sound velocities of ringwoodite in the transition zone. In: Jacobsen SD and van der Lee S (eds.) *Geophysical Monograph Series, 168: Earth's Deep Water Cycle*, pp. 131–145. Washington, DC: American Geophysical Union.

Jeanloz R and Wenk H-R (1988) Convection and anisotropy of the inner core. *Geophysical Research Letters* 15: 72–75.

Jeffreys H (1926) The rigidity of the Earth's central core. *Monthly Notices of the Royal Astronomical Society Geophysics* 371–383.

Jiang F, Speziale S, and Duffy TS (2006) Single-crystal elasticity of brucite, Mg(OH)2, to 15 GPa by Brillouin scattering. *American Mineralogist* 91: 1893–1900.

Jousselin D and Mainprice D (1998) Melt topology and seismic anisotropy in mantle peridotites of the Oman ophiolite. *Earth and Planetary Science Letters* 167: 553–568.

Julian BR, Davies D, and Sheppard RM (1972) PKJKP. *Nature* 235: 317–318.

Jung H and Karato S-I (2001) Water-induced fabric transitions in olivine. *Science* 293: 1460–1463.

Karato S-I (1992) On the Lehmann discontinuity. *Geophysical Research Letters* 19: 2255–2258.

Karato S-I (1993) Inner core anisotropy due to magnetic field-induced preferred orientation of iron. *Science* 262: 1708–1711.

Karato S-I (1998) Seismic anisotropy in the deep mantle, boundary layers and the geometry of mantle convection. *Pure and Applied Geophysics* 151: 565–587.

Karato S-I (1999) Seismic anisotropy of Earth's inner core caused by Maxwell stress-induced flow. *Nature* 402: 871–873.

Karato S-I (2006) Remote Sensing of hydrogen in Earth's mantle. *Reviews in Mineralogy and Geochemistry* 62: 343–375.

Karato S-I, Dupas-Bruzek C, and Rubie DC (1998) Plastic deformation of silicate spinel under the transition zone conditions of the Earth's mantle. *Nature* 395: 266–269.

Karato S-I and Jung H (1998) Water, partial melting and the origin of the seismic low velocity and high attenuation zone in the upper mantle. *Earth and Planetetary Science Letters* 157: 193–207.

Karato S-I, Zhang S, and Wenk H-R (1995) Superplastic in Earth's lower mantle: Evidence from seismic anisotropy and rock physics. *Science* 270: 458–461.

Karki BB, Stixrude L, and Crain J (1997b) *Ab initio* elasticity of three high-pressure polymorphs of silica. *Geophysical Research Letters* 24: 3269–3272.

Karki BB, Stixrude L, Clark SJ, Warren MC, Ackland GJ, and Crain J (1997a) Elastic properties of orthorhombic MgSiO3 pervoskite at lower mantle pressures. *American Mineralogist* 82: 635–638.

Karki BB, Stixrude L, Clark SJ, Warren MC, Ackland GJ, and Crain J (1997c) Structure and elasticity of MgO at high pressure. *American Mineralogist* 82: 52–61.

Karki BB, Wentzcovitch RM, de Gironcoli M, and Baroni S (1999) First principles determination elastic anisotropy and wave velocities of MgO at lower mantle conditions. *Science* 286: 1705–1707.

Karki BB, Wentzcovitch RM, de Gironcoli M, and Baroni S (2000) High pressure lattice dynamics and thermoelasticity of MgO. *Physical Review B1* 61: 8793–8800.

Karki BB, Strixrude L, and Wentzocovitch RM (2001) High-pressure elastic properties of major materials of Earth's mantle from from first principles. *Review of Geophysics* 39: 507–534.

Katayama I, Jung H, and Karato S-I (2004) A new type of olivine fabric from deformation experiments at modest water content and low stress. *Geology* 32: 1045–1048.

Katayama I and Karato S-I (2006) Effect of temperature on the B- to C-type olivine fabric transition and implication for flow pattern in subduction zones. *Physics of the Earth and Planetary Interiors* 157: 33–45.

Kawakatsu H and Niu F (1994) Seismic evidence for a 920 km discontinuity in the mantle. *Nature* 371: 301–305.

Kendall J-M (1994) Teleseismic arrivals at a mid-ocean ridge: Effects of mantle melt and anisotropy. *Geophysical Research Letters* 21: 301–304.

Kendall J-M (2000) Seismic anisotropy in the boundary layers of the mantle. In: Karato S, Forte AM, Liebermann RC, Masters G, and Stixrude L (eds.) *Earth's Deep Interior: Mineral Physics and Tomography from the Atomic to the Global Scale*, pp. 133–159. Washington, DC: American Geophysical Union.

Kendall J-M and Silver PG (1996) Constraints from seismic anisotropy on the nature of the lowermost mantle. *Nature* 381: 409–412.

Kendall J-M and Silver PG (1998) Investigating causes of D'' anisotropy. In: Gurnis M, Wysession M, Knittle E, and Buffet B (eds.) *The Core–Mantle Boundary Region*, pp. 409–412. Washington, D.C: American Geophysical Union.

Kendall J-M, Stuart GW, Ebinger CJ, Bastow ID, and Keir D (2004) Magma-assisted rifting in Ethiopia. *Nature* 433: 146–148 (doi:10.1038/nature03161).

Kennett BLN (2006) On seismological reference models and the perceived nature of heterogeneity. *Physics of the Earth and Planetary Interiors* 159: 129–139.

Kesson SE and Fitz GJD (1991) Partitioning of MgO, FeO, NiO, MnO and Cr2O3 between magnesian silicate perovskite and magnesiowüstite: Implications for the inclusions in diamond and the composition of the lower mantle. *Earth and Planetary Science Letters* 111: 229–240.

Kiefer B, Stixrude L, and Wentzcovitch RM (1997) Calculated elastic constants and anisotropy of Mg2SiO4 spinel at high pressure. *Geophysical Research Letters* 24: 2841–2844.

Kind R, Kosarev GL, Makeyeva LI, and Vinnik LP (1985) Observation of laterally inhomogeneous anisotropy in the continental lithosphere. *Nature* 318: 358–361.

Kingma KJ, Cohen RE, Hemley RJ, and Mao H-K (1995) Transformations of stishovite to a denser phase at lower-mantle pressures. *Nature* 374: 243–245.

Kneller EA, van Keken PE, Karato S-I, and Park J (2005) B-type fabric in the mantle wedge: Insights from high-resolution non-Newtonian subduction zone models. *Earth and Planetary Science Letters* 237: 781–797.

Knittle E (1995) Static compression measurements of equation of state. In: Ahrens TJ (ed.) *Minerals Physics and Crystallography: A Handbook of Physical Constants*, pp. 98–142. Washington, D.C: American Geophysical Union.

Kröner E (1978) Self-consistent scheme and graded disorder in polycrystal elasticity. *Journal of Physics F: Metal Physics* 8: 2261–2267.

Kumazawa M (1969) The elastic constants of single crystal orthopyroxene. *Journal of Geophysical Research* 74: 5973–5980.

Laio A, Bernard S, Chiarotti GL, Scandolo S, and Tosatti E (2000) Physics of iron at Earth's core conditions. *Science* 287: 1027–1030.

Lay T, Garnero EJ, and Williams Q (2004) Partial melting in a thermo–chemical boundary layer at the base of the mantle. *Physics of the Earth and Planetary Interiors* 146: 441–467.

Lehmann I (1936) P'. *Union Geodesique at Geophysique Internationale, Serie A, Travaux Scientifiques* 14: 87–115.

Lehmann I (1959) Velocites of longitudinal waves in the upper part of the Earth's mantle. *Annals of Geophysics* 15: 93–118.

Lehmann I (1961) S and the structure of the upper mantle. *Geophyical Journal of the Royal Astronomical Society* 4: 124–138.

Leven J, Jackson I, and Ringwood AE (1981) Upper mantle seismic anisotropy and lithosphere decoupling. *Nature* 289: 234–239.

Levien L, Weidner DJ, and Prewitt CT (1979) Elasticity of diopside. *Physics and Chemistry of Minerals* 4: 105–113.

Li B, Kung J, and Liebermann RC (2004) Modern techniques in measuring elasticity of Earth materials at high pressure and high temperature using ultrasonic interferometry in conjunction with synchrotron X-radiation in multi-anvil apparatus. *Physics of the Earth and Planetary Interiors* 143–144: 559–574.

Li L, Weidner DJ, Brodholt J, Alfé D, and Price GD (2006a) Elasticity of $Mg_2SiO_4$ ringwoodite at mantle conditions. *Physics of the Earth and Planetary Interiors* 157: 181–187.

Li L, Weidner DJ, Brodholt J, Alfé D, Price GD, Caracas R, and Wentzcoitch R (2006b) Elasticity of CaSiO3 perovskite at high pressure and high temperature. *Physics of the Earth and Planetary Interiors* 155: 249–259.

Liebermann RC and Li B (1998) Elasticity at high pressures and temperatures. In: Hemley R (ed.) *Ultrahigh-Pressure Mineralogy: Physics and Chemistry of the Earth's Deep Interior*, pp. 459–492. Washington, DC: Mineralogical Society of America.

Lin J-F, Sturhahn W, Zhao J, Shen G, Mao H-K, and Hemley RJ (2005) Sound Velocities of hot dense iron: Birch's law revisited. *Science* 308: 1892–1894.

Love AEH (1927) *A Treatise on the Mathematical Theory of Elasticity*. New York: Dover Publications.

McLaughlin RA (1977) A study of the differential scheme for composite materials. *International Journal of Engineering Science* 15: 237–244.

McNamara AK, van Keken PE, and Karato S-I (2003) Development of finite strain in the convecting lower mantle and its implications for seismic anisotropy. *Journal of Geophysical Research* 108(B5): 2230 (doi:10.1029/2002JB001970).

Mainprice D (1990) A FORTRAN program to calculate seismic anisotropy from the lattice preferred orientation of minerals. *Computers and Geosciences* 16: 385–393.

Mainprice D (1997) Modelling anisotropic seismic properties of partially molten rocks found at mid-ocean ridges. *Tectonophysics* 279: 161–179.

Mainprice D, Barruol G, and Ben Ismaïl W (2000) The anisotropy of the Earth's mantle: From single crystal to polycrystal. In: Karato S-I, Stixrude L, Liebermann R, Masters G, and Forte A (eds.) *Geophysical Monograph Series, 117: Mineral Physics and Seismic Tomography from the Atomic to the Global Scale*, pp. 237–264. Washington, DC: American Geophysical Union.

Mainprice D and Humbert M (1994) Methods of calculating petrophysical properties from lattice preferred orientation data. *Surveys in Geophysics 15* Special issue 'Seismic properties of crustal and mantle rocks: laboratory measurements and theorietical calculations' 575–592.

Mainprice D, Humbert M, and Wagner F (1990) Phase transformations and inherited lattice preferred orientation: Implications for seismic properties. *Tectonophysics* 180: 213–228.

Mainprice D and Nicolas A (1989) Development of shape and lattice preferred orientations: Application to the seismic anisotropy of the lower crust. *Journal of Structural Geology* 11(1/2): 175–189.

Mainprice D, Tommasi A, Couvy H, Cordier P, and Frost DJ (2005) Pressure sensitivity of olivine slip systems: Implications for the interpretation of seismic anisotropy of the Earth's upper mantle. *Nature* 433: 731–733.

Mao H-K, Shu J, Shen G, Hemley RJ, Li B, and Singh AK (1998) Elasticity and rheology of iron above 220 GPa and the nature of Earth's inner core. *Nature* 396: 741–743 (Correction, 1999 *Nature* 399: 280).

Mao HK, Xu J, Struzhkin VV, *et al.* (2001) Phonon density of states of iron up to 153 gigapascals. *Science* 292: 914–916.

Mason TA and Adams BL (1999) Use of microstructural statistics in predicting polycrystalline material properties. *Metallurgical Transations A* 30: 969–979.

Masters G and Gilbert F (1981) Structure of the inner core inferred from observations of its spheroidal shear modes. *Geophysical Research Letters* 8: 569–571.

Matsui M and Busing WR (1984) Calculation of the elastic constants and high-pressure properties of diopside, CaMgSi2O6. *American Mineralogist* 69: 1090–1095.

Matthies S and Humbert M (1993) The realization of the concept of a geometric mean for calculating physical constants of polycrystalline materials. *Physica Status Solidi (b)* 177: K47–K50.

Mavko GM (1980) Velocity and attenuation in partially molten rocks. *Journal of Geophysical Research* 85: 5173–5189.

Maupin V, Garnero EJ, Lay T, and Fouch MJ (2005) Azimuthal anisotropy in the D'' layer beneath the Caribbean. *Journal of Geophysical Research* 110: B08301 (doi:10.1029/2004JB003506).

Mégnin C and Romanowicz B (2000) The three-dimensional shear velocity structure of the mantle from the inversion of body, surface, and higher-mode waveforms. *Geophysical Journal International* 143: 709–728.

Mehl L, Hacker BR, Hirth G, and Kelemen PB (2003) Arc-parallel flow within the mantle wedge: Evidence from the accreted Talkeetna arc, South Central Alaska. *Journal of Geophysical Research* 108(B8): 2375 (doi:10.1029/2002JB002233).

MELT Seismic Team (1998) Imaging the deep seismic structure beneath a midocean ridge: The MELT experiment. *Science* 280: 1215–1218.

Mensch T and Rasolofosaon P (1997) Elastic-wave velocities in anisotropic media of arbitary symmetry – generalization of Thomsen's parameters $\varepsilon$, $\delta$ and $\gamma$. *Geophysical Journal International* 128: 43–64.

Merkel S, Kubo A, Miyagi L, Speziale S, Duffy TS, Mao H-K, and Wenk H-R (2006a) Plastic deformation of $MgGeO_3$ post-perovskite atlower mantle pressures. *Science* 311: 644–646.

Merkel S, Miyajima N, Antonangeli D, Fiquet G, and Yagi T (2006b) Lattice preferred orientation and stress in polycrystalline hcp-Co plastically deformed under high pressure. *Journal of Applied Physics* 100: 023510 (doi:10.1063/1.2214224).

Merkel S, Shu J, Gillet H-K, Mao H, and Hemley RJ (2005) X-ray diffraction study of the single-crystal elastic moduli of $\varepsilon$-Fe up to 30 GPa. *Journal of Geophysical Research* 110: B05201 (doi:10.1029/2004JB003197).

Mercier J-C (1980) Single-pyroxene thermobarometry. *Tectonophysics* 70: 1–37.

Mercier J-C (1985) Olivine and pyroxenes. In: Wenk HR (ed.) *Preferred Orientation in Deformed Metals and Rocks: An Introduction to Modern Texture Analysis*, pp. 407–430. Orlando, FL: Academic Press.

Michibayashi K, Abe N, Okamoto A, Satsukawa T, and Michikura K (2006) Seismic anisotropy in the uppermost mantle, back-arc region of the northeast Japan arc:

Petrophysical analyses of Ichinomegata peridotite xenoliths. *Geophysical Research Letters* 33: L10312 (doi:10.1029/2006GL025812).
Mizukami T, Simon W, and Yamamoto J (2004) Natural examples of olivine lattice preferred orientation patterns with a flow-normal a-axis maximum. *Nature* 427: 432–436.
Montagner J-P (1994a) What can seismology tell us about mantle convection ? *Reviews of Geophysics* 32: 115–137.
Montagner J-P (1994b) Where can seismic anisotropy be detected in the Earth's mantle ? In boundary layers. *Pure and Applied Geophysics* 151: 223–256.
Montagner J-P (1998) Where can seismic anisotropy be detected in the Earth's mantle? In boundary layers. . .. *Pure and Applied Geophysics* 151: 223–256.
Montagner J-P and Anderson DL (1989) Contraints on elastic combinations inferred from petrological models. *Physics of the Earth and Planetary Interiors* 54: 82–105.
Montagner J-P and Kennett BLN (1996) How to reconcile body-wave and normal-mode reference Earth models. *Geophysical Journal International* 125: 229–248.
Montagner J-P and Tanimoto T (1990) Global anisotropy in the upper mantle inferred from the regionalization of phase velocities. *Journal of Geophysical Research* 95: 4797–4819.
Moore RO and Gurney JJ (1985) Pyroxene solid solution in garnets included in diamond. *Nature* 335: 784–789.
Morelli A, Dziewoński AM, and Woodhouse JH (1986) Anisotropy of the inner core inferred from PKIKP travel times. *Geophysical Research Letters* 13: 1545–1548.
Mura T (1987) *Micromechanics of Defects in Solids*. Dordrecht, The Netherlands: Martinus Nijhoff.
Musgrave MJP (2003) *Crystal Acoustics – Introduction to the Study of Elastic Waves and Vibrations in Crystals*, 621 pp. New York: Acoustical Society of America.
Murakami M, Hirose K, Kawamura K, Sata N, and Ohishi Y (2004) Post-perovskite phase transition in MgSiO3. *Science* 304: 855–858.
Neighbours JR and Schacher GE (1967) Determination of elastic constants from sound-velocity measurements in crystals of general symmetry. *Journal of Applied Physics* 38: 5366–5375.
Nakajima J and Hasegawa A (2005) Shear-wave polarization anisotropy and subduction-induced flow in the mantle wedge of northeastern Japan. *Earth and Planetary Science Letters* 225: 365–377.
Nataf HC, Nakanishi I, and Anderson DL (1984) Anisotropy and shear velocity heterogeneities in the upper mantle. *Geophysical Research Letters* 11(2): 109–112.
Nataf HC, Nakanishi I, and Anderson DL (1986) Measurements of mantle wave velocities and inversion for lateral inhomogeneities and anisotropy. *Journal of Geophysical Research* 91(B7): 7261–7307.
Nataf H and Houard S (1993) Seismic discontinuity at the top of D: A world-wide feature? *Geophysical Research Letters* 20: 2371–2374.
Nicolas A and Boudier F (1995) Mapping mantle diapirs and oceanic crust segments in Oman ophiolites. *Journal of Geophysical Research* 100: 6179–6197.
Nicolas A, Boudier F, and Boullier AM (1973) Mechanism of flow in naturally and experimentally deformed peridotites. *American Journal of Science* 273: 853–876.
Nicolas A and Christensen NI (1987) Formation of anisotropy in upper mantle peridotites; a review. In: Fuchs F and Froidevaux C (eds.) *Geodynamics Series, Vol. 16: Composition, Structure and Dynamics of the Lithosphere–Asthenosphere System*, pp. 111–123. Washington, DC: American Geophysical Union.
Nye JF (1957) *Physical Properties of Crystals – Their Representation by Tensors And Matrices*. Oxford: Oxford University Press.
Oganov AR, Brodholt JP, and Price GD (2001) The elastic constants of MgSiO3 perovskite at pressures and temperatures of the Earth's mantle. *Nature* 411: 934–937.
Oganov AR and Ono S (2004) Theoretical and experimental evidence for a post-perovskite phase of MgSiO3 in Earth's D''layer. *Nature* 430: 445–448.
Okal EA and Cansi Y (1998) Detection of PKJKP at intermediate periods by progressive multichannel correlation. *Earth and Planetary Science Letters* 164: 23–30.
Ono S and Oganov AR (2005) *In situ* observations of phase transition between perovskite and CaIrO3-type phase in MgSiO3 and pyrolitic mantle composition. *Earth and Planetary Science Letters* 236: 914–932.
Pacalo REG and Weidner DJ (1997) Elasticity of majorite, MgSiO3 tetragonal garnet. *Physics of the Earth and Planetary Interiors* 99: 145–154.
Pacalo REG, Weidner DJ, and Gasparik T (1992) Elastic properties of sodium-rich majorite garnet. *Geophysical Research Letteres* 19(18): 1895–1898.
Panning M and Romanowicz B (2006) Three-dimensional radially anisotropic model of shear velocity in the whole mantle. *Geophysical Journal International* 167: 361–379 (doi: 10.1111/j.1365-246X.2006.03100.x).
Paterson MS (1982) The determination of hydroxyl by infrared absorption in quartz, silicate glasses and similar materials. *Bulletin of Mineralogy* 105: 20–29.
Pedersen HA, Bruneton M, Maupin V, and the SVKLAPKO Seismic Tomography Working Group (2006) Lithospheric and sublithospheric anisotropy beneath the Baltic shield from surface-wave array analysis. *Earth and Planetary Science Letters* 244: 590–605.
Perrillat J-P, Ricolleau A, Daniel I, *et al.* (2006) Phase transformations of subducted basaltic crust in the upmost lower mantle. *Physics of the Earth and Planetary Interiors* 157: 139–149.
Phakey P, Dollinger G, and Christie J (1972) Transmission electron microscopy of experimentally deformed olivine crystals. In: Heard HC, Borg IY, Carter NL, and Raleigh CB (eds.) *Geophysics Monograph Series: Flow and Fracture of Rocks*, vol. 16, pp. 117–138. Washington, DC: AGU.
Polet J and Anderson DL (1995) Depth extent of cratons as inferred from tomographic studies. *Geology* 23: 205–208.
Poli S and Schmidt M (2002) Petrology of subducted slabs. *Annual Review of Earth and Planetary Sciences* 30: 207–235.
Poupinet G, Pillet R, and Souriau A (1983) Possible heterogeneity of the Earth's core deduced from PKIKP travel times. *Nature* 305: 204–206.
Poupinet G and Kennett BLN (2004) On the observation of high frequency PKiKP an dits coda in Australia. *Physics of the Earth and Planetary Interiors* 146: 497–511.
Raitt RW, Schor GG, Francis TJG, and Morris GB (1969) Anisotropy of the Pacific upper mantle. *Journal of Geophysical Research* 74: 3095–3109.
Ritsema J and van Heijst H-J (2001) Constraints on the correlation of P and S-wave velocity heterogeneity in the mantle from P, PP, PPP, and PKPab traveltimes. *Geophysical Journal International* 149: 482–489.
Ritsema J, van Heijst H-J, and Woodhouse JH (2004) Global transition zone tomography. *Journal of Geophysical Research* 109: B02302 (doi:10.1029/2003JB002610).
Reuss A (1929) Berechnung der Fliessgrenze von Mischkristallen auf Grund der Plastizitätsbedingung für Einkristalle. *Zeitschrift fur Angewandte Mathematik und Mechanik* 9: 49–58.
Ringwood AE (1991) Phase transitions and their bearing on the constitition and dynamics of the mantle. *Geochimica et Cosmochimica Acta* 55: 2083–2110.

Poirier J-P (1994) Light elements in the Earth's outer core: A critical review. *Physics of the Earth and Planetary Interiors* 85: 319–337.

Russo RM and Silver PG (1994) Trench-parallel flow beneath the Nazca plate from seismic anisotropy. *Science* 263: 1105–1111.

Sanchez-Valle C, Sinogeikin SV, Smyth JR, and Bass JD (2006) Single-crystal elastic properties of dense hydrous magnesium silicate phase A. *Americn Mineralologist* 91: 961–964.

Sautter V, Haggerty SE, and Field S (1991) Ultra deep (>300 km) xenoliths: New petrological evidence from the transition zone. *Science* 252: 827–830.

Sawamoto H, Weidner DJ, Sasaki S, and Kumazawa M (1984) Single-crystal elastic properties of the modified-spinel (beta) phase of magnesium orthosilicate. *Science* 224: 749–751.

Saxena SK, Dubrovinsky LS, and Häggkvist P (1996) X-ray evidence for the new phase of $\beta$-iron at high temperature and high pressure. *Geophysical Research Letters* 23: 2441–2444.

Scott-Smith BH, Danchin RV, Harris JW, and Stracke KJ (1984) Kimberlites near Orrorroo, South Australia. In: Kornprobst J (ed.) *Kimberlites I: Kimberlites and Related Rocks*, pp. 121–142. Amsterdam: Elsevier.

Schmeling H (1985) Numerical models on the influence of partial melt on elastic, anelastic ane electrical properties of rocks. Part I: elasticity and anelasticity. *Physics of the Earth and Planetary Interiors* 41: 34–57.

Sha X and Cohen RE (2006) Thermal effects on lattice strain in e-Fe under pressure. *Physical Review B* 74: (doi:10.1103/PhysRevB.74.064103).

Sharp TG, Bussod GYA, and Katsura T (1994) Microstructures in b-Mg1.8Fe0.2SiO4 experimentally deformed at transition-zone conditions. *Physics of the Earth and Planetary Interiors* 86: 69–83.

Shearer PM (1996) Transition zone velocity gradients and the 520 km discontinuity. *Journal of Geophysical Research* 101: 3053–3066.

Shearer PM and Toy KM (1991) PKP(BC) versus PKP(DF) differential travel times and aspherical structure in the Earth's inner core. *Journal of Geophysical Research* 96: 2233–2247.

Sidorin I, Gurnis M, and Helmberger DV (1999a) Evidence for a ubiquitous seismic discontinuity at the base of the mantle. *Science* 286: 1326–1331.

Sidorin I, Gurnis M, and Helmberger DV (1999b) Dynamics of a phase change at the base of the mantle consistent with seismological observations. *Journal of Geophysical Research* 104: 15005–15023.

Silver PG (1996) Seismic anisotropy beneath the continents: Probing the depths of geoloy. *Annual Review of Earth and Planetary Sciences* 24: 385–432.

Silver PG and Chan W (1988) Implications for continental structure and evolution from seismic anisotropy. *Nature* 335: 34–39.

Silver PG and Chan WW (1991) Shear wave splitting and subcontinental mantle deformation. *Journal of Geophysical Research* 96: 16429–16454.

Singh AK, Mao H-K, Shu J, and Hemley RJ (1998) Estimation of single crystal elastic moduli from polycrystalline X-ray diffraction at high pressure: Applications to FeO and iron. *Physical Review Letters* 80: 2157–2160.

Singh SC, Taylor MAJ, and Montagner J-P (2000) On the presence of liquid in Earth's inner core. *Science* 287: 2471–2474.

Sinogeikin SV, Katsura T, and Bass JD (1998) Sound velocities and elastic properties of Fe-bearing wadsleyite and ringwoodite. *Journal of Geophysical Research* 103: 20819–20825.

Sinogeikin SV and Bass JD (2002) Elasticity of pyrope and majorite–pyrope solid solutions to high temperatures. *Earth and Planetary Science Letters* 203: 549–555.

Sinogeikin SV, Bass JD, and Katsura T (2001) Single-crystal elasticity of $\gamma$-(Mg0.91Fe0.09)2SiO4 to high pressures and to high temperatures. *Geophysical Research Letters* 28: 4335–4338.

Sinogeikin SV, Lakshtanov DL, Nichola JD, and Bass JD (2004) Sound velocity measurements on laser-heated MgO and Al2O3. *Physics of the Earth and Planetary Interiors* 143–144: 575–586.

Sinogeikin SV, Lakshtanov DL, Nichola JD, Jackson JM, and Bass JD (2005) High temperature elasticity measurements on oxides by Brillouin spectroscopy with resistive and IR laser heating. *Journal of European Ceramic Society* 25: 1313–1324.

Solomon SC and Toomey DR (1992) The structure of mid-ocean ridges. *Annual Review of the Earth and Planetary Sciences* 20: 329–364.

Song X (1997) Anisotropy of the Earth's inner core. *Reviews of Geophysics* 35: 297–313.

Song X (2000) Joint inversion for inner core rotation, inner core anisotropy, and mantle heterogeneity. *Journal of Geophysical Research* 105: 7931–7943.

Song X and Helmberger DV (1993) Anisotropy of the Earth's inner core. *Geophysical Research Letters* 20: 2591–2594.

Song X and Helmberger DV (1998) Seismic evidence for an inner core transition zone. *Science* 282: 924–927.

Song X and Richards PG (1996) Seismological evidence for differential rotation of the Earth's inner core. *Nature* 382: 221–224.

Song X and Xu XX (2002) Inner core transition zone and anomalous PKP(DF) waveforms from polar paths. *Geophysical Research Letters* 29(4): (10.1029/2001GL013822).

Souriau A, Roudil P, and Moynot B (1997) Inner core differential rotation: Facts and artefacts. *Geophysical Research Letters* 24: 2103–2106.

Stackhouse S, Brodholt JP, Wookey J, Kendall J-M, and Price GD (2005) The effect of temperature on the seismic anisotropy of the perovskite and post-perovskite polymorphs of MgSiO3. *Earth and Planetary Science Letters* 230: 1–10.

Steenbeck M and Helmis G (1975) Rotation of the Earth's solid core as a possible cause of declination, drift and reversals of the Earth's magnetic field. *Geophysical Journal of the Royal Astronomical Society* 41: 237–244.

Steinle-Neumann G, Stixrude L, Cohen RE, and Gulseren O (2001) Elasticity of iron at the temperature of the Earth's inner core. *Nature* 413: 57–60.

Stevenson DJ (1987) Limits on lateral density and velocity variations in the Earth's outer core. *Geophysical Journal of the Royal Astronomical Society* 88: 311–319.

Stixrude L and Cohen RE (1995) High-pressure elasticity of iron and anisotropy of Earth's inner core. *Science* 267: 1972–1975.

Stixrude L and Lithgow-Bertelloni C (2005a) Mineralogy and elasticity of the oceanic upper mantle: Origin of the low-velocity zone. *Journal of Geophysical Research* 110: B03204 (doi:10.1029/2004JB002965).

Stixrude L and Lithgow-Bertelloni C (2005b) Thermodynamics of mantle minerals – I. Physical properties. *Geophysical Journal International* 162: 610–632.

Su WJ and Dziewoński AM (1995) Inner core anisotropy in three dimensions. *Journal of Geophysical Research* 100: 9831–9852.

Szeto AMK and Smylie DE (1984) The rotation of the Earth's inner core. *Philosophical Transactions of the Royal Society of London, Series A* 313: 171–184.

Takei Y (2002) Effect of pore geometry on Vp/Vs: From equilibrium geometry to crack. *Journal of Geophysical Research* 107(B2): 2043 (doi:10.1029/2001JB000522).
Tanaka S and Hamaguchi H (1997) Degree one heterogeneity and hemispherical variations of anisotropy in the inner core form PKP(BC)–PKP(DF) times. *Journal of Geophysical Research* 102: 2925–2938.
Taylor MAJ and Singh SC (2002) Composition and microstructure of magma bodies from effective medium theory. *Geophysical Journal International* 149: 15–21.
Thomsen L (1986) Weak elastic anisotropy. *Geophysics* 51: 1954–1966.
Thurel E, Douin J, and Cordier P (2003) Plastic deformation of wadsleyite: III. Interpretation of dislocations and slip systems. *Physics Chemistry of Minerals* 30: 271–279.
Tommasi A (1998) Forward modeling of the development of seismic anisotropy in the upper mantle. *Earth and Planetary Science Letters* 160: 1–13.
Tommasi A, Mainprice D, Canova G, and Chastel Y (2000) Viscplastic self-consistent and equilibrium-based modeling of olivine lattice preferred orientations. 1.Implications for the upper mantle seismic anisotropy. *Journal of Geophysical Research* 105: 7893–7908.
Tommasi A, Mainprice D, Cordier P, Thoraval C, and Couvy H (2004) Strain-induced seismic anisotropy of wadsleyite polycrystals: Constraints on flow patterns in the mantle transition zone. *Journal of Geophysical Research* 109(B12405): 1–10.
Tommasi A, Vauchez A, Godard M, and Belley F (2006) Deformation and melt transport in a highly depleted peridotite massif from the Canadian Cordillera: Implications to seismic anisotropy above subduction zones. *Earth and Planetary Science Letters* 252: 245–259.
Toomey DR, Wilcock WSD, Solomon SC, Hammond WC, and Orcutt JA (1998) Mantle seismic structure beneath the MELT region of the East Pacific Rise from P and S tomography. *Science* 280: 1224–1227.
Toomey DR, Wilcock WSD, Conder JA, *et al.* (2002) Asymmetric mantle dynamics in the MELT Region of the East Pacific Rise. *Earth and Planetary Science Letters* 200: 287–295.
Trampert J, Deschamps F, Resovsky J, and Yuen D (2004) Probabilistic tomography maps significant chemical heterogeneities in the lower mantle. *Science* 306: 853–856.
Trampert J and van Heijst HJ (2002) Global azimuthal anisotropy in the transition zone. *Science* 296: 1297–1299.
Trampert J and van der Hilst RD (2005) Towards a quantitative interpretation of global seismic tomography. Earth's deep mantle: Structure, composition, and evolution. *Geophysical Monograph Series* 160: 47–63.
Tromp J (1993) Support for anisotropy of the Earth's inner core. *Nature* 366: 678–681.
Tromp J (1994) Normal mode splitting due to inner core anisotropy. *Geophysical Journal International* 121: 963–968.
Tromp J (2001) Inner-core anisotropy and rotation. *Annual Review of Earth and Planetary Sciences* 29: 47–69.
Tsuchiya T, Tsuchiya J, Umemoto K, and Wentzcovitch RM (2004) Elasticity of MgSiO3-post-perovskite. *Geophysical Research Letters* 31: L14603 (doi:10.1029/2004GL020278).
Ulmer P (2001) Partial melting in the mantle wedge – The role of $H_2O$ on the genesis of mantle-derived 'arc-related' magmas. *Physics of the Earth and Planetary Interiors* 127: 215–232.
Vacher R and Boyer L (1972) A tool for the measurement of elastic and photoelastic constants. *Physical Review B* 6: 639–673.
Vauchez A, Tommasi A, Barruol G, and Maumus J (2000) Upper mantle deformation and seismic anisotropy in continental rifts. *Physics and Chemistry of the Earth, Part A Solid Earth and Geodesy* 25: 111–117.
Vavrycuk V (2003) Parabolic lines and caustics in homogeneous weakly anisotropic solids. *Geophysical Journal International* 152: 318–334.
Vidale JE and Earle PS (2000) Fine-scale heterogeneity in the Earth's inner core. *Nature* 404: 273–275.
Vinnik LP, Chevrot S, and Montagner J-P (1997) Evidence for a stagnant plume in the transition zone? *Geophysical Research Letters* 24: 1007–1010.
Vinnik LP, Kind R, Kosarev GL, and Makeyeva LI (1989) Azimuthal anisotropy in the lithosphere from observations of long-period S-waves. *Geophysical Journal International* 99: 549–559.
Vinnik LP and Montagner JP (1996) Shear wave splitting in the mantle PS phases. *Geophysical Research Letters* 23(18): 2449–2452.
Vinnik LP, Kurnik, and Farra V (2005) Lehmann discontinuity beneath North America: No role for seismic anisotropy. *Geophysical Research Letters* 32: L09306 (doi:10.1029/2004GL022333).
Vočadlo L, Alfe D, Gillan MJ, Wood IG, Brodholt JP, and Price GP (2003a) Possible thermal and chemical stabilization of body-centred-cubic iron in the Earth's core. *Nature* 424: 536–539.
Vočadlo L, Alfè D, Gillan MJ, and Price GD (2003b) The properties of iron under core conditions from first principles calculations. *Physics of the Earth and Planetary Intereriors* 140: 101–125.
Voigt W (1928) *Lerrbuch der Kristallphysik*. Leipzig: Teubner-Verlag.
Wang J, Sinogeikin SV, Inoue T, and Bass JD (2003) Elastic properties of hydrous ringwoodite. *American Mineralogist* 88: 1608–1611.
Watt JP (1988) Elastic properties of polycrystalline materials: Comparison of theory and experiment. *Physics and Chemistry of Minerals* 15: 579–587.
Webb SL (1989) The elasticity of the upper mantle orthosilicates olivine and garnet to 3 GPa. *Physics and Chemistry of Minerals* 516: 684–692.
Webb SL and Jackson I (1993) The pressure dependence of the elastic moduli of single-crystal orthopyroxene $(Mg_{0.8}Fe_{0.2})SiO_3$. *European Journal of Mineralogy* 5: 1111–1119.
Weber P and Machetel P (1992) Convection within the inner core and thermal implications. *Geophysical Research Letters* 19: 2107–2110.
Weidner DJ, Bass JD, Ringwood AE, and Sinclair W (1982) The single-crystal elastic moduli of stishovite. *Journal of Geophysical Research* 87: 4740–4746.
Weidner DJ and Carleton HR (1977) Elasticity of coesite. *Journal of Geophysical Research* 82: 1334–1346.
Weidner DJ and Ito E (1985) Elasticity of $MgSiO_3$ in the ilmenite phase. *Physics of the Earth and Planetary Interiors* 40: 65–70.
Weidner DJ, Sawamoto H, Sasaki S, and Kumazawa M (1984) Single-crystal elastic properties of the spinel phase of $Mg_2SiO_4$. *Journal of Geophysical Research* 89: 7852–7860.
Weidner DJ, Wang H, and Ito J (1978) Elasticity of orthoenstatite. *Physics of the Earth and Planetary Interiors* 17: P7–P13.
Weidner D, Li L, Davis M, and Chen J (2004) Effect of plasticity on elastic modulus measurements. *Geophysical Research Letters* 31: L06621 (doi:10.1029/2003GL019090).
Wenk H-R, Baumgardner J, Lebensohn R, and Tomé C (2000) A convection model to explain anisotropy of the inner core. *Journal of Geophysical Research* 105: 5663–5677.
Wenk HR, Lonardelli I, Pehl J, *et al.* (2004) *In situ* observation of texture development in olivine, ringwoodite, magnesiowüstite and silicate perovskite. *Earth and Planetary Science Letters* 226: 507–519.
Wenk H-R, Speziale S, McNamara AK, and Garnero EJ (2006) Modeling lower mantle anisotropy development in a

subducting slab. *Earth and Planetary Science Letters* 245: 302–314.
Wenk H-R, Takeshita T, and Jeanloz R (1988) Development of texture and elastic anisotropy during deformation of hcp metals. *Geophysical Research Letters* 15: 76–79.
Wentzcovitch RM, Karki BB, Cococcioni M, and de Gironcoli S (2004) Thermoelastic properties of of MgSiO3 perovskite: Insights on the nature of the Earth's lower mantle. *Physical Review Letters* 92: 018501.
Wentzcovitch RM, Tsuchiya T, and Tsuchiya J (2006) MgSiO3-post perovskite at D'' conditions. *Proceedings of the National Academy of Sciences USA* 103: 543–546 (doi:10.1073_pnas.0506879103).
Widmer R, Masters G, and Gilbert F (1992) Observably split multiplets—data analysis and interpretation in terms of large-scale aspherical structure. *Geophysiocal Journal International* 111: 559–576.
Williams Q and Garnero EJ (1996) Seismic evidence for partial melt at the base of the Earth's mantle. *Science* 273: 1528–1530.
Willis JR (1977) Bounds and self-consistent estimates for the overall properties of anisotropic composites. *Journal of the Mechanics and Physics of Solids* 25: 185–202.
Wolfe CJ and Solomon SC (1998) Shear-wave splitting and implications for mantle flow beneath the MELT region of the East Pacific Rise. *Science* 280: 1230–1232.
Woodhouse JH, Giardini D, and Li X-D (1986) Evidence for inner core anisotropy from splitting in free oscillation data. *Geophysical Research Letters* 13: 1549–1552.
Wookey J, Kendall J-M, and Barruol G (2002) Mid-mantle deformation inferred from seismic anisotropy. *Nature* 415: 777–780.
Wookey J, Kendall J-M, and Rumpker G (2005a) Lowermost mantle anisotropy beneath the north Pacific from differential S-ScS splitting. *Geophysical Journal International* 161: 829–838.
Wookey J, Stackhouse S, Kendall J-M, Brodholt J, and Price GD (2005b) Efficacy of the post-perovskite phase as an explanation for lowermost-mantle seismic properties. *Nature* 438: 1004–1007.
Yeganeh-Haeri A (1994) Synthesis and re-investigation of the elastic properties of single-crystal magnesium silicate perovskite. *Physics of the Earth and Planetary Interiors* 87: 111–121.
Yeganeh-Haeri A, Weidner DJ, and Ito E (1989) Elasticity of $MgSiO_3$ in the perovskite structure. *Science* 243: 787–789.
Yoshida SI, Sumita I, and Kumazawa M (1996) Growth model of the inner core coupled with the outer core dynamics and the resulting elastic anisotropy. *Journal of Geophysical Research* 101: 28085–28103.
Yukutake T (1998) Implausibility of thermal convection in the Earth's solid inner core. *Physics of the Earth and Planetary Interiors* 108: 1–13.
Zaug JM, Abramson EH, Brown JM, and Slutsky LJ (1993) Sound velocities in olivine at Earth mantle pressures. *Science* 260: 1487–1489.
Zha C-S, Duffy TS, Downs RT, Mao H-K, and Hemley RJ (1996) Sound velocity and elasticity of single-crystal fosterite to 16 GPa. *Journal of Geophysical Research* 101: 17535–17545.
Zha C-S, Duffy TS, Downs RT, Mao H-K, Hemley RJ, and Weidner DJ (1987) Single-crystal elasticity of $\beta$-$Mg_2SiO_4$ to the pressure of the 410 km seismic discontinuity in the Eath's mantle. *Physics of the Earth and Planetary Interiors* 147: E9–E15.
Zha C-S, Duffy TS, Downs RT, Mao H-K, and Hemley RJ (1998) Brillouin scattering and X-ray diffraction of San Carlos olivine: Direct pressure determination to 32 GPa. *Earth and Planetary Science Letters* 159: 25–33.
Zha CS, Mao HK, and Hemley RJ (2000) Elasticity of MgO and a primary pressure scale to 55 GPa. *Proceedings of the National Academy of Sciences USA* 97: 13494–13499.
Zhang S and Karato S-I (1995) Lattice preferred orientation of olivine aggregates in simple shear. *Nature* 375: 774–777.
Zhang J, Song X, Li Y, Richards PG, Sun X, and Waldhauser F (2005) Inner core differential motion confirmed by earthquake waveform doublets. *Science* 309: 1357–1360.
Zimmerman ME, Zhang S, Kohlstedt DL, and Karato S-I (1999) Melt distribution in mantle rocks deformed in shear. *Geophysical Research Letters* 26(10): 1505–1508.
Xu Z, Wang Q, Ji S, *et al.* (2006) Petrofabrics and seismic properties of garnet peridotite from the UHP Sulu terrane (China): Implications for olivine deformation mechanism in a cold and dry subducting continental slab. *Tectonophysics* 421: 111–127.